

EXPERIMENTS IN CRYOGENIC TWO PHASE FLOW

By

CHRISTOPHER JAMES VELAT

A THESIS PRESENTED TO THE GRADUATE SCHOOL
OF THE UNIVERSITY OF FLORIDA IN PARTIAL FULFILLMENT
OF THE REQUIREMENTS FOR THE DEGREE OF
MASTER OF SCIENCE

UNIVERSITY OF FLORIDA

2004

Copyright 2004

by

Christopher James Velat

ACKNOWLEDGMENTS

I would like to express my appreciation to all of the individuals who have assisted me in my educational development and in the completion of my thesis. My greatest gratitude is extended to my supervisory committee chair, Dr. James Klausner. Dr. Klausner's boundless patience, constant encouragement, friendly demeanor, and professional expertise have been critical to both my research and education. He shares an outstanding level of professionalism and respect for all students. He is an inspirational professor and regarded highly. Dr. Renwei Mei also deserves recognition for his patience and astonishing technical expertise. I would like to further thank Dr. David Hahn for kindly serving on my supervisory committee.

I would like to additionally recognize my fellow graduate associates Jelliffe Jackson, Yusen Qi, Jun Liao, and Yi Li for their friendship and technical assistance. Their diverse cultural background and character have provided an enlightening and positive environment.

Additional acknowledgment must be addressed to Mrs. Becky Hoover for her continual administrative support and guidance. Mrs. Hoover has been an invaluable resource and has continually offered support and encouragement.

I would like to further acknowledge the Florida Space Grant Consortium for its funding and the opportunity to tour the Kennedy Space Center. This research was also funded by NASA Glenn Research Center under contract NAG3-2750.

Finally I would like to recognize my parents and family for their continual support and encouragement. I would like to thank my mom and dad for instilling the values that have afforded me success in my continual endeavors.

TABLE OF CONTENTS

	<u>page</u>
ACKNOWLEDGMENTS	iii
LIST OF FIGURES	vii
NOMENCLATURE	xi
ABSTRACT.....	xiii
CHAPTER	
1 INTRODUCTION.....	1
1.1 Cryogenic Chilldown Overview	2
1.1.1 Horizontal Flow Regimes.....	3
1.1.2 Heat Transfer Mechanisms.....	5
1.2 Outline of Current Investigation.....	6
2 EXPERIMENTAL FACILITY	8
2.1 System Overview.....	8
2.2 Liquid Nitrogen Storage and Supply	10
2.3 Test Section Design.....	11
2.4 Instrumentation and Calibration	13
2.4.1 Static Pressure Transducers.....	13
2.4.2 Test Section Pressure Drop	15
2.4.3 Flow Meter Calibration and Velocity Correlation.....	16
2.4.4 Temperature Measurements	19
2.5 Heat Transfer Section Design.....	21
2.6 Vapor Volume Fraction	22
2.7 Vapor Quality Estimation	24
2.8 Data Acquisition System	26
2.9 Digital Imaging Facility.....	28
3 CRYOGENIC CHILLDOWN VISUALIZATIONS IN HORIZONTAL FLOW	29
3.1 Introduction and Literature Survey.....	29
3.2 Visualizations of Cryogenic Chilldown.....	31
3.2.1 Pre-Quenching Front Visualizations	34

3.2.2	Quenching Front Visualizations	37
3.2.3	Post Quenching Front Visualizations	42
3.3	Vapor Volume Fraction and Quality Measurement Results.....	48
3.4	Discussion of Results.....	52
3.5	Sources of Experimental Error	55
4	WALL TEMPERATURE PROFILES AND CHILLDOWN TIME IN CRYOGENIC HORIZONTAL FLOW	57
4.1	Introduction and Literature Survey.....	57
4.2	Wall Temperature Profile and History	58
4.3	Discussion.....	71
4.4	Sources of Error	74
5	CONCLUSIONS AND RECOMMENDATIONS	75
5.1	Accomplishments and Findings.....	75
5.2	Recommendations for Future Research.....	76
APPENDIX		
A	PROPERTIES OF NITROGEN	77
B	EXPERIMENTAL CRYOGENIC CHILLDOWN VISUALIZATIONS	78
LIST OF REFERENCES		109
BIOGRAPHICAL SKETCH		112

LIST OF FIGURES

<u>Figure</u>	<u>page</u>
1-1 Typical flow regimes observed in horizontal two-phase flow.	5
2-1 Schematic diagram of the cryogenic flow facility.....	9
2-2 Schematic overview of a typical vacuum jacketed cryogenic cylinder [10].	11
2-3 Wall thickness selection chart used to design the visual test section [11].	12
2-4 Schematic of the flange assembly.	13
2-5 Calibration plot of the inlet pressure transducer.	14
2-6 Calibration plot of the exit pressure transducer.	14
2-7 Calibration plot of the test section differential pressure transducer.....	15
2-8 Calibration plot of the venturi differential pressure transducer.	18
2-9 Calibration plot of the actual velocity versus the ideal velocity.	19
2-10 Schematic of the thermocouple arrangement on the steel transfer line.....	20
2-11 Thermocouple arrangements along the pipe wall of the heat transfer section.	21
2-12 Thermocouple arrangements along the insulation of the heat transfer section.	22
2-13 Diagram of the various flow regimes observed.	23
2-14 Diagram of the model used for the stratified flow volume fraction computation. ...	23
2-15 Diagram of the model used for the annular flow volume fraction computation.	24
3-1 Experimentally observed flow structure transitions during cryogenic chilldown for horizontal flow.....	33
3-2 Photographs of the unstable vapor flow that occurs at the beginning of chilldown. (a) $G = 25 \text{ kg/m}^2\text{-s}$, $\bar{T}_w = 8.3 \text{ }^\circ\text{C}$, (b) $G = 25 \text{ kg/m}^2\text{-s}$, $\bar{T}_w = -0.2 \text{ }^\circ\text{C}$	35

3-3	Photographs of the unstable vapor flow that occurs at the beginning of chilldown. (a) $G = 64 \text{ kg/m}^2\text{-s}$, $\bar{T}_w = -12.4^\circ \text{C}$, (b) $G = 62 \text{ kg/m}^2\text{-s}$, $\bar{T}_w = -14.8^\circ \text{C}$	36
3-4	Photographs of the unstable vapor flow that occurs at the beginning of chilldown. (a) $G = 104 \text{ kg/m}^2\text{-s}$, $\bar{T}_w = 7.5^\circ \text{C}$, (b) $G = 115 \text{ kg/m}^2\text{-s}$, $\bar{T}_w = -2.3^\circ \text{C}$	37
3-5	Sequential photographs of the film boiling front as it crosses through the visual test section. (a) $G = 24 \text{ kg/m}^2\text{-s}$, $\bar{T}_w = -10.0^\circ \text{C}$, (b) $G = 24 \text{ kg/m}^2\text{-s}$, $\bar{T}_w = -10.7^\circ \text{C}$, (c) $G = 26 \text{ kg/m}^2\text{-s}$, $\bar{T}_w = -11.7^\circ \text{C}$	38
3-6	Sequential photographs of the film boiling front as it crosses through the visual test section. (a) $G = 72 \text{ kg/m}^2\text{-s}$, $\bar{T}_w = -28.9^\circ \text{C}$, (b) $G = 72 \text{ kg/m}^2\text{-s}$, $\bar{T}_w = -30.2^\circ \text{C}$, (c) $G = 72 \text{ kg/m}^2\text{-s}$, $\bar{T}_w = -31.4^\circ \text{C}$	40
3-7	Sequential photographs of the film boiling front as it crosses through the visual test section. (a) $G = 154 \text{ kg/m}^2\text{-s}$, $\bar{T}_w = -26.7^\circ \text{C}$, (b) $G = 143 \text{ kg/m}^2\text{-s}$, $\bar{T}_w = -28.0^\circ \text{C}$	41
3-8	Photographs of the various flow structures observed during the chilldown process following the passing of the film boiling front. (a) $G = 23 \text{ kg/m}^2\text{-s}$, $\bar{T}_w = -18.7^\circ \text{C}$, (b) $G = 72 \text{ kg/m}^2\text{-s}$, $\bar{T}_w = -84.3^\circ \text{C}$, (c) $G = 40 \text{ kg/m}^2\text{-s}$, $\bar{T}_w = -170.6^\circ \text{C}$	43
3-9	Photographs of the flow structures during the chilldown process following the passing of the film boiling front. (a) $G = 84 \text{ kg/m}^2\text{-s}$, $\bar{T}_w = -59.8^\circ \text{C}$, (b) $G = 104 \text{ kg/m}^2\text{-s}$, $\bar{T}_w = -120.9^\circ \text{C}$, (c) $G = 112 \text{ kg/m}^2\text{-s}$, $\bar{T}_w = 161.6^\circ \text{C}$, (d) $G = 126 \text{ kg/m}^2\text{-s}$, $\bar{T}_w = -175.6^\circ \text{C}$, (e) $G = 150 \text{ kg/m}^2\text{-s}$, $\bar{T}_w = -177.2^\circ \text{C}$	44
3-10	Photographs of the various flow structures observed during the chilldown process following the passing of the film boiling front. (a) $G = 176 \text{ kg/m}^2\text{-s}$, $\bar{T}_w = 39.7^\circ \text{C}$, (b) $G = 234 \text{ kg/m}^2\text{-s}$, $\bar{T}_w = -51.8^\circ \text{C}$, (c) $G = 211 \text{ kg/m}^2\text{-s}$, $\bar{T}_w = -62.5^\circ \text{C}$, (d) $G = 338 \text{ kg/m}^2\text{-s}$, $\bar{T}_w = -178.4^\circ \text{C}$	47
3-11	Graph of the vapor volume fraction and quality for experiment # 10.....	51
3-12	Graph of the vapor volume fraction and quality for experiment # 2.....	51
3-13	Graph of the vapor volume fraction and quality for experiment # 1.....	52

3-14	Graph of the vapor volume fraction data for experiment # 11.....	54
4-1	Schematic representation of the thermocouple arrangement on the stainless steel transfer line.....	60
4-2	Temperature history during chilldown for experiment # 1.	61
4-3	Mass flux history for experiment # 1.	61
4-4	Temperature history during chilldown for experiment # 2.	62
4-5	Mass flux history for experiment # 2.	62
4-6	Temperature history during chilldown for experiment # 3.	63
4-7	Mass flux history for experiment # 3.	63
4-8	Temperature history during chilldown for experiment # 4.	64
4-9	Mass flux history for experiment # 4.	64
4-10	Temperature history during chilldown for experiment # 5.	65
4-11	Mass flux history for experiment # 5.	65
4-12	Temperature history during chilldown for experiment # 6.	66
4-13	Mass flux history for experiment # 6.	66
4-14	Temperature history during chilldown for experiment # 7.	67
4-15	Mass flux history for experiment # 7.	67
4-16	Temperature history during chilldown for experiment # 8.	68
4-17	Mass flux history for experiment # 8.	68
4-18	Temperature history during chilldown for experiment # 9.	69
4-19	Mass flux history for experiment # 9.	69
4-20	Temperature history during chilldown for experiment # 10.	70
4-21	Mass flux history for experiment # 10.	70
B-1	Chilldown images from experiment # 1.....	79
B-2	Chilldown images from experiment # 2.....	81
B-3	Chilldown images from experiment # 3.....	84

B-4	Chiltdown images from experiment # 4.....	87
B-5	Chiltdown images from experiment # 5.....	89
B-6	Chiltdown images from experiment # 6.....	92
B-7	Chiltdown images from experiment # 7.....	94
B-8	Chiltdown images from experiment # 8.....	97
B-9	Chiltdown images from experiment # 9.....	100
B-10	Chiltdown images from experiment # 10.....	104

NOMENCLATURE

A	cross sectional area (m^2)
\bar{C}_0	empirical constant
C_p	specific heat (kJ/kg/K)
C_v	critical wave velocity (m/s)
C_{IV}	inviscid wave velocity (m/s)
f	frequency (Hz)
g	gravitational acceleration ($9.81 m/s^2$)
G	mass flux ($kg/m^2\cdot s$)
h	liquid level height (m)
h_{lv}	latent heat of vaporization (J/kg)
k	thermal conductivity (W/mK)
K_{12}	Vortex flow meter constant
ma	measured amperage (milliamps)
P	pressure (kPa or psi)
Q	volumetric flow rate (cfm or L/min)
r	radius (m)
S	slip velocity, ratio of vapor and liquid velocities
t	time (s)

T	temperature ($^{\circ}\text{C}$ or K)
$\overline{T_w}$	average wall temperature ($^{\circ}\text{C}$)
u	axial velocity (m/sec)
U	average axial phase velocity (m/s)
V	voltage (volts)
$\overline{V_{vj}}$	empirical constant
χ	vapor quality

Greek

α	volume fraction
β	angle of inclination from the horizon (degree)
δ	liquid film thickness (m)
μ	dynamic viscosity (Ns/m^2)
ρ	density (kg/m^3)
σ	liquid/vapor surface tension (N/m)

Subscripts

2ϕ	two-phase
g	gas
l	liquid
v	vapor
i	ideal

Abstract of Thesis Presented to the Graduate School
of the University of Florida in Partial Fulfillment of the
Requirements for the Degree of Master of Science

EXPERIMENTS IN CRYOGENIC TWO PHASE FLOW

By

Christopher James Velat

August 2004

Chair: James F. Klausner

Major Department: Mechanical and Aerospace Engineering

A cryogenic chilldown facility has been designed, fabricated, and tested to experimentally study the flow structure and heat transfer processes that occur in horizontal two-phase flow during chilldown. The facility incorporates a Pyrex viewing section from which the flow structure and heat transfer transitions may be observed and recorded using a high resolution CCD camera system. Temperature and pressure measurements are recorded from sensors throughout the facility to monitor the flow conditions and the external transfer line wall temperature.

Visualizations of the flow structure have revealed the presence of several transitions during the chilldown phase. The general chilldown process begins with purely vapor flow. The vapor flow results from the rapid evaporation of the cryogenic liquid when it encounters the hot transfer line. The vapor surges through the system and was observed to choke at the throttling ball valve. As chilldown progresses droplets of liquid begin to accumulate on the bottom of transfer line. Film boiling is evident at this phase and the droplets travel at high speed on top of a thin vapor layer. A more observable

stream continues to develop until a quenching front is observed. The quenching front marks the transition from film boiling to nucleate boiling. The nucleate boiling phase typically assumes a stratified/wavy flow structure, which gradually transitions into slug and plug flow near the end of chilldown. At high flow rates the nucleate boiling phase is suppressed and occurs for a shorter duration. Following the nucleate boiling phase the dominant heat transfer mechanism observed is two-phase bulk turbulent convection, with evaporation at the liquid/vapor interface. Annular flow was observed in several experiments but is not specifically addressed in the current research.

Temperature profiles were produced from 6 thermocouples that were placed on the external wall surface of the transfer line and insulated with Melamine foam insulation. Chilldown times were computed from temperature profiles and an approximate Leidenfrost temperature of -98°C was observed. Large circumferential temperature gradients were observed during chilldown and moderate axial gradients were also observed during the passing of the quenching front. The mass flux of the experiments had a considerable impact on the chilldown time and magnitude of the temperature gradients.

The experimental facility and the current data will be used in continued research to develop a comprehensive and fundamentally based numerical chilldown model.

CHAPTER 1 INTRODUCTION

Cryogenic fluid transfer is a complex physical phenomenon concerning the transport of low temperature liquids through transfer lines that are initially a couple of hundred degrees Celsius higher in temperature. When the cryogenic fluid contacts the comparatively hot pipe wall, voracious evaporation ensues resulting in large unstable pressure fluctuations and rapid contraction of the transfer system components.

To develop a comprehensive model of the chilldown process an elaborate investigation into the flow structure, heat transfer, pressure fluctuations, and temperature variation is required. Early examinations of chilldown conducted by Burke et al. [1] resulted in a crude model for estimating the chilldown time in pressurized lines. The model was constructed from a lumped energy and mass balance analysis of a control volume and disregarded the detailed transient phenomena of current interest. Bronson et al. [2] further investigated chilldown and attributed the existence of large temperature gradients between the top and bottom of transfer lines attributed to flow stratification. Additionally Bronson recognized the importance of flow regimes and suggested there exists good correlation between the empirical oil and water flow regime maps of Baker [3] and the two-phase flow of hydrogen. Hedayatpour et al. [4], and Steward et al. [5] have proposed more detailed numerical based chilldown models. Hedayatpour developed an advanced two-phase flow model for chilldown in vertical transfer lines. Their predictions of the wall temperature history and chilldown time are in good agreement with their experiments.

These pioneering investigations on chilldown have led to the development of functional cryogenic transfer systems. Yet, the detailed momentum and heat transfer processes occurring during chilldown are still not well understood, which limits the development of more advanced hydrodynamic and thermal models. The focus of this research is to provide detailed data on the two-phase flow characteristics of liquid nitrogen flowing through a horizontal transfer line during chilldown. The data will be used in future research to evaluate existing flow regime and heat transfer coefficient models and, when necessary, to develop new models for cryogenic two-phase flows. Advanced understanding of the chilldown stage of cryogenic transfer will ultimately improve safety, reduce fuel loss and time associated with the filling of reusable space vehicles, and encourage the development of advanced cryogenic systems.

1.1 Cryogenic Chilldown Overview

Cryogenic chilldown refers to the process by which the temperature of the transfer line is lowered to the saturation temperature of the cryogen. This process is highly unstable and characterized by large pressure fluctuations accompanied by transitory boiling heat transfer. As noted by Hedayatpour the specific two-phase flow pattern observed during chilldown is dependent on the pipeline orientation, cryogenic fluid temperature, vapor quality, and the flow rate. In the current work, visualizations of the chilldown process have revealed the presence of a quenching front at the onset of chilldown, which is followed by a sustained stratified liquid growth with evaporation at the liquid vapor interface. Nucleate boiling has been observed in all of the experiments and is most prominent at low mass flux.

1.1.1 Horizontal Flow Regimes

Flow regime identification is critical to the development of a comprehensive model for chillover. The heat transfer and pressure drop of a system can vary significantly depending on the flow regime condition. Parameters that affect the observed flow regime include the pipe orientation, flow rate, and vapor quality. Flow regimes for vertical flow vary from those observed for horizontal flow. As noted by Carey [6] horizontal flow has a propensity for stratification, resulting from the tendency of the vapor to migrate to the upper portion of the tube. As described by Warren and Klausner [7] in low quality flows the existing vapor bubbles of bubbly flow tend to agglomerate at the top of the tube due to buoyant stratification in the horizontal flow orientation.

The relative velocity between the vapor and the liquid also influences the observed flow regimes. Barnea and Taitel [8] noted that transitions from stratified flow to either wavy or in more extreme cases slug flow result from the instability generally attributed to the viscous Kelvin-Helmholtz instability. The Kelvin-Helmholtz instability is caused primarily from the Bernoulli effect by which the pressure decreases over the wave crest due to the velocity acceleration [8]. The work by Barnea and Taitel on interfacial and structural stability of separated flows identified the importance of the wall shear stress in the stability analysis for transitions to wavy and slug flows using the viscous Kelvin-Helmholtz neutral stability criterion,

$$(U_g - U_l) < K \left[\left(\rho_l \alpha_g + \rho_g \alpha_l \right) \frac{\rho_l - \rho_g}{\rho_l \rho_g} g \cos \beta \frac{A}{\frac{dA_l}{dh_l}} \right]^{\frac{1}{2}}, \quad (1.1)$$

where h is the liquid level, β is the angle of inclination from the horizon, A is the cross sectional area, U is the axial average phase velocity, α is the ratio of the phase area to the total cross sectional area, and K is a factor described below. For the inviscid case $K = 1$ and for the viscous case $K = K_v$ where

$$K_v = \sqrt{1 - \frac{(C_v - C_{IV})^2}{\frac{\rho_l - \rho_g}{\rho} g \cos \beta \frac{A}{\frac{dA_l}{dh_l}}}}, \quad (1.2)$$

and

$$\rho_{2\phi} = \rho_l \alpha_l + \rho_g \alpha_g. \quad (1.3)$$

$C_v - C_{IV}$ is the difference between the critical wave velocity at the inception of instability and the wave velocity for the inviscid Kelvin-Helmholtz analysis. This term accounts for the effect of the wall shear stress, which noted by Barnea and Taitel, tends to amplify disturbances of the film thickness. The viscous and inviscid criteria differ in the computational difficulty and predictive capabilities, with the latter offering an analytical solution but tending to over predict stability. In addition to tube orientation and relative phase velocity, heat transfer also influences the prevailing flow regimes due to the transverse momentum flux created by evaporation.

The flow structure of a system is affected by the quality and occurrence of destabilizing heat transfer mechanisms. The introduction of a cryogenic fluid to a transfer line results in rapid evaporation. This evaporation cools the system until thermodynamic conditions prevail capable of supporting a liquid film. Destabilizing boiling heat transfer continues during this initial phase, producing film boiling. As the system cools further the quenching front transverses downstream, and the liquid level

continues to rise. If the mass flux is low enough, nucleate boiling will be persistent with high wall superheats. As the rate of heat transfer slows in the later stages of chilldown vapor plugs and bubbles are observed. The various flow regimes typically observed in horizontal two-phase flow are illustrated in Figure 1-1.

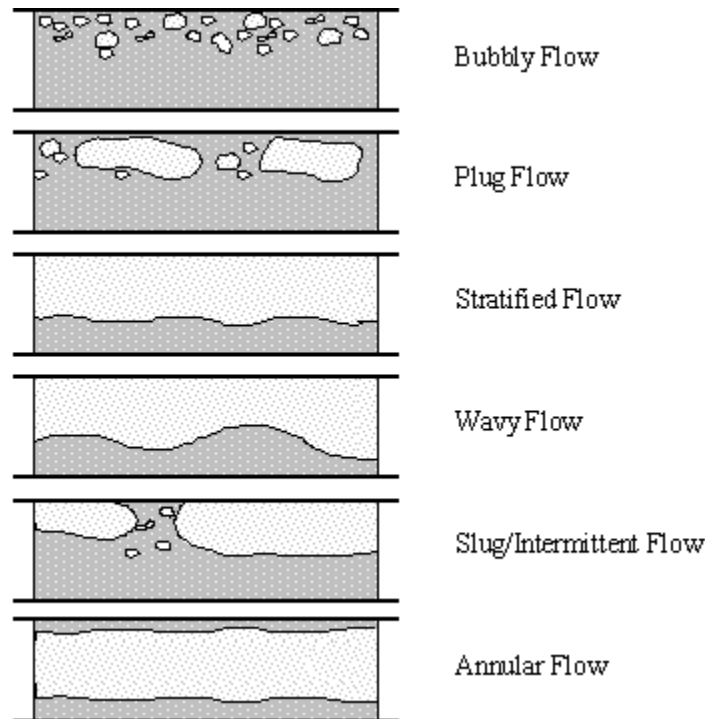


Figure 1-1. Typical flow regimes observed in horizontal two-phase flow.

1.1.2 Heat Transfer Mechanisms

An understanding of the prevailing heat transfer mechanisms is required to develop a comprehensive chilldown model. During chilldown three main heat transfer regimes were typically observed. In the beginning of chilldown the cryogenic fluid is introduced to the transfer line of the system, which is several hundred degrees Celsius higher in temperature. The cryogenic fluid undergoes rapid evaporation and the small liquid slugs present reside on a thin layer of vapor that is formed at the bottom of the transfer line. This stage, commonly referred to as film boiling, persists until the system chills down to the Leidenfrost temperature of the fluid. Heat is transferred during film

boiling from the pipe wall to the fluid primarily by conduction through the vapor film and by radiation from the hot pipe wall. Following the passing of the quenching front nucleate boiling was observed in all of the experiments; however, sustained nucleate boiling was generally only observed in experiments with low mass flux. When the mass flux exceeds a threshold, nucleate boiling is suppressed and evaporation occurs at the liquid/vapor interface of the liquid film; ebullition is not observed at the wall. Typically as the system neared chilldown, the test section became filled with liquid, resulting in single-phase convective heat transfer that persisted until the experiment was shutdown.

Knowledge of the prevailing heat transfer regimes is critical in selecting an appropriate model for the entire chilldown process. Past researchers Bronson et al. [2], Burke et al. [1], and Chi [9] generally assumed average heat transfer properties out of the need for simplification. Observations of the chilldown process as well as the experimental data clearly illustrate the importance of considering spatial variations and transients when developing an accurate and fundamentally based chilldown model.

1.2 Outline of Current Investigation

An experimental examination of the two-phase flow characteristics of liquid nitrogen flowing through a horizontal transfer line during chilldown has been performed to clarify the flow structure and heat transfer mechanisms as well as compile a database on two-phase flow transport. These data will be used in future research to develop advanced models capable of predicting the flow regime, pressure drop, and heat transfer coefficient of cryogenic two-phase flows. An experimental facility, which is described in great detail in chapter 2, has been fabricated that allows visualization of the flow structure and heat transfer mechanisms. The facility is capable of operating at pressures as high as 1400 kPa and mass flux ranges of 30-1000 kg/m²-sec. The cryogenic facility is

instrumented with thermocouples and pressure sensors for measuring the relevant heat transfer and flow properties. Visualizations of the flow regimes and heat transfer mechanisms are captured using a high resolution CCD camera system. All instrumentation in the facility has been fully calibrated and the tested measurement accuracy has been assessed.

In chapter 3 the visualizations from three experiments are presented. The images are arranged by increasing mass flux and separated by reference to the transitional boiling front passage. The visualizations prior to the transitional boiling front passage illustrate the stratified/wavy flow structure present during the initial phase of chilldown. Subsequent images of the growth and movement of the transitional boiling front from the three experiments are shown. The visualization section concludes with images that capture the nucleate boiling heat transfer and slug and plug flow structure transitions, which occurred after the quenching front passage. In addition to the visualizations, the vapor volume fraction data and computed quality for the three experiments are also presented and followed by a general discussion.

Chapter 4 presents the temperature data of the ten experiments. Demarcations indicating the approximate Leidenfrost temperature and visually observed transitional boiling front passage are included on the temperature profiles. The mass flux range as well as chilldown time data for each of the experiments is also reported.

Chapter 5 concludes the research with a summary of the overall work and discussion of the unresolved issues. Lastly, final recommendations are made for future research regarding annular flow; heat transfer coefficient, pressure drop measurements, and the development flow regime maps for cryogenic two-phase flows.

CHAPTER 2 EXPERIMENTAL FACILITY

2.1 System Overview

The experimental work presented herein was performed in a cryogenic facility that was designed specifically for this investigation. The experimental flow diagram is displayed schematically in Figure 2-1. A single pressurized liquid nitrogen cylinder feeds the facility. The cylinder, which is supplied by Praxair at 1587 kPa (230 psi), provides the driving potential for the liquid nitrogen fluid. Following discharge from the main cylinder the nitrogen is immediately directed through a shell and tube heat exchanger device. The heat exchanger coolant is supplied by another pressurized nitrogen cylinder, which is throttled and expanded to the atmosphere to achieve a combined Joule-Thomson and evaporative cooling effect. The additional cooling is used to keep the high-pressure nitrogen at subcooled conditions after being discharged from the storage cylinder. The working fluid is then directed through a 12.7 mm inner diameter 15.9 mm outer diameter 304-stainless steel tube that is instrumented with a series of external type E thermocouples, a single internal type E thermocouple, and a port leading to a static and differential Validyne pressure transducer. These instruments record the inlet flow conditions as well as outer wall temperature profile. After passing through the length of a stainless steel tube the fluid then proceeds through the visual test section, where high-resolution images of the flow structure are sequentially captured by the CCD camera system. The working fluid then passes through another length of instrumented

tubing containing a single internal type E thermocouple and port leading to another static and common differential Validyne pressure transducer. These instruments record the exit conditions of the working fluid. Positioned immediately after the aforementioned instruments is a heat transfer section containing internal inlet and exit thermocouple probes as well as a series of symmetrically spaced thermocouples secured both on the pipe wall and exterior of the insulation. The heat transfer section provides information required for analysis of the unsteady heat transfer coefficient. A cryogenic ball valve is located downstream of the instrumentation, and is used as a flow throttling device. After passing through the valve, the fluid is heated through a heating section to ensure only vapor is passed through the venturi flow meter. The nitrogen vapor is collected in a storage tank and vented to the atmosphere.

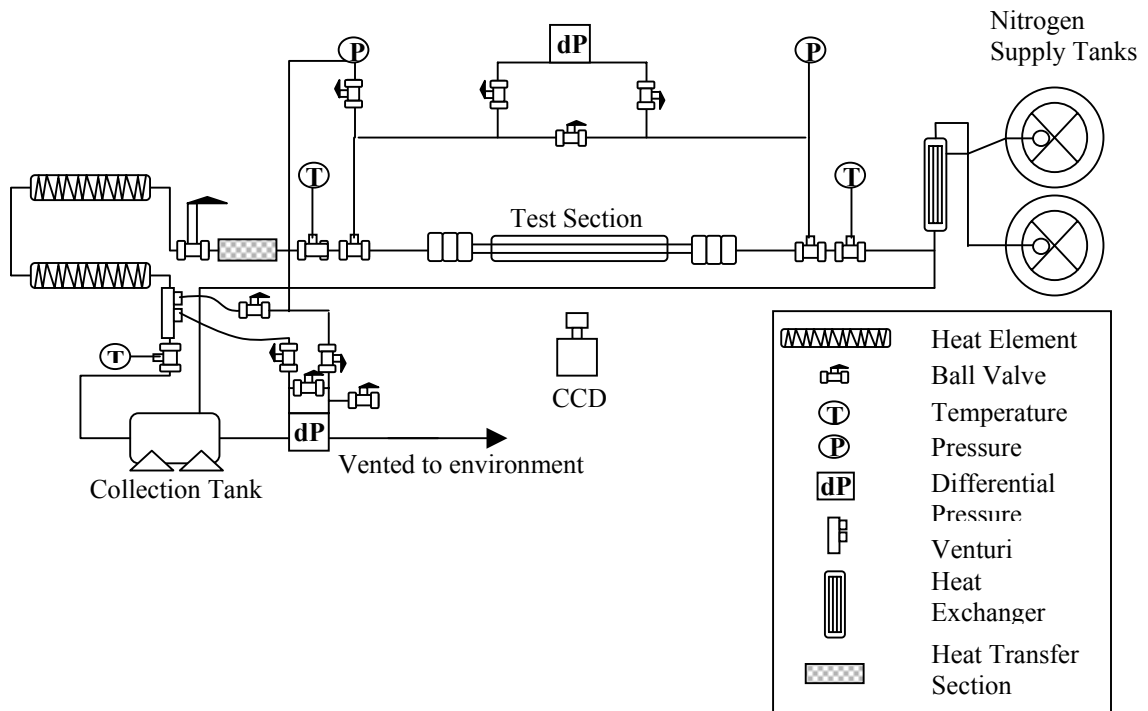


Figure 2-1. Schematic diagram of the cryogenic flow facility.

The facility is operated using a combination of manual control and computer monitoring. Manual control is required to open the nitrogen cylinders, set the proper positions of the ball valves, and activate the various computer programs prior to testing. Monitoring and recording of all temperature and pressure measurements as well as digital images was achieved via a high performance combination data acquisition image capture PC-style computer system. The Softwire programming platform is used to process the collected data. The program designed for this facility is capable of recording and displaying the data in near real time, allowing for immediate experiment feedback, and determination of the completed chilldown.

Nitrogen was selected as the cryogen working fluid because it is chemically inert, colorless, odorless, non-corrosive, nonflammable, relatively inexpensive, readily available, and poses no significant environmental hazards. Additionally, the properties of nitrogen are well documented, and may be referenced in Appendix A.

2.2 Liquid Nitrogen Storage and Supply

The test facility requires two vacuum-jacketed pressurized cylinders, schematically illustrated in Figure 2-2. The cylinders, which are provided and maintained by a local gas company, are available with a low pressure rating of 207 kPa (30 psi), or a high pressure rating 1587 kPa (230 psi). The high-pressure tanks are used to achieve high mass fluxes. To prepare these tanks for use, the pressure building circuit is actuated until the tank pressure gauge registers the appropriate level. Once the proper pressure level is reached, the associated liquid valve is opened and the chilldown experiment is commenced.

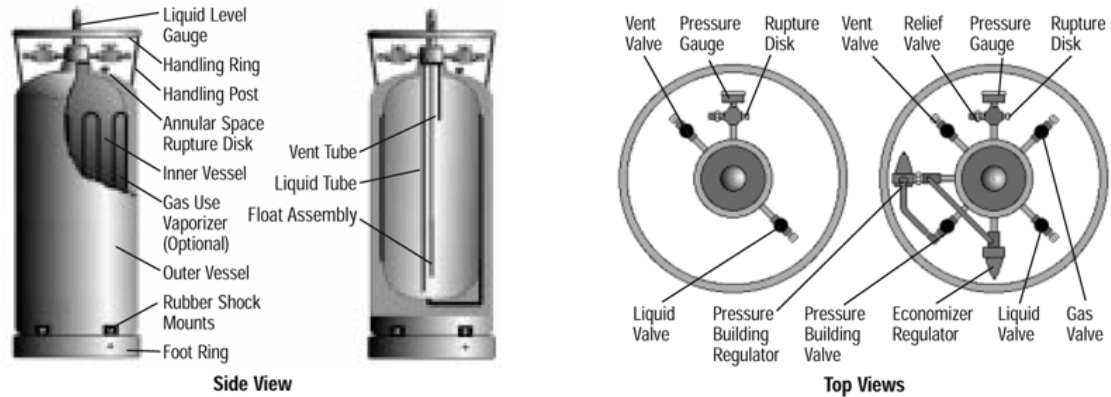


Figure 2-2. Schematic overview of a typical vacuum jacketed cryogenic cylinder [10].

2.3 Test Section Design

A crucial component to the cryogenic facility is the visual test section. The visual test section must be capable of withstanding the dynamic high pressure and low temperature conditions associated with chilldown, seamlessly attach with the steel tubing, and provide an excellent view of the working fluid. The success of the experimental facility is contingent upon meeting these demands while maintaining leak-free operation.

A Pyrex Glass tube was selected for the visual test section. Pyrex was chosen because of its toughness and superior thermal expansion (32.5×10^{-7} cm/cm/deg C) as compared to soda lime and other borosilicate glasses. To prevent condensation on the outer portion of the visual test section, a vacuum jacketed design was adapted. The wall thickness of the inner tube was selected to preclude catastrophic failure under the desired operating conditions. To select the appropriate wall thickness an industrial selection chart provided by the Bibby Sterilin Company was used and is included as Figure 2-3 [11].

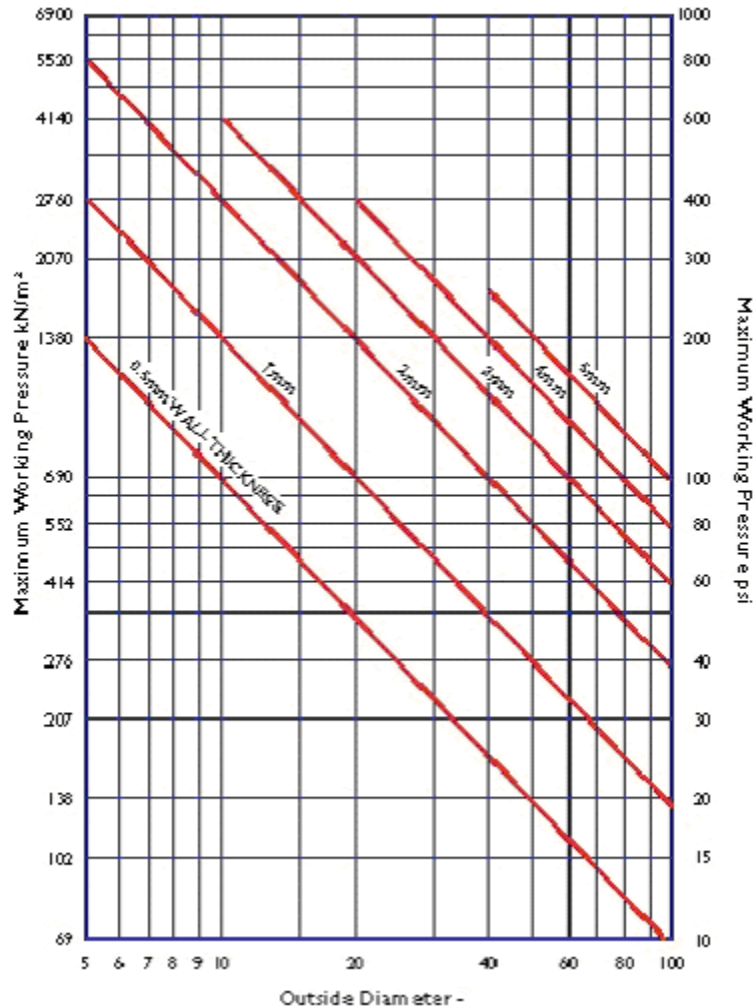


Figure 2-3. Wall thickness selection chart used to design the visual test section [11].

Based on a maximum design pressure of 1400 kPa, a 19 mm OD 12.4 mm ID glass tube was selected for use. The extra thickness of the glass tube was selected to prevent hazardous explosion of the glass section as well as to withstand the compressive forces of the steel flanges necessary for leak-free operation. A novel flange assembly was constructed to seamlessly secure and seal the glass test section in place. The flange assembly consisted of a series of three flanges fastened with machine bolts. A leak-free seal was achieved through the compression of a Teflon o-ring and Teflon pipe wrap as depicted schematically in Figure 2-4.

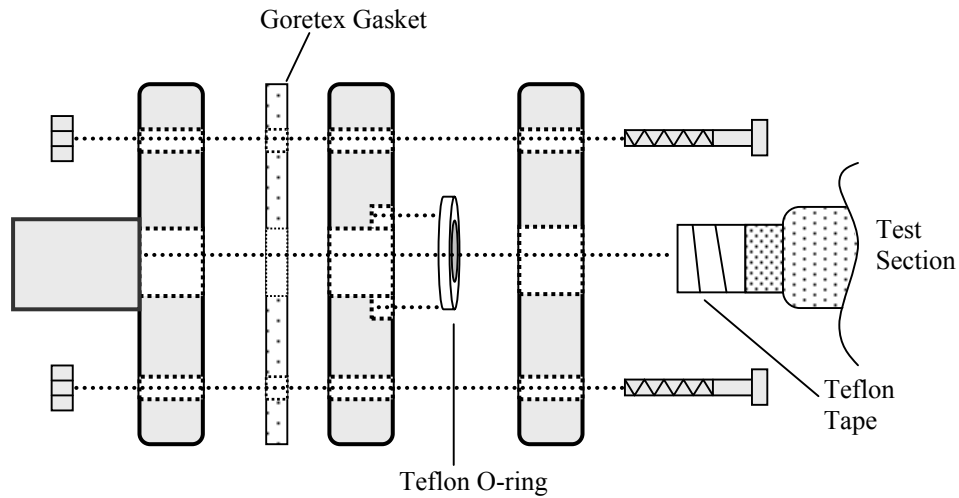


Figure 2-4. Schematic of the flange assembly.

2.4 Instrumentation and Calibration

2.4.1 Static Pressure Transducers

Two Validyne P2-200V pressure transducers were installed in line on either side of the visual test section. The first transducer was used to measure the inlet pressure of the flow while exit pressure transducer measured the pressure just prior to the venturi flow meter. Each transducer was rated to 1380 kPa and had been independently calibrated using a mercury monometer. The calibration plots are referenced in Figures 2-5 and 2-6. The linear curve fits for the inlet and exit pressure transducers are

$$P_{inlet} = -27.712 + 274.937 * V \quad (2.1)$$

and

$$P_{exit} = -30.709 + 276.479 * V \quad (2.2)$$

respectively, where P_{inlet} and P_{exit} are given as gage pressure in kPa and V is in volts. The calibrations are accurate to .25% of their respective full scale.

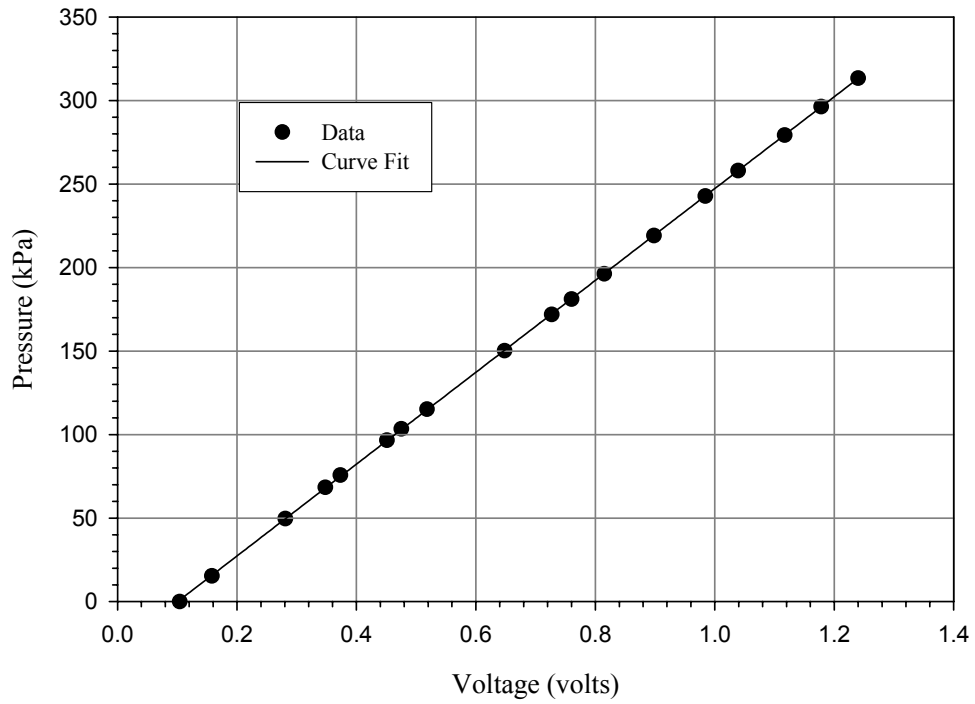


Figure 2-5. Calibration plot of the inlet pressure transducer.

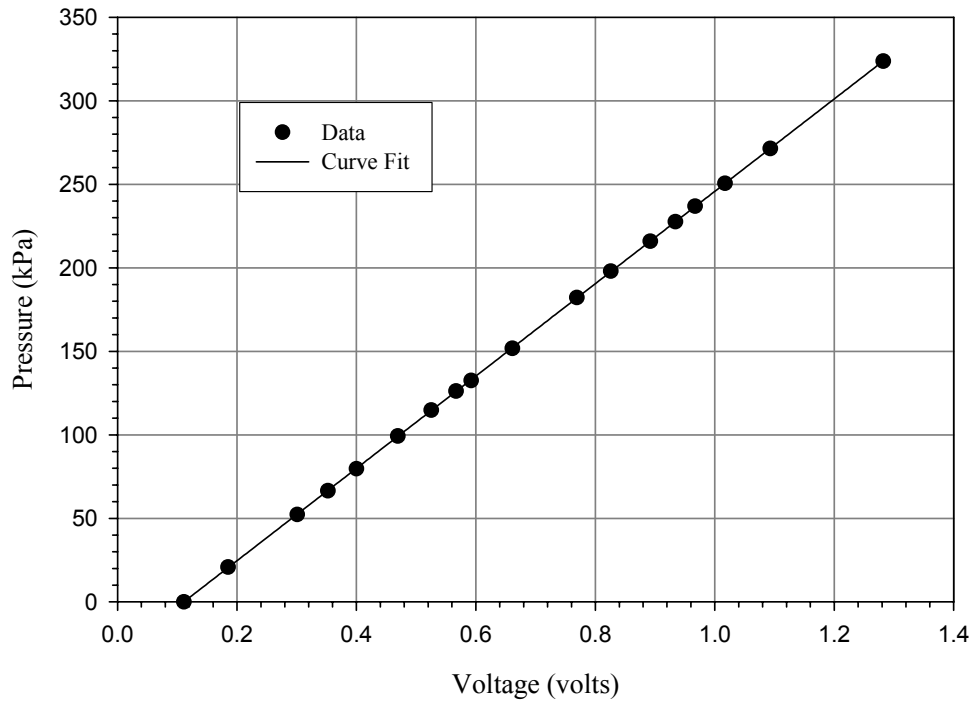


Figure 2-6. Calibration plot of the exit pressure transducer.

2.4.2 Test Section Pressure Drop

The pressure drop across the test section is measured using a Validyne model DP215 variable reluctance differential pressure transducer equipped with a dash-30 diaphragm. A carrier demodulator device is used to convert the transducer signal to an analog voltage. The carrier demodulator device is capable of conditioning the span and zero of the signal and was calibrated specifically with a designated transducer.

Calibration of the transducer was accomplished using a monometer containing R 827 monometer oil. The resulting calibration curve is graphically displayed in Figure 2-7, depicting a linear relationship between pressure and voltage. The resulting calibration curve fits

$$\Delta P = 1.2788 * V \quad (2.3)$$

where ΔP is given in kPa and V is in volts. The standard deviation of the calibration was 0.12%, which is within the 0.25% full-scale accuracy claimed by the manufacturer.

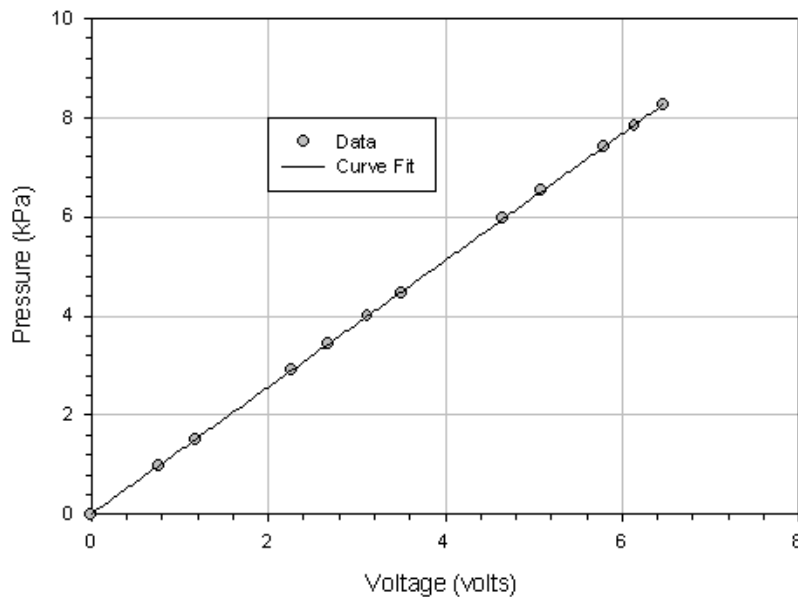


Figure 2-7. Calibration plot of the test section differential pressure transducer.

2.4.3 Flow Meter Calibration and Velocity Correlation

The flow rate of the nitrogen is measured using a Preso classical venturi flow meter with an inner diameter of 13.9 mm and a throat diameter of 8.73 mm. The flow meter is located downstream of the test section just past two large 1-kilowatt coil heaters. The coil heaters are used to ensure that only vapor enters the venturi during operation. The pressure ports on the venturi meter are coupled to another Validyne variable reluctance DP15 differential pressure transducer. A dash-40 diaphragm was selected for the transducer to maximize sensor output response while providing moderate overload protection. Similar to the pressure drop setup discussed in section 2.4.2, the differential pressure transducer is coupled to a carrier demodulator device. The transducer and demodulator device were calibrated together using a mercury monometer, Figure 2-8. The standard deviation of the differential pressure transducer calibration was 0.17%, which was within the 0.25% full-scale accuracy claimed by the manufacturer. After the pressure transducer was calibrated, the venturi device was calibrated with an Omega vortex flow meter using compressed air. The vortex flow meter provided frequency information that was conditioned into an analog voltage by measuring the voltage drop across a known resistor. The voltage measured was then related back to frequency through the relationship below

$$f = f_{\max} * \left(\frac{ma - 4}{20 - 4} \right) \quad (2.4)$$

where $f_{\max} = 914$ Hz is the maximum frequency and ma is the measured amperage in milliamps, which was related to the measured voltage through the equation

$$ma = \frac{V}{280} * 10^3 \quad (2.5)$$

where V is the measured voltage drop across the resistor. The analog voltage was then related to the volumetric flow rate with the equation below

$$f = K_{t2} * Q \quad (2.6)$$

where $K_{t2} = 32.443$ Hz/CFM is a constant derived from fluid properties and operating conditions and Q is the volumetric flow rate measured in CFM.

Once the volumetric flow rate was obtained from the vortex flow meter it was then used to calibrate the venturi by plotting the actual velocity measured with the vortex flow meter versus the ideal velocity, Figure 2-9. The ideal velocity was computed using a modified Bernoulli relation [12], which accounted for compressibility,

$$p_0 = p + \frac{1}{2} \rho V^2 \left(1 + \frac{1}{4} Ma^2 + \frac{2-\gamma}{24} Ma^4 + \dots \right). \quad (2.7)$$

The modified Bernoulli relation in equation 2.7 was solved iteratively. A polynomial curve, shown in equation 2.8, was then fit to the calibration data and used to correlate the ideal velocity with the actual velocity.

$$u_{actual} = (1 * 10^{-7})u_i^4 - (5 * 10^{-5}) * u_i^3 + 0.0076 * u_i^2 + 0.5653 * u_i \quad (2.8)$$

The ideal velocities shown in Figure 2-10 are computed based on the compressible and incompressible form of the Bernoulli equation. The differences between the compressible and incompressible ideal velocities do not visually appear to be significant in Figure 2-10. However, an analysis using cryogenic flow experimental data revealed a difference of about 5-10% at high velocities between the incompressible and compressible flow ideal. Therefore, for all tests Equation 2.7 is used to compile the ideal velocity and the actual velocity is determined using Equation 2.8.

Additionally noted in Figure 2-9 is the lack of low velocity measurements on the calibration plot. A trade off between resolution and operable pressure drop range was inherent to the diaphragm selection. To prevent possible damage to the instrument a diaphragm was selected that would safely accommodate the range of anticipated experimental differential pressures. Unfortunately the pressure range limitations on the diaphragm of differential pressure transducer prevented accurate measurement of the low velocity flows during the calibration. This unavoidable compromise is of minimal impact, as the vast majority of flow velocities that were in the high range.

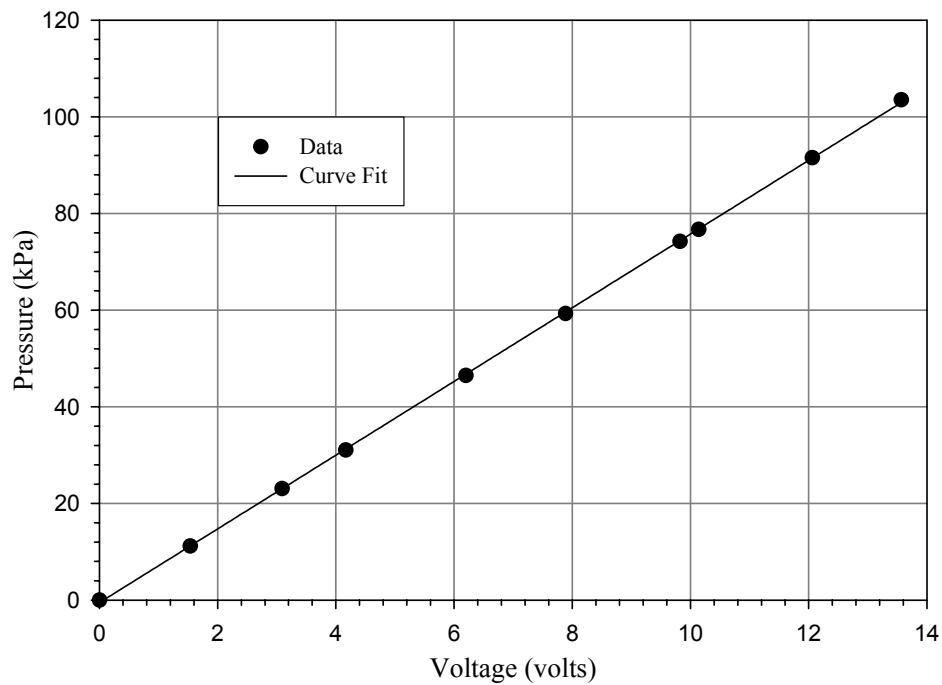


Figure 2-8. Calibration plot of the venturi differential pressure transducer.

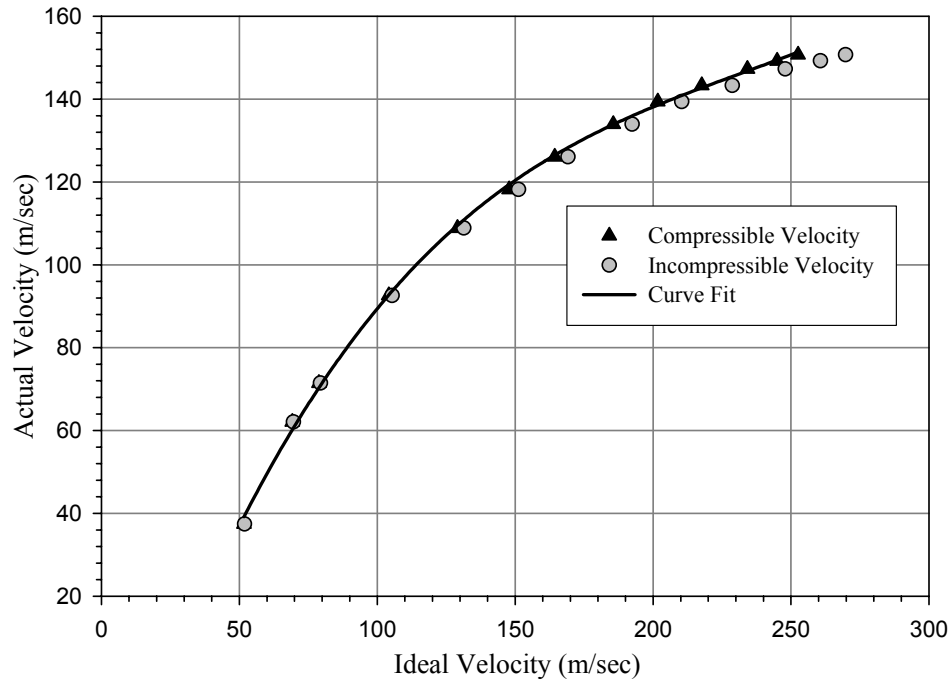


Figure 2-9. Calibration plot of the actual velocity versus the ideal velocity.

2.4.4 Temperature Measurements

Each cryogenic experiment required the acquisition of numerous temperature measurements. The temperature at the inlet and exit of the test section provided information that was used to monitor the chilldown process as well as compute the approximate liquid density. Additionally, a series of six thermocouples placed along the top and bottom of the 304-stainless steel tube prior to the test section (Figure 2-10) as well as 8 thermocouples placed circumferentially around the transfer line one meter down from the visual test section (Figure 2-11) supplied essential information on the progression of chilldown and flow regime transitions. The 304-stainless steel tube has an approximate thermal conductivity of $16.3 \text{ W/m}\cdot\text{C}$ and a specific heat of $0.46 \text{ kJ/kg}\cdot\text{C}$. To compile the thermodynamic information for the computation of the heat transfer coefficient the system was outfitted with an additional series of thermocouples that were

located after the test section (described in Section 2.5). A single thermocouple was also placed inline and just prior to the venturi to correct for the effects of temperature variation on the Mach number and vapor density.

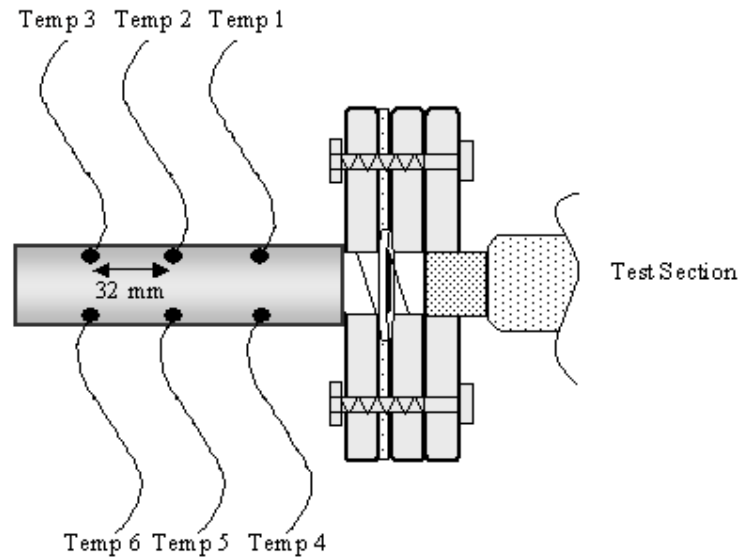


Figure 2-10. Schematic of the thermocouple arrangement on the steel transfer line.

All of the temperature measurements were made with type E (Chromel-Constantan) thermocouples that were either manufactured in the laboratory or purchased from Omega Engineering. The thermocouples that were manufactured in the laboratory were prepared from 36-gauge wire and welded in the laboratory with a bead size of approximately 0.5 mm. These thermocouples were used exclusively on the exterior of the pipe wall and insulation to measure the respective temperature distribution throughout chilldown process. 1/16-inch thermocouple probes were purchased from Omega Engineering to measure the initial fluid temperature. The probes were placed through precision-drilled holes in line with the fluid and sealed using a combination of brass compression fittings. The voltages of all of the thermocouples were recorded via the data acquisition system and converted to temperature using the supporting software.

2.5 Heat Transfer Section Design

The heat transfer segment of the facility was positioned downstream of the visual test section and contained 16 thermocouples that were symmetrically positioned around the exterior of the pipe wall and insulation as shown in Figures 2-11 and 2-12. The symmetrical groups of thermocouples were carefully positioned so that the exterior thermocouples that were secured to the insulation were exactly at the same angular positions as the interior thermocouples that were secured to the pipe wall. Each set of thermocouples were separated by an axial distance of approximately 9.0 cm and secured to either the insulation or pipe wall using 0.25-inch Teflon tape. Inlet and exit thermocouple probes, separated by an axial distance of 35.5 cm, were used to evaluate the change in fluid temperature. Currently this design provides sufficient temperature information for future analysis of the unsteady heat transfer coefficient.

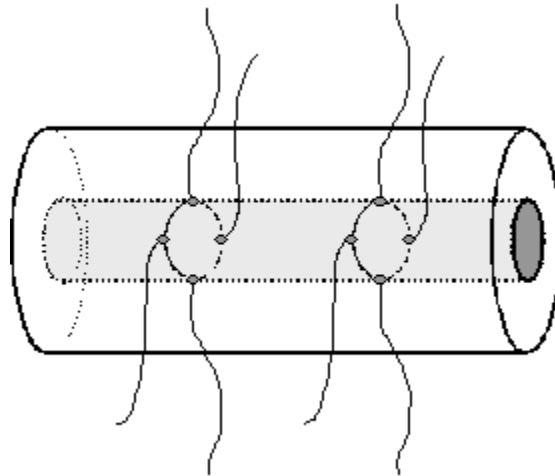


Figure 2-11. Thermocouple arrangements along the pipe wall of the heat transfer section.

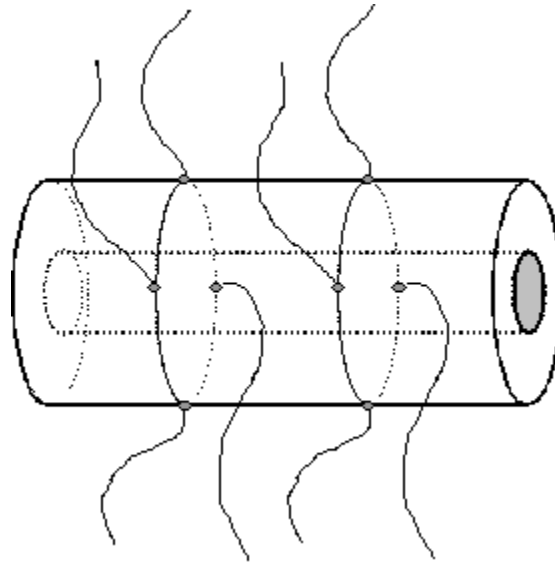


Figure 2-12. Thermocouple arrangements along the insulation of the heat transfer section.

2.6 Vapor Volume Fraction

The vapor volume fraction in the facility was computed from digital images of the flow structure obtained during the experiment. The high resolution digital imaging system discussed in section 2.5 was used to sequentially record images of the flow through out the test section. These images were stored and later analyzed using the Global Imaging Lab software to determine the flow structure and liquid height. The flow structure was analyzed initially to select the appropriate model to determine the vapor volume fraction. The flow structures observed during the experiments are illustrated in Figure 2-13. Previous researchers have used various conventions to describe the names of various flow structures observed in horizontal two-phase flows. The convention for naming the flow regimes used in this study follows that suggested by Carey [6] for horizontal two-phase flow structures.

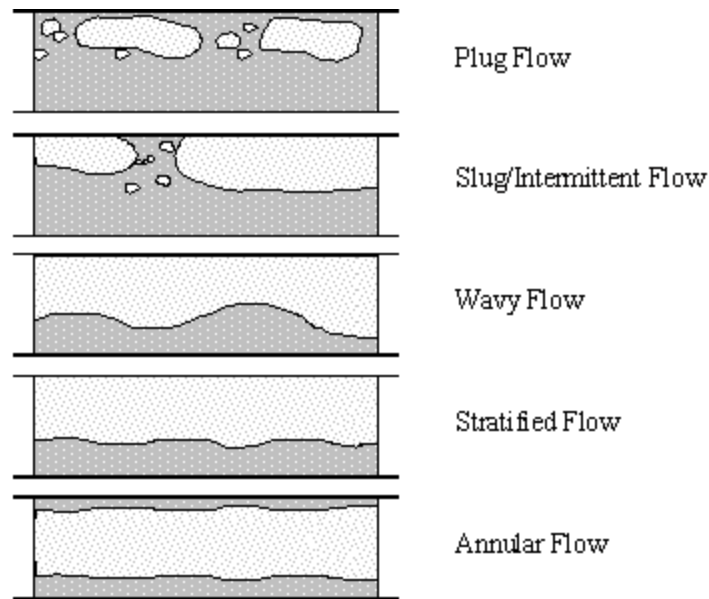


Figure 2-13. Diagram of the various flow regimes observed.

If stratified flow is prevalent then the liquid height is measured as depicted in Figure 2-14.

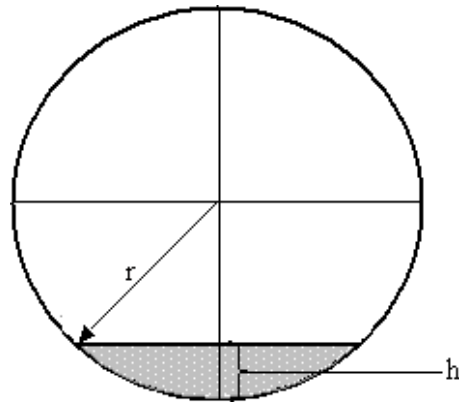


Figure 2-14. Diagram of the model used for the stratified flow volume fraction computation.

The vapor volume fraction is computed from the measured liquid height from,

$$\alpha_v = 1 - \left(\frac{r^2 \text{ACOS}\left(\frac{r-h}{r}\right) - (r-h)\sqrt{2rh-h^2}}{\pi r^2} \right) \quad (2.9)$$

The same relation is used to compute the vapor volume fraction for intermittent and wavy flow using the instantaneous liquid height. When annular flow is present, the flow structure is approximated as depicted in Figure 2-15. As shown in Figure 2-15 the vapor core is approximated as circular in shape.

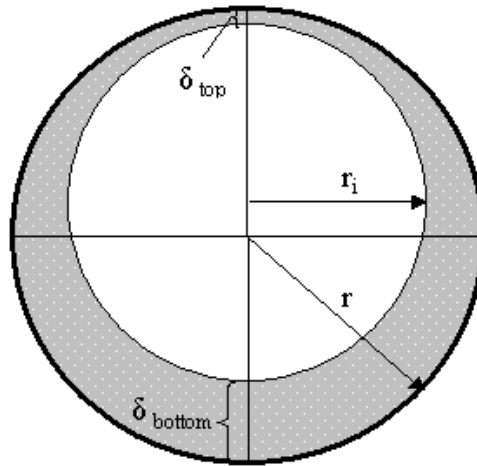


Figure 2-15. Diagram of the model used for the annular flow volume fraction computation.

The liquid film thickness at the top and bottom of the tube are measured, and the vapor volume fraction is computed from equation 2.10.

$$\alpha_v = \left(1 - \frac{\delta_{bottom}}{2r} - \frac{\delta_{top}}{2r} \right)^2 \quad (2.10)$$

2.7 Vapor Quality Estimation

Direct computation of the quality using an energy conservation analysis is not feasible because of the non-equilibrium conditions and unknown heat transfer rate from the pipe walls to the fluid. To obtain an approximation for the vapor quality a correlation between the vapor volume fraction and vapor quality is used. One method of relating the vapor volume fraction and vapor quality is through knowledge of the slip velocity and

density ratio. The slip velocity is defined as the ratio of vapor velocity to liquid velocity.

The vapor and liquid phase velocities may be expressed as

$$u_v = \frac{Gx}{\rho_v \alpha_v} \quad \text{and} \quad u_l = \frac{G(1-x)}{\rho_l (1-\alpha_v)}, \quad (2.11)$$

where G is the mass flux, u_v is the vapor velocity, u_l is the liquid velocity, α is the vapor volume fraction, and x is the quality.

Substituting these relations into the slip velocity definition yields the recognizable slip velocity expression,

$$S = \left(\frac{x}{1-x} \right) \left(\frac{1-\alpha_v}{\alpha_v} \right) \left(\frac{\rho_l}{\rho_v} \right). \quad (2.12)$$

Vapor volume fraction and vapor quality may be expressed in terms of the slip velocity as,

$$x = \frac{\alpha_v S}{\alpha_v S + (1-\alpha_v) \left(\frac{\rho_v}{\rho_l} \right)} \quad (2.14)$$

and

$$\alpha = \frac{x}{x + S(1-x) \left(\frac{\rho_v}{\rho_l} \right)}. \quad (2.15)$$

A limitation of the slip velocity model for estimating the vapor quality is that the slip velocity needs to remain relatively constant. The slip velocity does not typically remain constant over a wide range of quality and vapor volume fractions, especially during transient flow. Consequentially another method for estimating the vapor quality was explored.

Zuber and Findlay [13] developed a model commonly used to correlate the vapor volume fraction and quality. Zuber and Findlay fundamentally derived the model by considering the local volumetric fluxes of the vapor and liquid phases and the continuity equations of the two phases. The volume fraction may be expressed in terms of the vapor quality as,

$$\frac{1}{\alpha_v} = C_0 \left[1 + \frac{1-x}{x} \frac{\rho_v}{\rho_l} \right] + \frac{\rho_v}{Gx} \tilde{V}_{vj}, \quad (2.16)$$

where C_0 and \tilde{V}_{vj} are empirical constants. The first constant C_0 is the distribution parameter and accounts for non-uniform flow and concentration profiles, while the second constant \tilde{V}_{vj} accounts for the effect of the local relative velocity. Klausner [14] demonstrated in his horizontal flow experiments that the difference in the measured and calculated vapor volume fraction using the Zuber and Findlay model with empirical constants for C_0 and \tilde{V}_{vj} of 1.0 and 0.6 respectively was within +/- 5% for over 90 % of the data. Due to the excellent agreement with the horizontal flow experiments of Klausner using R113 as the boiling medium equation 2.16 is used to estimate the vapor quality from the measured vapor volume fraction.

2.8 Data Acquisition System

A digital data acquisition system consisting of a personal computer, data acquisition hardware, and supporting software was developed to record and condition the analog outputs of each instrument. The personal computer was built using an AMD Athlon XP 2200 MHz processor board combination supported with 15 Gigabits of random access memory. A PCIM-DAS1602/16 8-channel analog to digital board with 16-bit resolution was installed in the personal computer to acquire the data. The analog

to digital processor board was coupled to two CIO-EXP32 multiplexer boards. The multiplexer boards interfaced with the analog to digital board allowing the system to monitor up to 64 differential channels (32 channels per board). Each of the multiplexer boards was constructed of two banks of 16 channels, from which a given gain setting was selected by positioning a series of switches located on the board. As a result of this design the banks of channels on each board were separated based on the anticipated signal voltage and an appropriate gain setting was selected. The gain used for the thermocouples was 100 while the gain selected for the pressure measurements was 1. An on board junction temperature that was input to the analog to digital board through a prescribed channel served as a reference temperature for the thermocouple measurements. The channel selected for the junction temperature was carefully chosen to avoid a conflict with the analog to digital board. As per manufacturer's suggestion the pads on the back of each channel were soldered into the circuit. The soldering pads afforded each channel a 7Hz filtered input, open thermocouple detect, and a reference to ground through a 100k-ohm resistor. The analog to digital board and each of the multiplexer boards were calibrated to the manufacturer's specifications using the supplied Instacal software.

A computer program was developed to operate the data acquisition hardware, condition the analog signals, and continuously monitor the system in near real time. Using the Softwire software, a computer code was written that analyzed each of the occupied channels on the multiplexer boards. The program sequentially sampled each of the channels 50 times per second, storing each value in a distinct array. At the completion of the 50th sample, the values were time averaged and sent to an excel file for

further manipulation. The time averaging technique was employed to combat the inherently unstable conditions prevailing in two-phase flows as well as to remove additional unwanted noise. Prior to being transferred to excel the analog data were converted to temperatures and pressures in the Softwire program using the aforementioned calibration relations of Section 2.4 and the multiplexer board reference temperatures. The processed data were then simultaneously presented through a graphical user interface and sent to an excel file. The graphical user interface presented all of the temperature and pressure measurements for the facility and was updated every second. The excel file further processed the temperature and pressure data to obtain the mass flux, mach number, vapor and liquid velocity, vapor and liquid density, and vapor and liquid Reynolds number.

2.9 Digital Imaging Facility

An imaging facility was used to capture images of the flow regime, liquid height, and boiling phenomena through the visual test section. The imaging facility consisted of a Pulnix TM-1400CL progressive scan CCD camera, Data Translation DT-3145 frame grabber card, and supporting Global Imaging Lab software. The CCD camera was capable of image resolution of 1392 x 1040 pixels and was equipped with a Nikon 50 mm macro lens for high magnification. The camera was connected via a Camera Link cable to the DT-3145 frame grabber, which was installed in the abovementioned personal computer. Image acquisition and analysis was conducted using the Global Imaging Lab software. The Global Imaging Lab software was used to calibrate each image, from which accurate liquid height measurements and flow regimes were determined.

CHAPTER 3 CRYOGENIC CHILLDOWN VISUALIZATIONS IN HORIZONTAL FLOW

3.1 Introduction and Literature Survey

A detailed knowledge of the flow and heat transfer regimes is necessary to develop advanced numerical models capable of predicting the flow behavior of cryogenic fluids during chilldown. The identification and prediction of these regimes and their respective transitions is critical to the development of a fundamental numeric chilldown model. In general crude success has been achieved by previous researchers, which have typically neglected flow regime transition during chilldown in their numerical analysis.

Burke et al. [1], Graham et al. [15], Bronson et al. [2], and Chi and Vetere [16] conducted early notable chilldown experiments. The experimental chilldown studies performed by Burke produced a simple chill-down model. The model was based on one-dimensional heat transfer through a pipe wall and assumed an infinite heat transfer rate from the pipe wall to the cryogenic fluid. A crude model to calculate the chilldown time of a pressurized cryogenic transfer line was also proposed that neglected the affects of flow and heat transfer regime transitions. Subsequent research by Graham examined the heat transfer and pressure drop of film boiling liquid hydrogen through a heated pipe. They used the Martinelli parameter to correlate the frictional pressure drop and heat transfer coefficient; however their analysis did not give special consideration to flow regime transitions. In 1962 Bronson experimentally observed the presence of stratified flow in cryogenic chilldown systems and recognized the importance of the

circumferential temperature gradients in the facility design. Bronson further suggested there exists a good correlation between the early empirical oil-gas mixture flow regime maps of Baker [3] to that of boiling two-phase flow of hydrogen. Chi and Vetere experimentally studied the flow regime transition of hydrogen in a horizontal pipe. They recorded a temperature trace from thermocouples fixed to the center outside wall of a glass viewing section. The visual observations were correlated to measured temperature traces and used to identify flow regime transitions. Their visual observations were in general agreement with the sequence of flow regime transitions previously observed by Bronson. These early experiments provided a fundamental understanding of the chilldown process and have been useful in developing crude chilldown models.

Steward et al. [5] suggested an analytical chilldown model derived from the basic conservation equations. The conservation equations were simplified by assuming a homogeneous two-phase mixture, and one-dimensional flow. Steward considered film boiling, nucleate boiling, and convective heat transfer regimes in his model, and used the Kutateladze [17] correlation to identify the transition from nucleate to film boiling. He also addressed the presence of surge pressures resulting from the vapor produced from the rapid evaporation of the cryogenic fluid. Subsequent to Steward's work, Hedayatpour and Antar [4] proposed a chilldown model for a vertical line with liquid nitrogen. Hedayatpour and Antar employed a two-fluid model and analyzed four distinct flow regimes; complete liquid flow, inverted annular film boiling flow (where a liquid core is separated from the comparatively hot wall by a vapor film), dispersed flow, and complete vapor flow. Their model was derived from the one-dimensional form of the single-phase conservation equations, and a volume-averaged approach was used to address the two-

phase regimes. The results of the model compared well with the work of Kawaji and Banerjee [18,19], with the major deficiency being the requirement of flow regime knowledge and quenching front speed. Additional attempts to model the chilldown of a transfer line have been made by Cross et al. [20]. They have attempted a similar approach to that of Steward that incorporates a homogeneous two-phase mixture model. The model uses a Dittus-Boelter type correction for film boiling flow and is deficient due to oversimplifications regarding the heat transfer from the wall to the liquid.

Despite the aforementioned achievements, a more rigorous investigation of flow regime transition is necessary to accurately forecast the chilldown process. It is the intent of this portion of work to provide a comprehensive experimental database of visual images and flow information for the future development of fundamental predictive flow regime transition, pressure drop, and heat transfer relations. These relations will provide the necessary basis to complete a comprehensive fundamental chilldown model.

3.2 Visualizations of Cryogenic Chilldown

Visualizations of the chilldown process were conducted using the camera system described in Section 2.9. The images were recorded at one-second intervals and subsequently analyzed to determine an approximate chilldown sequence and vapor volume fraction. A typical chilldown experiment begins with purely vapor flow. The vapor genesis occurs in the supply tank and facility piping prior to the visual test section. As the liquid nitrogen contacts the hot pipe wall rapid evaporation ensues which produces this vapor. The vapor surges through the system at high velocity and is believed to choke at the throttling ball valve or flow meter. As the vapor continues to flow through the facility liquid is carried with it. The liquid is observed as a stream of droplets that are separated from the bottom of the visual tube by a thin layer of vapor. The layer of vapor

at the bottom of the tube is a result of the film boiling heat transfer that occurs in the initial stage of chilldown. The droplets move at a high velocity and evaporate quickly as they jet downstream. Eventually the droplets begin to coalesce and the stream of droplets is more visible. As chilldown continues the stream of droplets is replaced by a moving quenching front. The quenching front demarks the transition from film boiling to nucleate boiling. The quenching front typically moves in the direction of the flow but has been commonly observed to originate at multiple points downstream and flow backwards. After the quenching front transverses the test section an unstable pulsating stratified-wavy layer is observed. The liquid height fluctuates with the pulses in the system and continues to increase as the system cools further. Small vapor bubbles resulting from nucleate boiling are generally visible in this layer when the flow rate is not too high. A transition to slug flow is occasionally observed following moderate growth of the stratified-wavy layer. As the system nears chilldown the tube generally fills with liquid and transitions to plug flow, which typically persists until shutdown is initiated. A schematic drawing of the chilldown process is presented in Figure 3-1 and is followed by experimental images illustrating the various phases formerly discussed. The images presented in this document are of inferior resolution compared to the computer monitor versions and have been enhanced with lines denoting the liquid vapor interface as necessary. It should be noted that at high mass fluxes (generally larger than $600 \text{ kg/m}^2\text{-sec}$) annular flow was encountered. When annular flow was encountered, a similar chilldown process was observed except the annular flow structure persisted throughout chilldown. Due to the difficulty in determining the liquid height and consequentially the vapor volume fraction, the majority of experiments were conducted in a manner to avoid

encountering annular flow. Additional changes will be made in the future to the facility and camera system to analyze this regime and are discussed in greater detail in Section 5.3.

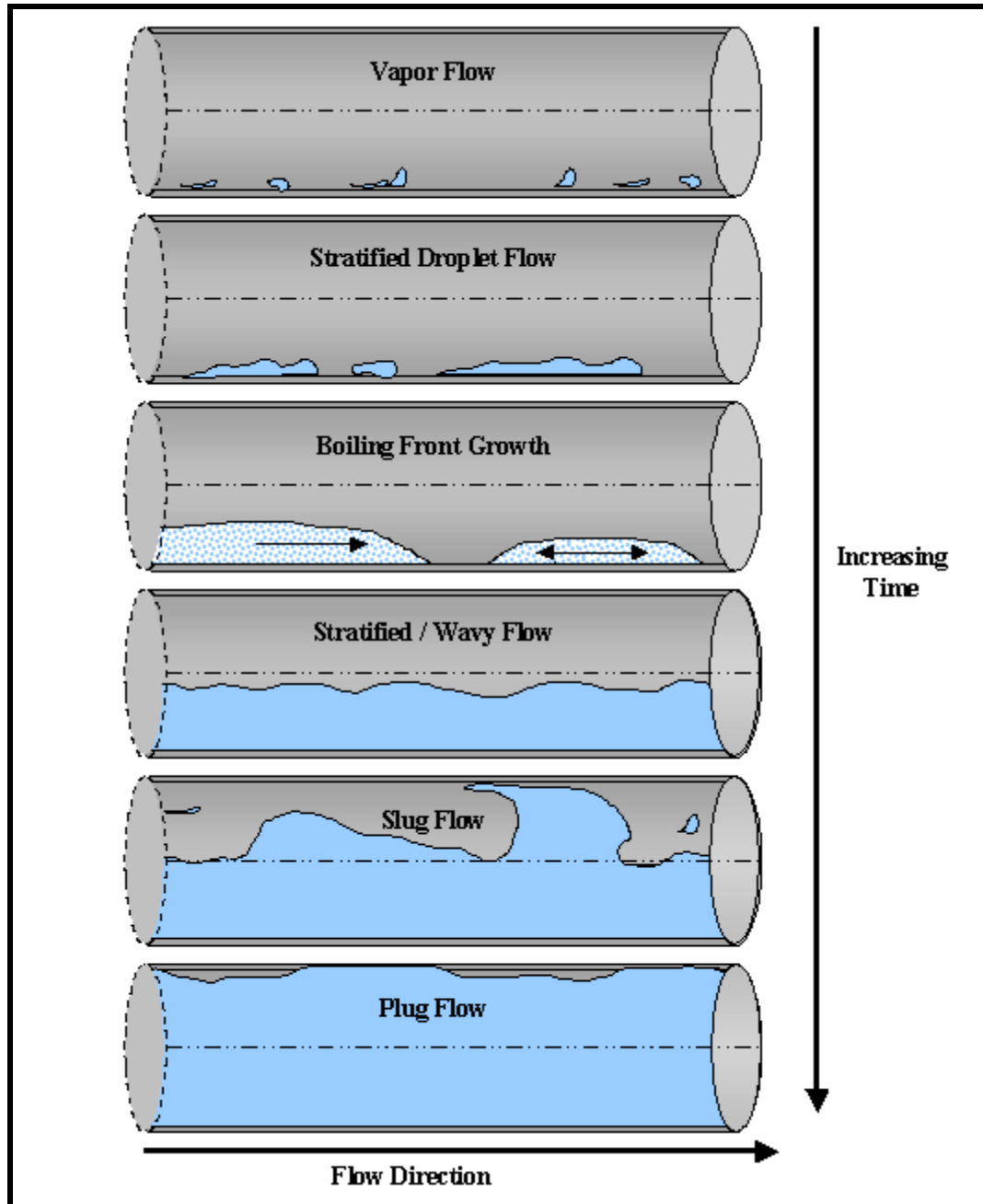


Figure3-1. Experimentally observed flow structure transitions during cryogenic chilldown for horizontal flow.

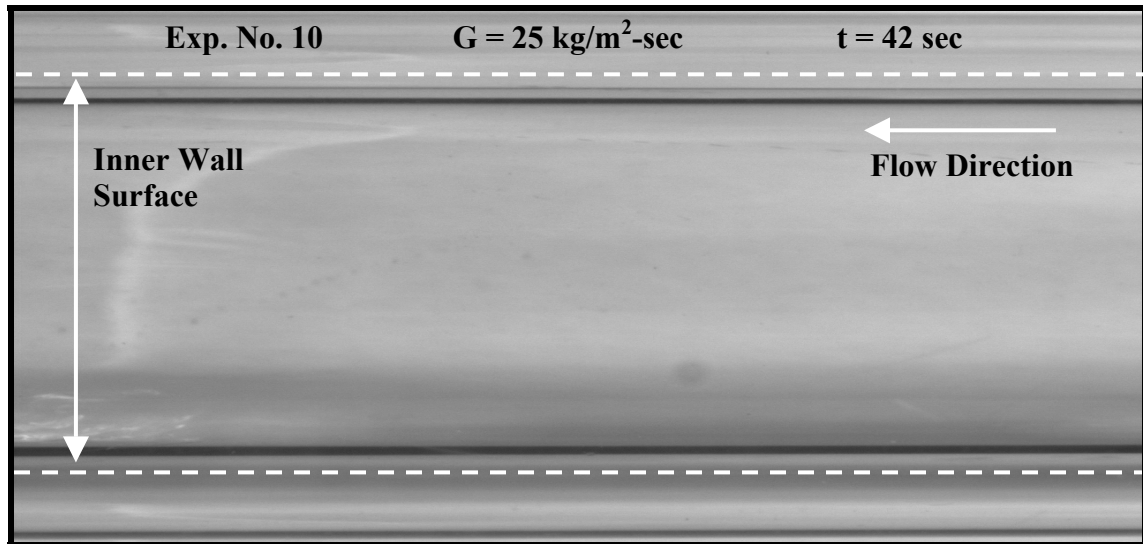
3.2.1 Pre-Quenching Front Visualizations

The series of pictures shown in Figures 3-2 through 3-10 of this chapter were selected from three experiments and have been arranged sequentially by increasing the computed mass flux to illustrate the general chilldown process as well as examine the influence of mass flux on the flow structure during chilldown. The images were recorded during each experiment at one-second intervals and were discriminately selected based on image quality and representation of typically observed phenomena. The instantaneous mass flux for each image as well as the average external wall temperature is included in the figure caption for each series of images.

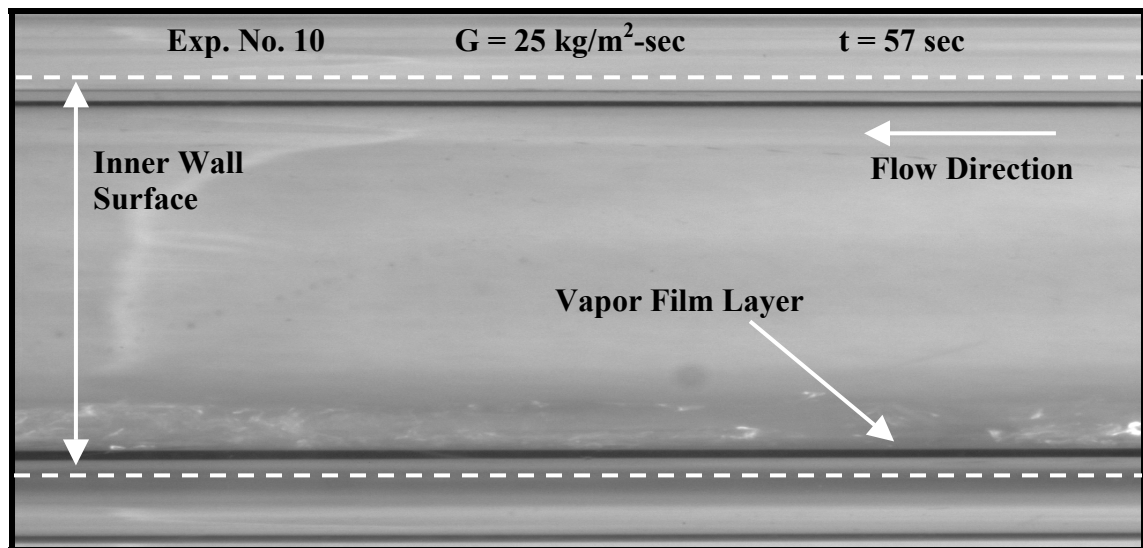
The chilldown process, as previously outlined in this chapter, consists of several distinct phases. To help distinguish the individual transitions that occur during chilldown, a boundary has been drawn around the passing of the quenching front. The following photographs reveal the events occurring prior to the quenching front and are the topic of the subsequent discussion.

Prior to the passing of the quenching front a high velocity vapor flow was observed. The vapor was generated from the film boiling of the cryogenic liquid. The vapor flow contained droplets of liquid located at the bottom of the test section. The liquid droplets rapidly traveled through the visual test section on top of a vapor film in both continuous and pulsating waves. Close examination of the images in Figures 3-2 through 3-4 exemplify this phenomenon and exhibit the development of the liquid layer on top of a very thin unsteady vapor film at the bottom of the test section. Arrows that identify the vapor layer have been added to Figures 3-2 b, 3-3 b, and 3-4 b. The developing liquid layer persisted during chilldown until the passing of the quenching

front. Comparison of the figures demonstrates an increasing thickness of the liquid layer at the bottom of the test section with increasing mass flux.

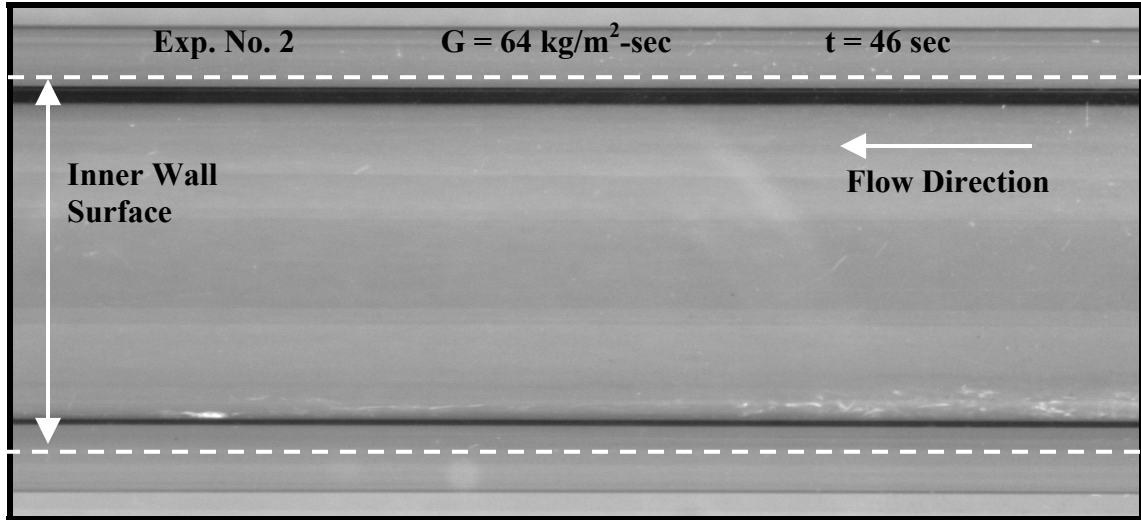


(a)

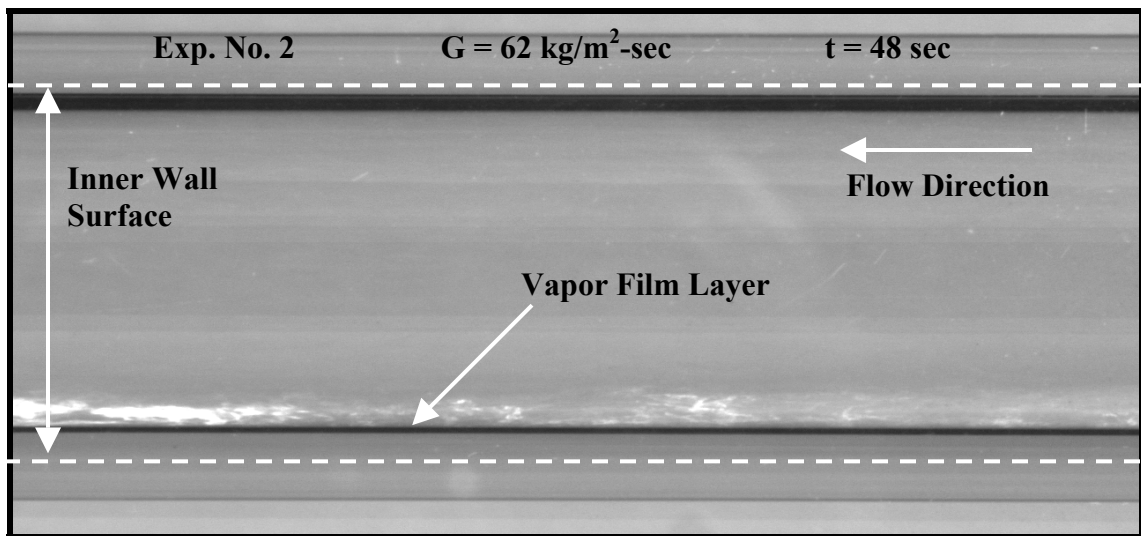


(b)

Figure 3-2. Photographs of the unstable vapor flow that occurs at the beginning of chillover. (a) $G = 25 \text{ kg/m}^2\text{-s}$, $\bar{T}_w = 8.3 \text{ }^\circ\text{C}$, (b) $G = 25 \text{ kg/m}^2\text{-s}$, $\bar{T}_w = -0.2 \text{ }^\circ\text{C}$.

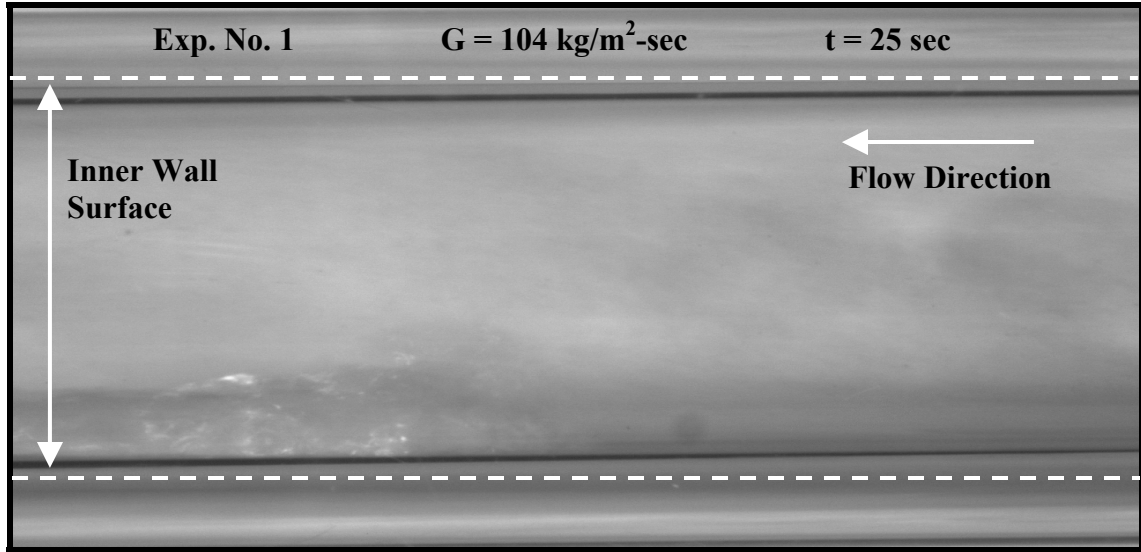


(a)

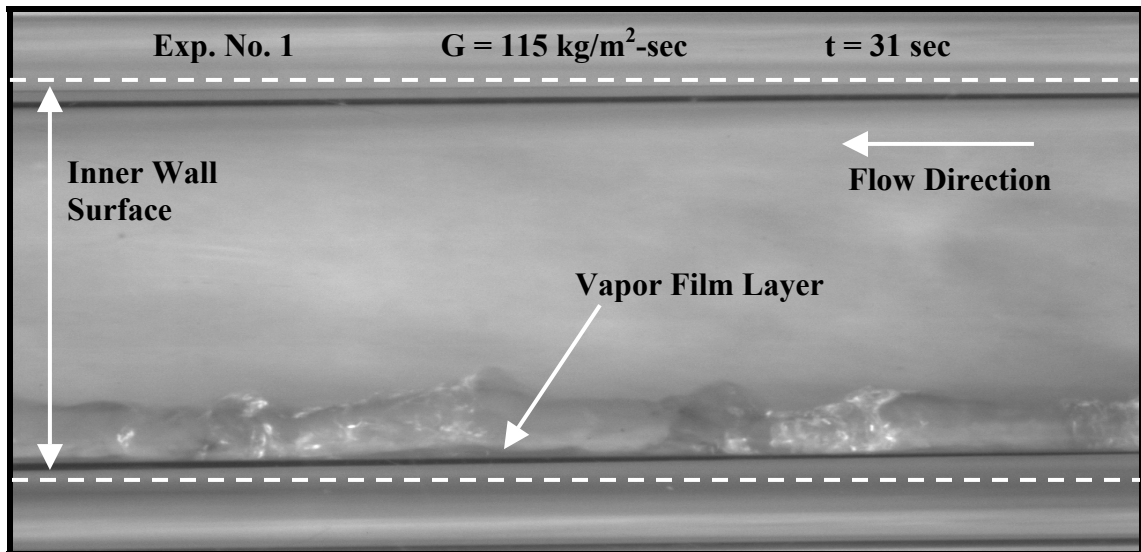


(b)

Figure 3-3. Photographs of the unstable vapor flow that occurs at the beginning of chillover. (a) $G = 64 \text{ kg/m}^2\text{-s}$, $\bar{T}_w = -12.4^\circ \text{C}$, (b) $G = 62 \text{ kg/m}^2\text{-s}$, $\bar{T}_w = -14.8^\circ \text{C}$.



(a)



(b)

Figure 3-4. Photographs of the unstable vapor flow that occurs at the beginning of chillover. (a) $G = 104 \text{ kg/m}^2\text{-s}$, $\bar{T}_w = 7.5 \text{ }^\circ\text{C}$, (b) $G = 115 \text{ kg/m}^2\text{-s}$, $\bar{T}_w = -2.3 \text{ }^\circ\text{C}$.

3.2.2 Quenching Front Visualizations

The images in Figures 3-5 through 3-7 display the progression of the quenching front across the visual test section. The images have been enhanced with a dotted line designating the contour of the quenching front. The quenching front was observed in all

of the experiments and varied in transverse speed, height, and incidence time according to experimental conditions. Experiments that were run at lower mass flux rates typically had lower transverse speeds, smaller quenching front heights, and occurred later in time than for experiments run at higher mass flux rates. This phenomenon is easily confirmed through visual comparison of the images of Figure 3-5 to that of the images of Figure 3-6 and 3.7. The image of Figure 3-7(a) from experiment No. 1 suggests a reversal of the direction of the quenching front. This phenomenon was commonly observed in several experiments and it is speculated that it is a result of liquid overshoot and system pressure fluctuations. The general shape of the quenching front is evident in the images; however it should be noted that a degree of distortion is present due to the refraction of the glass and the double walled construction of the vacuum-sealed visual test section.

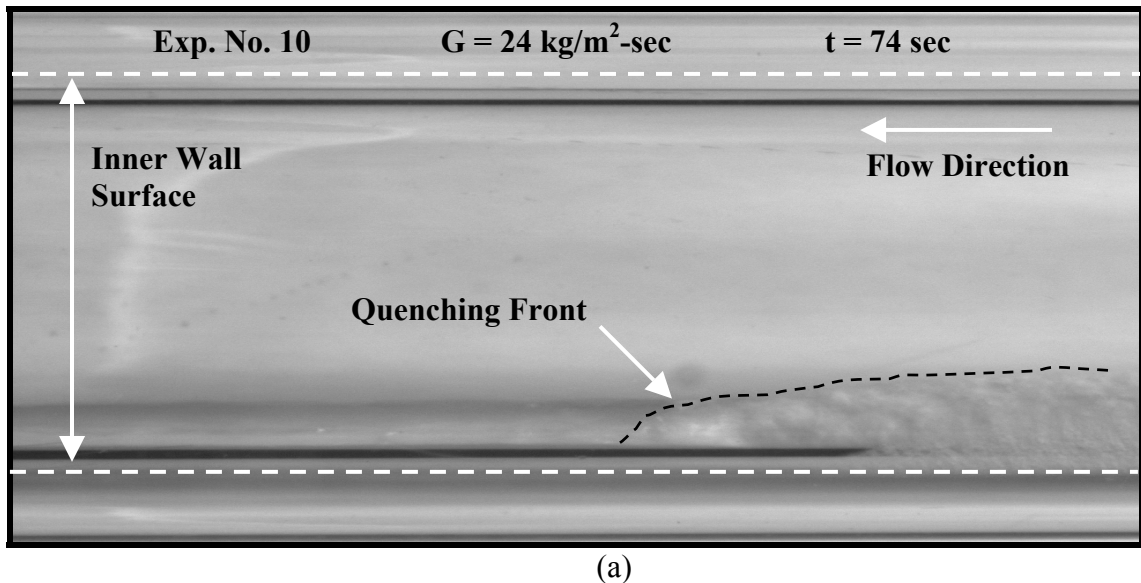
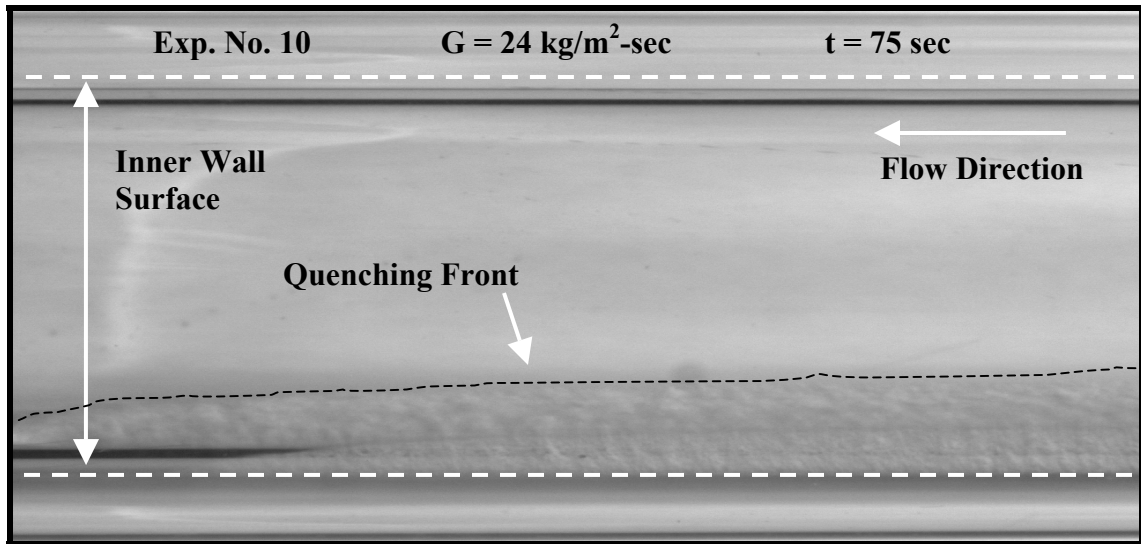
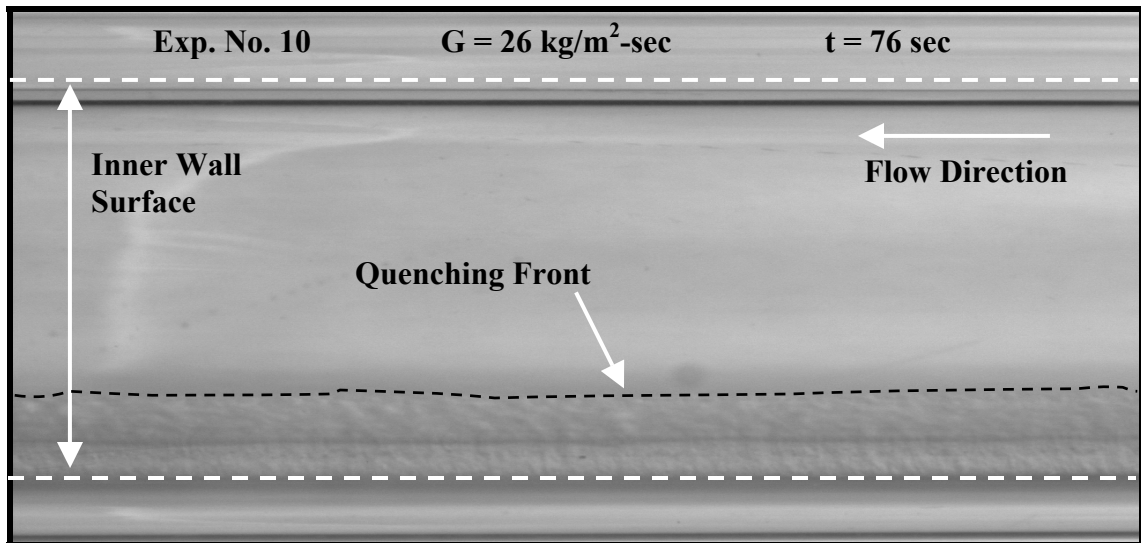


Figure 3-5. Sequential photographs of the film boiling front as it crosses through the visual test section. (a) $G = 24 \text{ kg/m}^2\text{-s}$, $\bar{T}_w = -10.0^\circ \text{C}$, (b) $G = 24 \text{ kg/m}^2\text{-s}$, $\bar{T}_w = -10.7^\circ \text{C}$, (c) $G = 26 \text{ kg/m}^2\text{-s}$, $\bar{T}_w = -11.7^\circ \text{C}$.

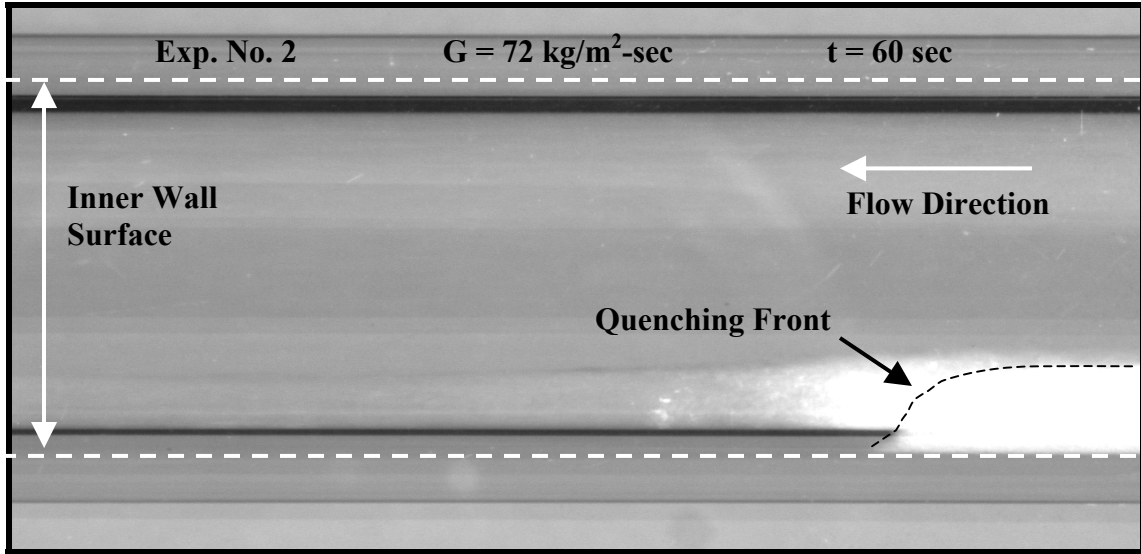


(b)

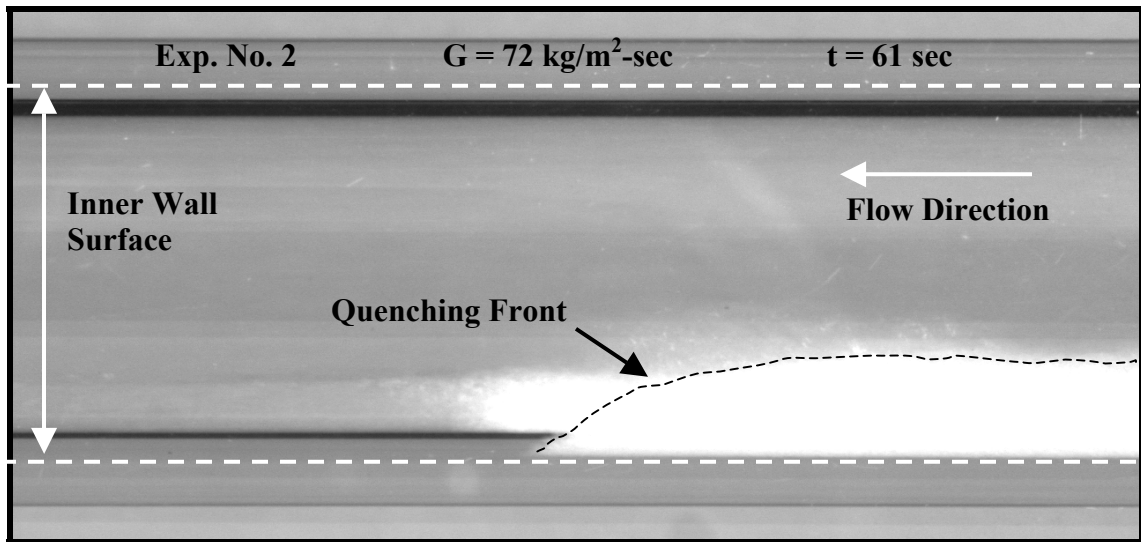


(c)

Figure 3-5. Continued.

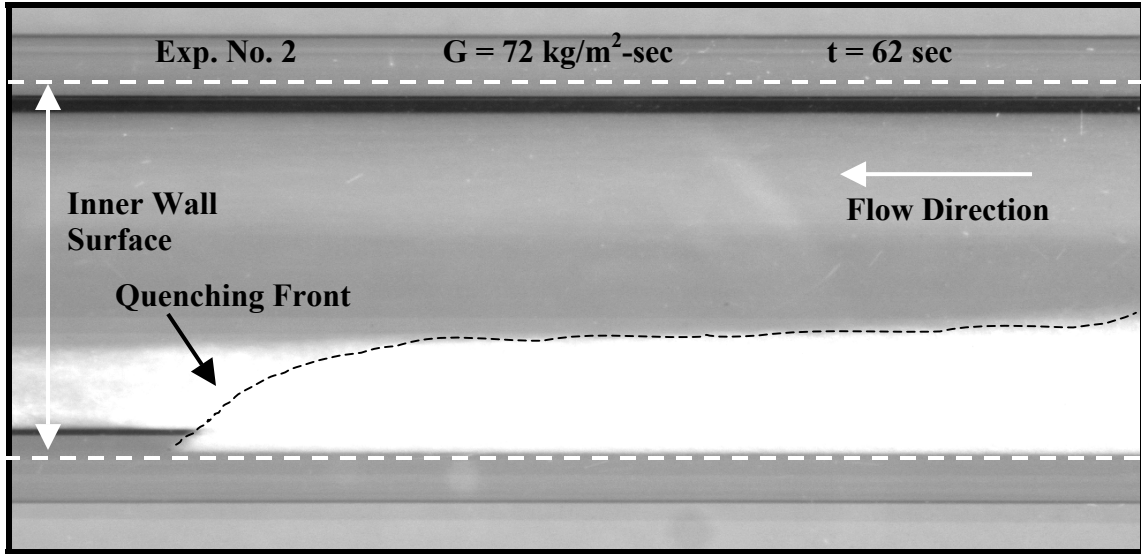


(a)

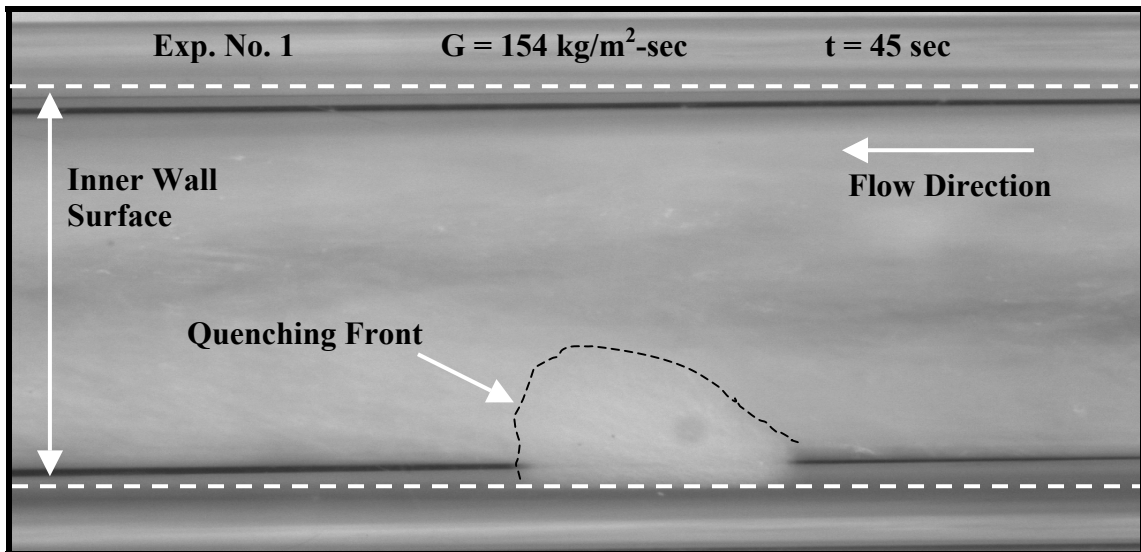


(b)

Figure 3-6. Sequential photographs of the film boiling front as it crosses through the visual test section. (a) $G = 72 \text{ kg/m}^2\text{-s}$, $\bar{T}_w = -28.9^\circ \text{C}$, (b) $G = 72 \text{ kg/m}^2\text{-s}$, $\bar{T}_w = -30.2^\circ \text{C}$, (c) $G = 72 \text{ kg/m}^2\text{-s}$, $\bar{T}_w = -31.4^\circ \text{C}$.

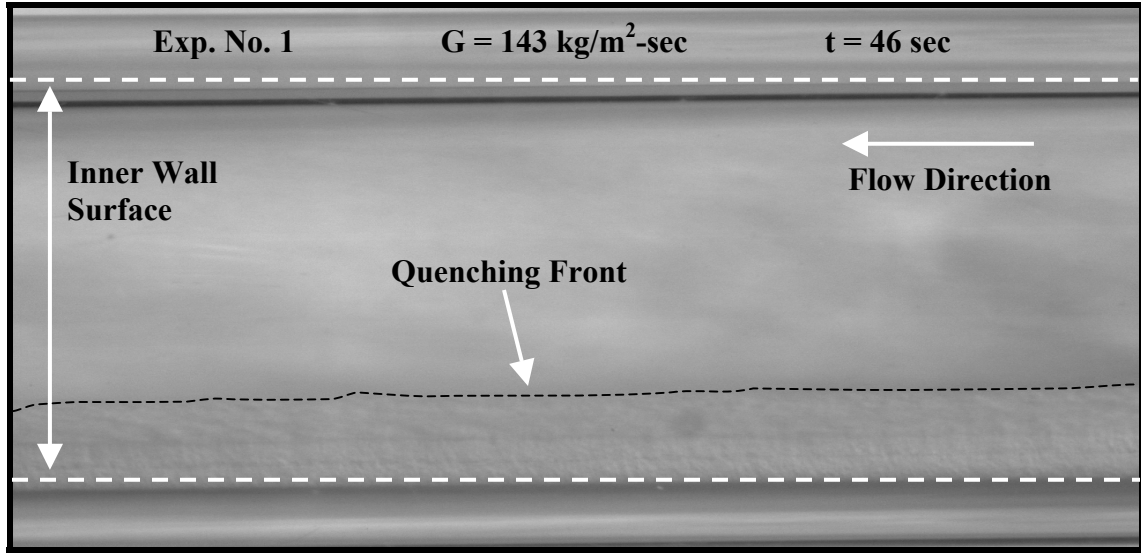


(c)



(a)

Figure 3-7. Sequential photographs of the film boiling front as it crosses through the visual test section. (a) $G = 154 \text{ kg/m}^2\text{-s}$, $\bar{T}_w = -26.7^\circ \text{C}$, (b) $G = 143 \text{ kg/m}^2\text{-s}$, $\bar{T}_w = -28.0^\circ \text{C}$.



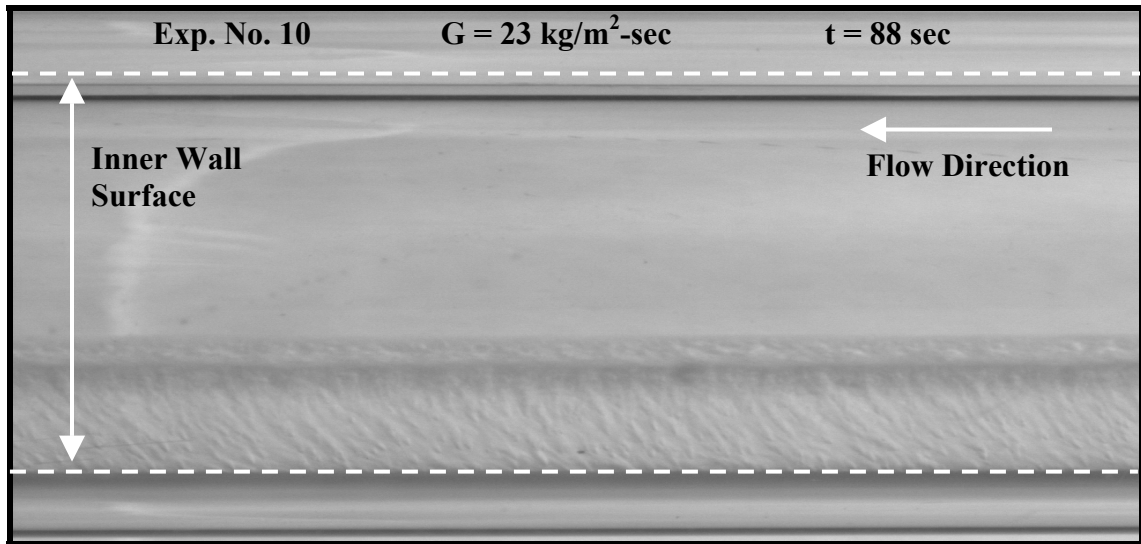
(b)

Figure 3-7. Continued.

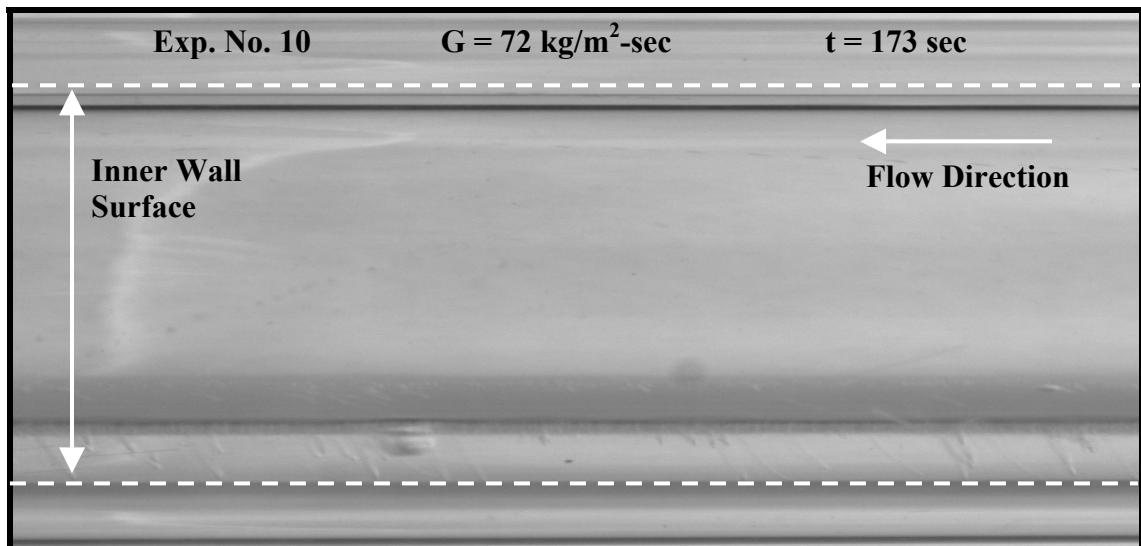
3.2.3 Post Quenching Front Visualizations

The images shown in Figures 3-8 through 3-10 have captured typical events that occur following the quenching front. Following the passing of the quenching front there is a noticeable change in the flow structure and liquid height. Immediately after the quenching front had passed, nucleate boiling was observed in the growing liquid layer. In general the higher the mass flux, the shorter the nucleate boiling regime persisted. After the nucleate boiling had ceased a typical stratified and wavy flow structure occurred. A clearly stratified or wavy flow structure was evidenced in several individual photographs (Figures 3-8(a & b), 3-9(a & b), and 3-10(b)), however due to the rapid fluctuations between the traditionally defined regimes a combined stratified/wavy regime was generally applied to describe the flow structure. At this point in the chilldown process additional flow structure transitions were observed in most of the experiments. As the chilldown process progressed the liquid height in the visual section continued to grow and the flow structure transitioned (in most cases) to slug flow followed by plug

flow. In general as the mass flux was increased the time between these transitions was decreased. In the case of some low mass flux experiments not all of the flow regime transitions occurred and the flow structure remained stratified/wavy for the remainder of the chilldown process as shown in Figure 3-8.

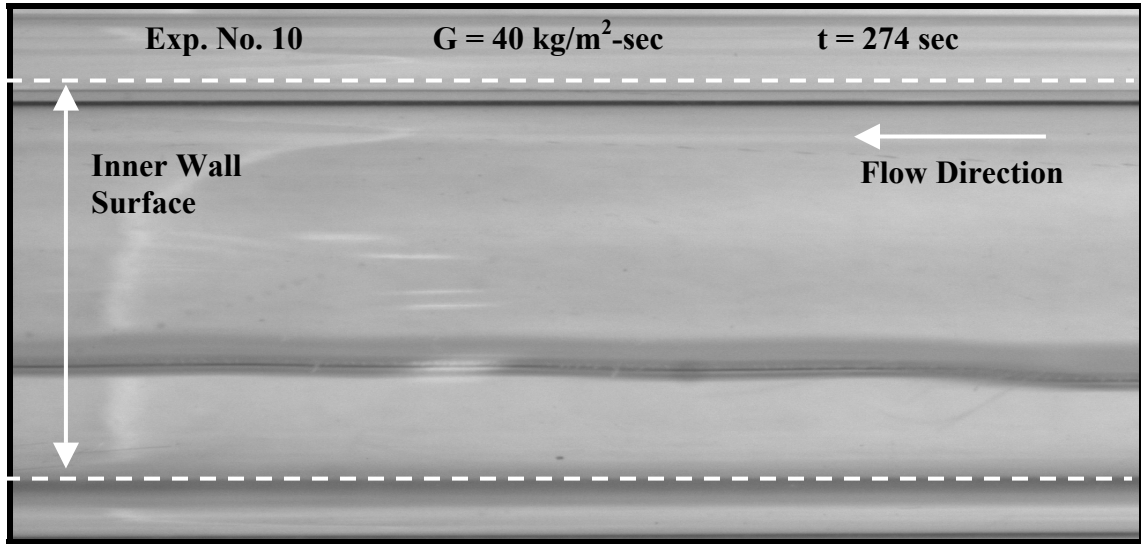


(a)

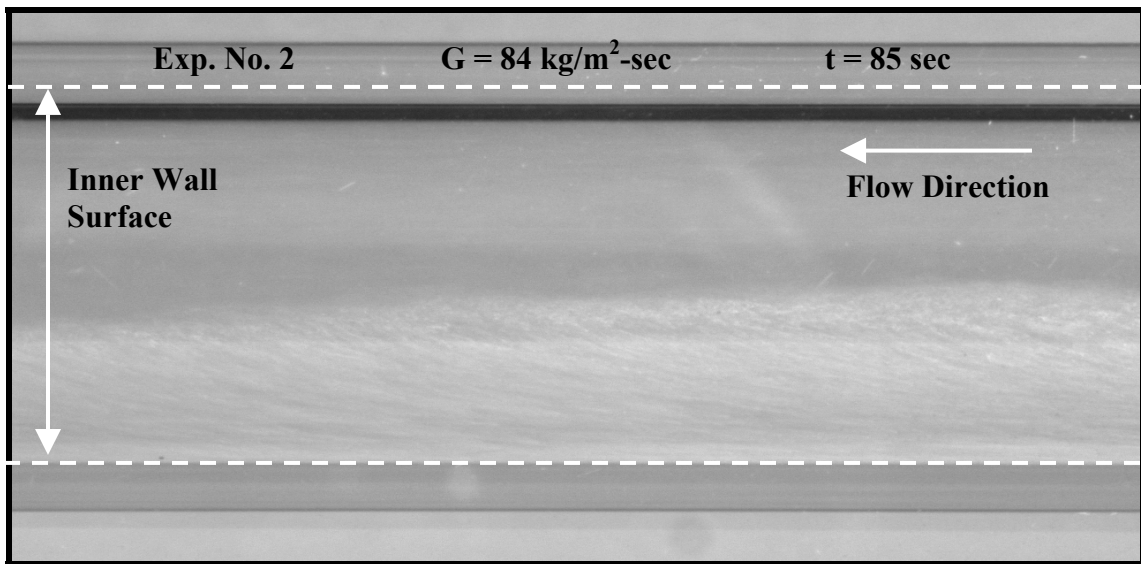


(b)

Figure 3-8. Photographs of the various flow structures observed during the chilldown process following the passing of the film boiling front. (a) $G = 23 \text{ kg/m}^2\text{-s}$, $\bar{T}_w = -18.7^\circ \text{C}$, (b) $G = 72 \text{ kg/m}^2\text{-s}$, $\bar{T}_w = -84.3^\circ \text{C}$, (c) $G = 40 \text{ kg/m}^2\text{-s}$, $\bar{T}_w = -170.6^\circ \text{C}$.

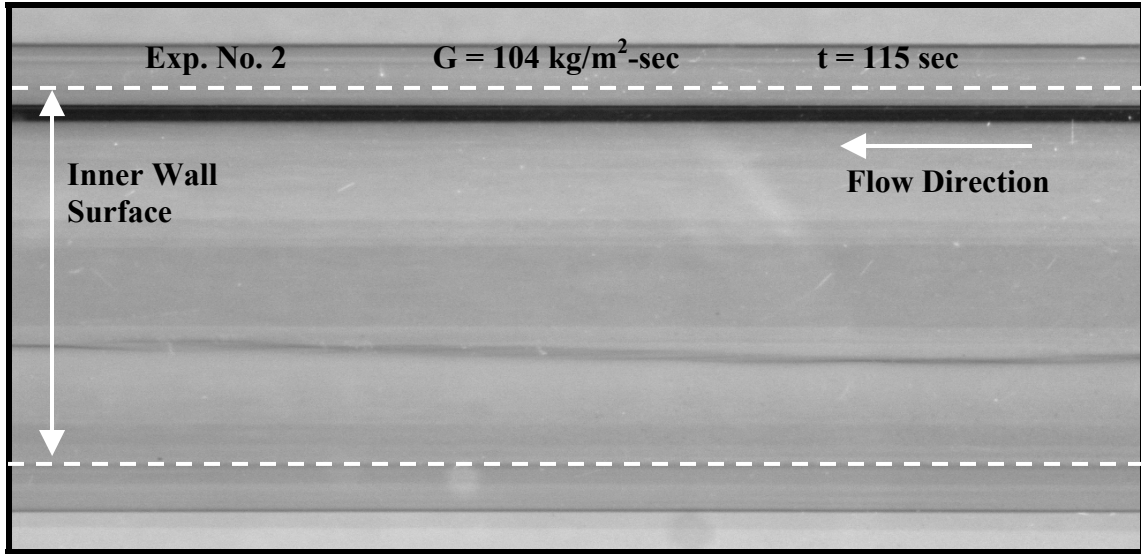


(c)

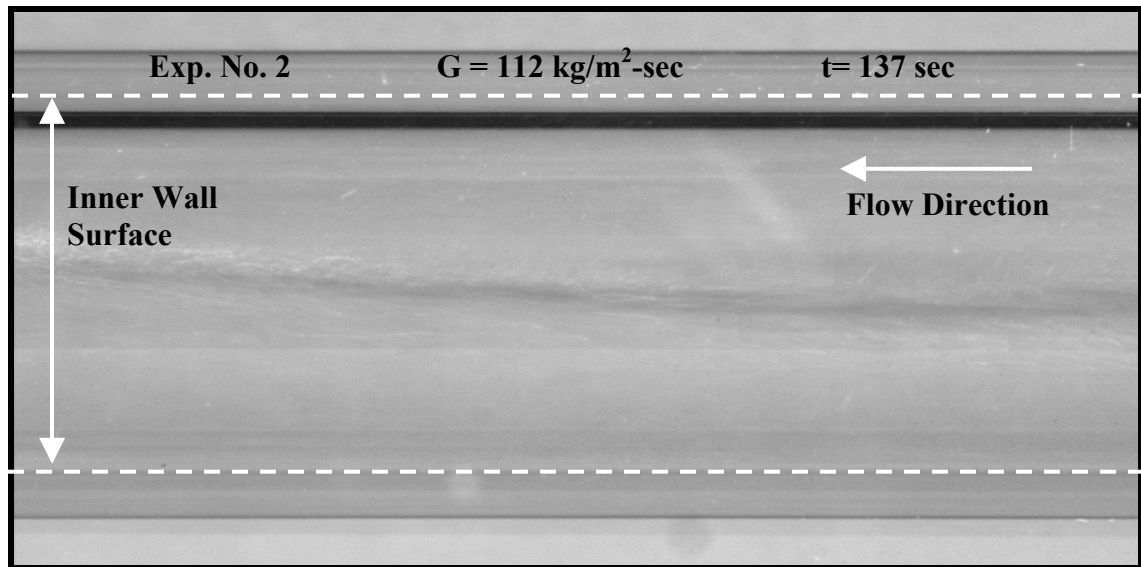


(a)

Figure 3-9. Photographs of the various flow structures observed during the chilldown process following the passing of the film boiling front. (a) $G = 84 \text{ kg/m}^2\text{-s}$, $\bar{T}_w = -59.8^\circ \text{C}$, (b) $G = 104 \text{ kg/m}^2\text{-s}$, $\bar{T}_w = -120.9^\circ \text{C}$, (c) $G = 112 \text{ kg/m}^2\text{-s}$, $\bar{T}_w = -161.6^\circ \text{C}$, (d) $G = 126 \text{ kg/m}^2\text{-s}$, $\bar{T}_w = -175.6^\circ \text{C}$, (e) $G = 150 \text{ kg/m}^2\text{-s}$, $\bar{T}_w = -177.2^\circ \text{C}$.

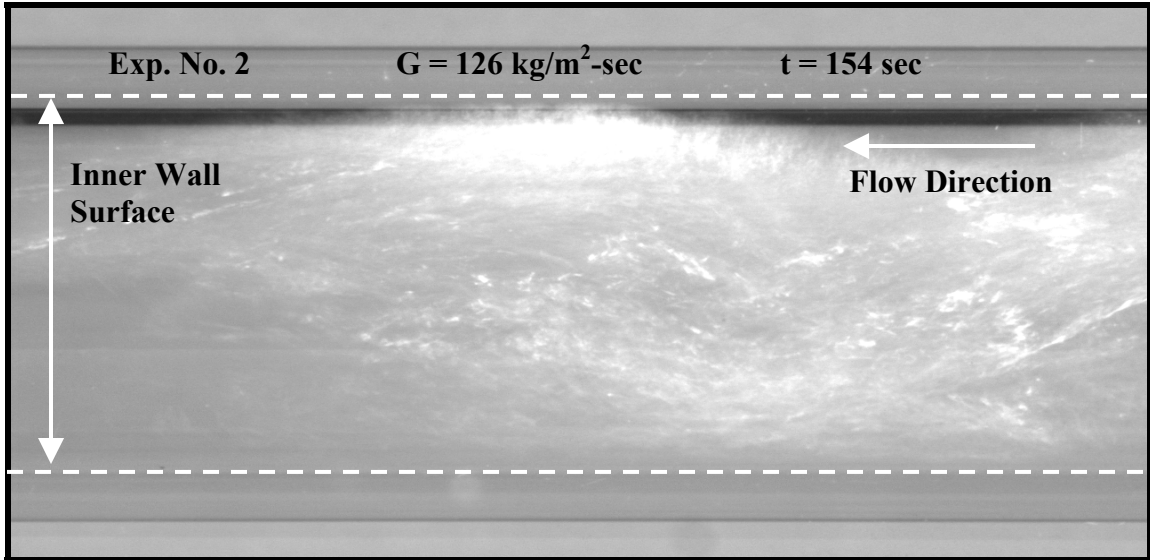


(b)

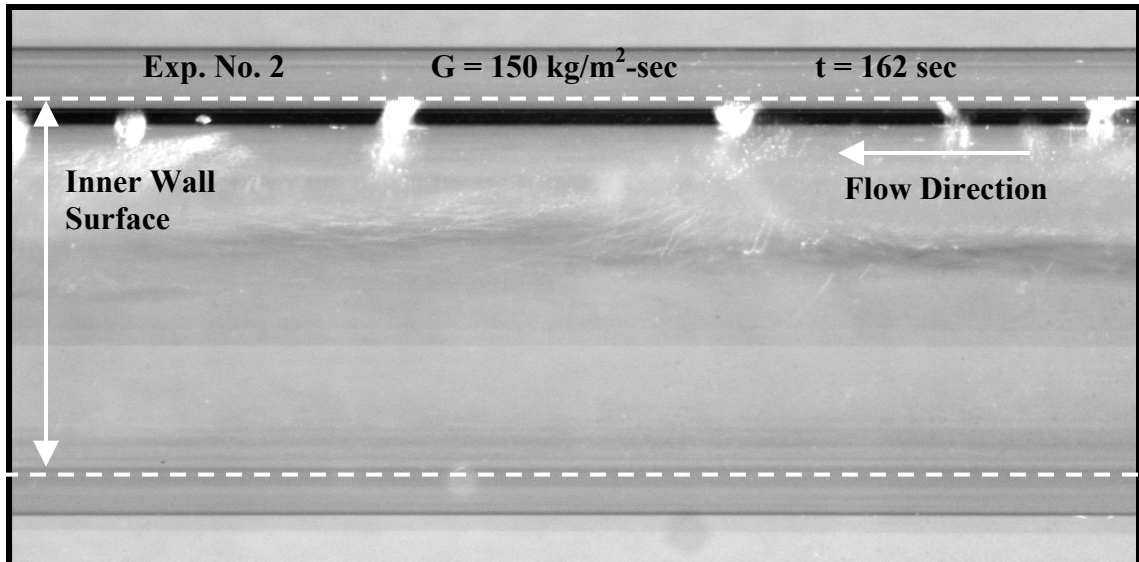


(c)

Figure 3-9. Continued.

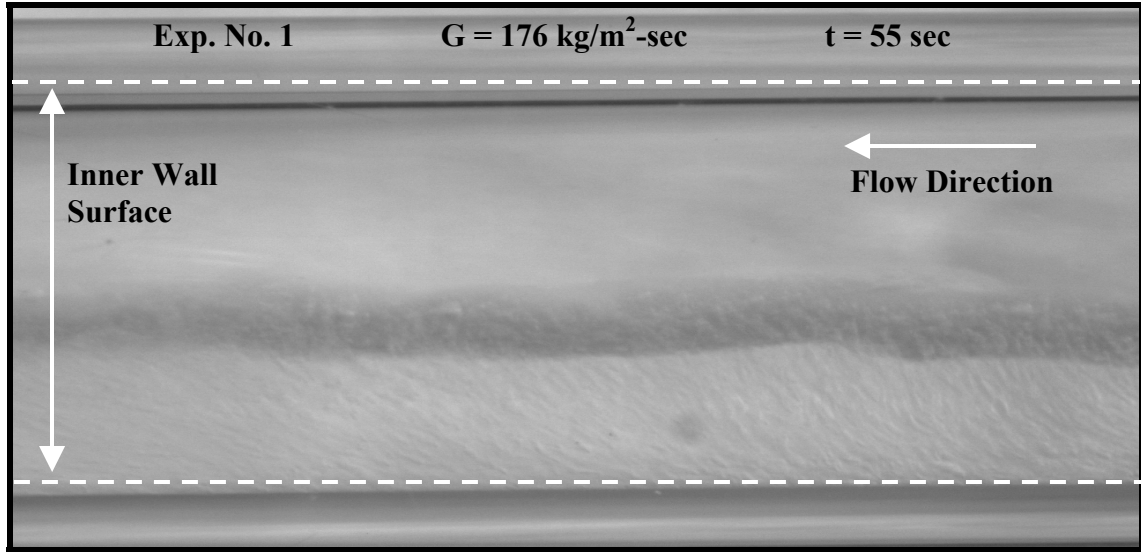


(d)

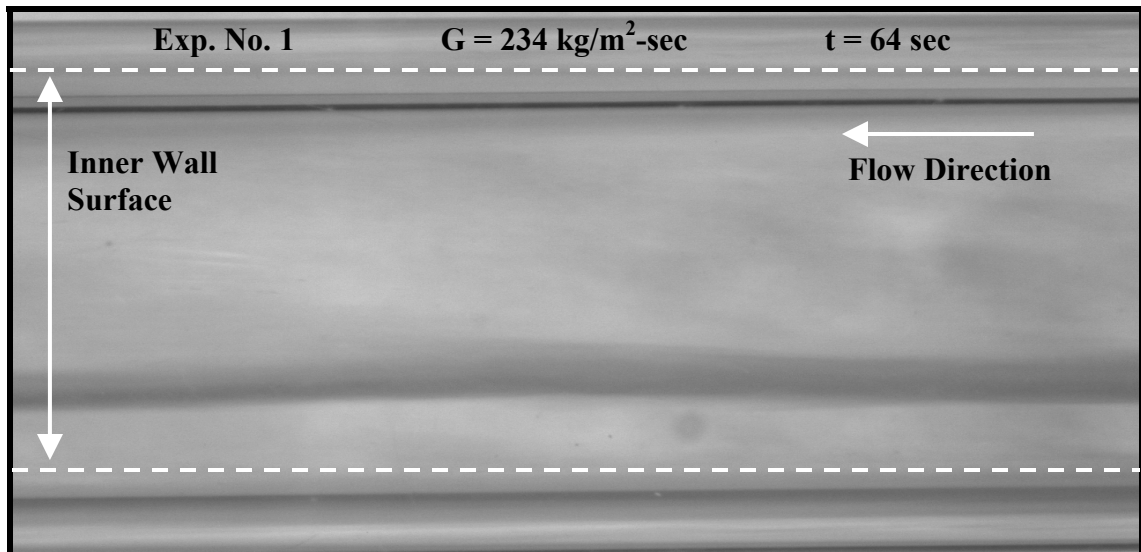


(e)

Figure 3-9. Continued.

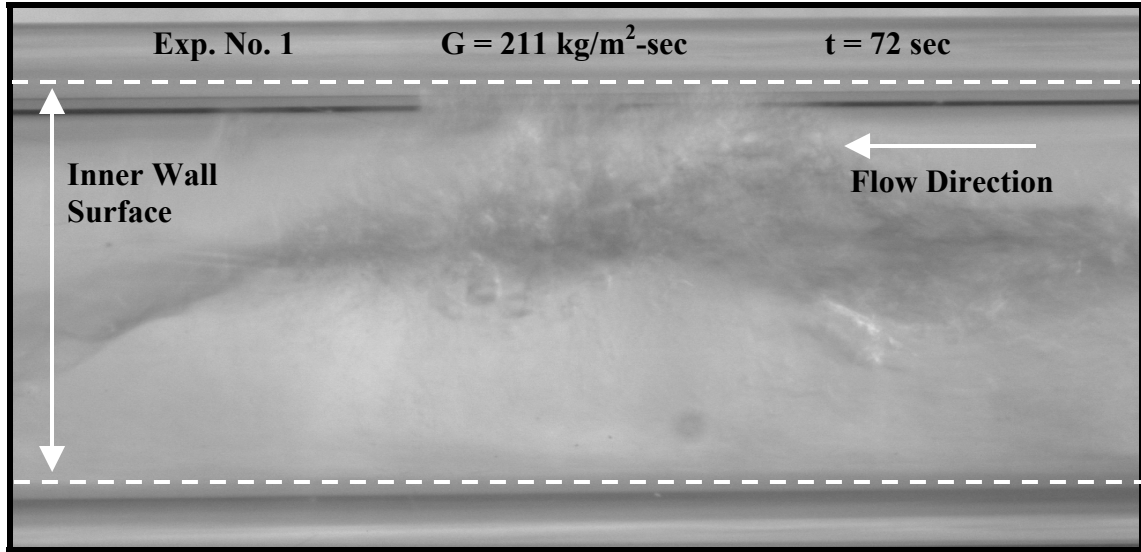


(a)

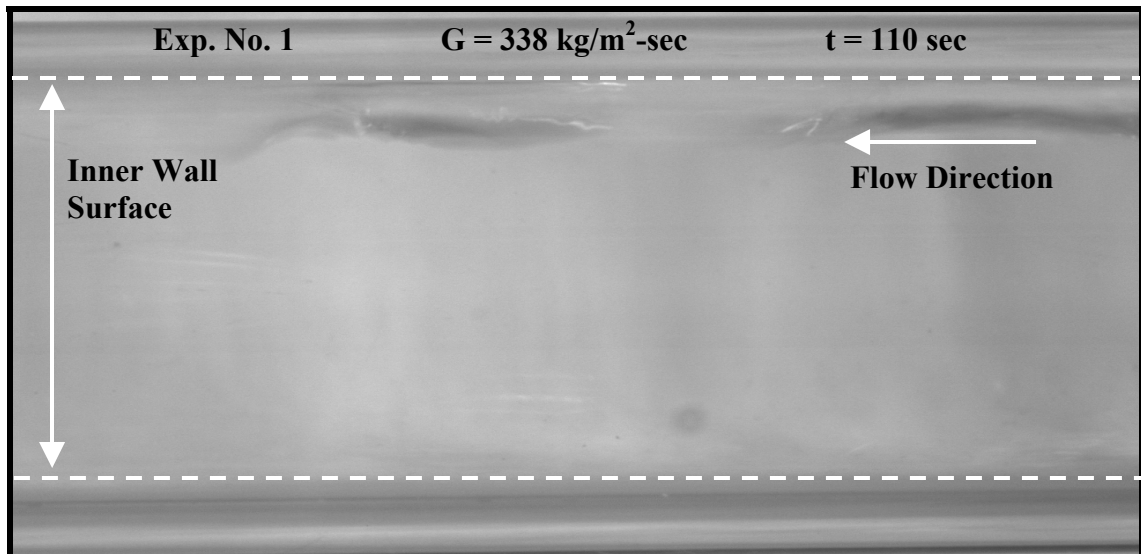


(b)

Figure 3-10. Photographs of the various flow structures observed during the chilldown process following the passing of the film boiling front. (a) $G = 176 \text{ kg/m}^2\text{-s}$, $\bar{T}_w = -39.7^\circ \text{C}$, (b) $G = 234 \text{ kg/m}^2\text{-s}$, $\bar{T}_w = -51.8^\circ \text{C}$, (c) $G = 211 \text{ kg/m}^2\text{-s}$, $\bar{T}_w = -62.5^\circ \text{C}$, (d) $G = 338 \text{ kg/m}^2\text{-s}$, $\bar{T}_w = -178.4^\circ \text{C}$.



(c)



(d)

Figure 3-10. Continued.

3.3 Vapor Volume Fraction and Quality Measurement Results

In addition to providing a visual account of the chillover process the images were also used to compute the vapor volume fraction of the cryogenic two-phase flow. The vapor volume fraction is an important measurement that is essential for estimating the vapor quality and other flow parameters of interest. Previous research has suggested several methods for measuring the vapor volume fraction in cryogenic two-phase flows.

The methods range from a crude approach proposed by Chi and Vetere [16] to capacitance sensor studies by Willis and Smith [21], Killian and Simpson [22], and Khalil et al. [23] to an elaborate radio frequency based sensor approach suggested by Filippov [24].

The approach suggested by Chi and Vetere [16] incorporated a rough average of the measured temperature data from a thermocouple placed inline with the transfer fluid. They proposed a crude relationship relating vapor volume fraction and patterned temperature variations associated with the various chilldown phases. An improvement over this approach was that of the capacitance sensor.

In the capacitance sensor approach capacitance probes were placed in line with the fluid and used to accurately measure fluctuations in the dielectric constant. The changes in the dielectric constant were then related to the void fraction and average density of the two-phase cryogenic flows. Typically the flow regime must be known to accurately use this approach. The limitation of this method resides in the small difference of the dielectric constants of the two phases. The sensor is less sensitive with small differences in the dielectric constant. Willis and Smith [21] and Killian and Simpson [22] have successfully applied this method to measure the average density of two-phase hydrogen. Khalil et al [23] has additionally reported success in measuring the average density of two-phase helium by using an ultra sensitive capacitance circuit.

Filippov's [24] method incorporated a radio frequency based sensor that was used to compute the dielectric constant of the two-phase flow. This method is similar to that of the capacitance sensor approach with the one difference being the use of a radio frequency sensor. The radio frequency sensor has greater sensitivity and was used to

address the very small difference of dielectric constants between the two phases. The method is limited to stable flow structures due to the non-uniform electric field energy distribution associated with flow structure variations. For the present study, the visual method is used to measure the volume fraction due to its simplicity.

The results of the vapor volume fraction measurements and the vapor quality for the previously discussed experiments are presented in Figures 3-11 through 3-13. The figures display the raw transient vapor volume fraction measurements; a smoothed fit for the vapor volume fraction, and the computed vapor quality. The raw vapor volume fraction data illustrates the unsteady and highly varied flow structure during chilldown. To capture the general chilldown trend, a smooth curve was fit to the raw vapor volume fraction data. As discussed in Section 2.7 the Zuber and Findlay [13] relation is used to estimate the vapor quality from the smoothed volume fraction data. The wavy contour of the quality curve results from the unsteady mass flux during chilldown, which is attributed to the considerable fluctuations in the vapor velocity measured at the venturi. In addition to the vapor volume fraction and quality data, the figures were also demarcated with lines indicating where the observed flow structure transitions occurred.

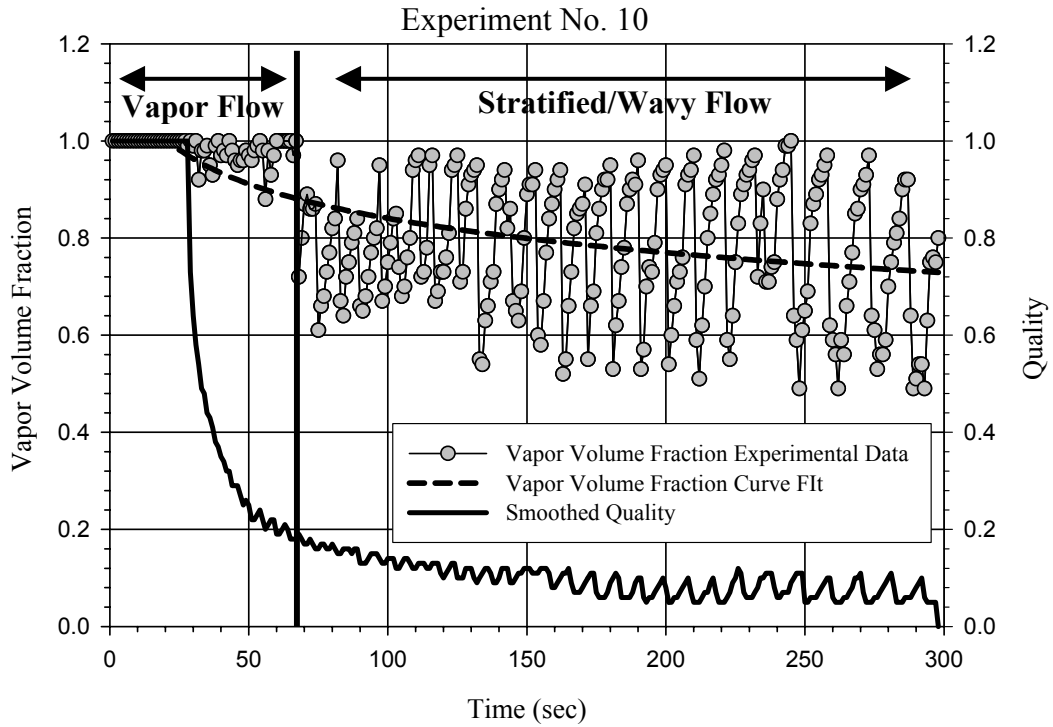


Figure 3-11. Graph of the vapor volume fraction and quality for experiment # 10.

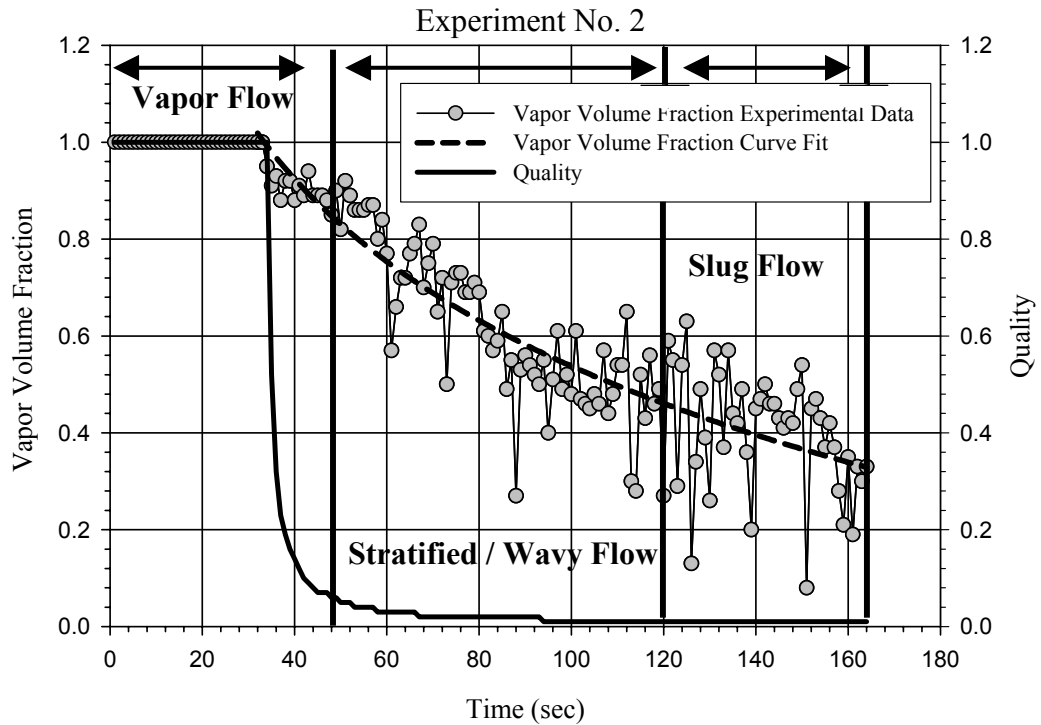


Figure 3-12. Graph of the vapor volume fraction and quality for experiment # 2.

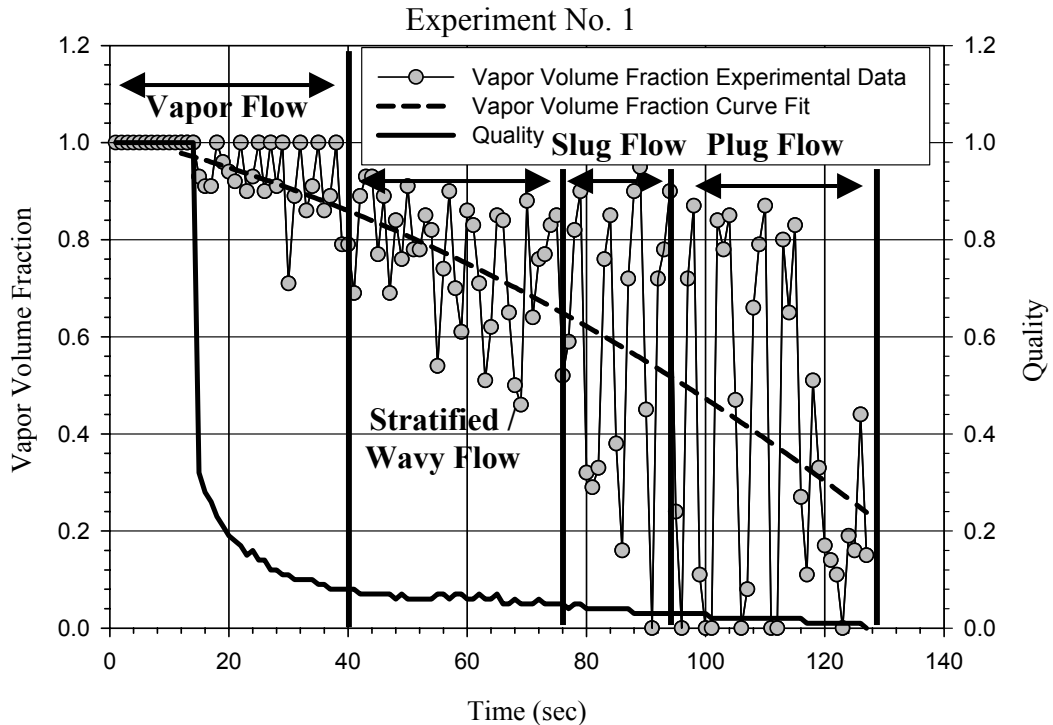


Figure 3-13. Graph of the vapor volume fraction and quality for experiment # 1.

3.4 Discussion of Results

The visual observations of the cryogenic chilldown experiments have confirmed and improved upon the previous work of Bronson et al. [2] and Chi and Vetere [16] regarding the general flow structure and heat transfer sequence. As noted in the literature review section of this chapter, Bronson and Chi and Vetere both conducted flow visualization studies of cryogenic chilldown. Bronson's facility was operated at pressures as high as 6900 kPa with mass fluxes up to 3100 kg/m²-sec, while Chi and Vetere, who did not report an operating pressure, examined mass fluxes of 0.25 kg/m²-sec. Bronson reported the chilldown process to begin with gas being vented from the system, followed by the presence of droplets of liquid cryogen that were transported through the length of the visual section before the line was cooled down. Pulses of liquid, which flashed into gas, then reportedly followed. Subsequently an advancing front of stratified flow that rapidly transitioned into a slug flow phase emerged. The slug flow phase persisted until the slugs

gradually coalesced filling the visual section with liquid. Chi and Vetere reported a chilldown sequence similar to that of Bronson with additional consideration for the prevailing heat transfer regimes. Chi and Vetere reported the existence of film boiling that persisted through the mist flow and slug flow regimes. The film boiling was reportedly followed by a short transitional boiling phase, which was then followed by nucleate boiling. The results of the current research differ moderately with the general descriptions of the chilldown events offered by Bronson and Chi and Vetere. The current research offers much greater detailed description of the chilldown sequence and occurrence of heat transfer regimes. In the current research, the early phase where pulses of liquid, which flashed into gas, described by Bronson were not specifically observed. Additionally, the current research did not observe the film boiling heat transfer phenomena to continue throughout the slug flow regime as indicated by Chi and Vetere. Instead film boiling was observed to occur in the initial stages of chilldown and subsided following the passing of the quenching front. Furthermore no transitional boiling stage was observed.

The vapor volume fraction and quality curves of the experiments appear to be in general agreement with the visually observed chilldown trend. The unstable nature of the chilldown process is also evidenced in the plots of the vapor volume fraction data. The data reveal the wide fluctuations and instability of the chilldown process. Despite these wide fluctuations a general trend was observed and smoothed. The graphs also indicate an approximate area where the flow regime transitions were visually observed. The observed flow regime transitions appear to occur earlier in time and are typically shorter in duration as the mass flux of the experiments increased. This general trend was

observed in the majority of experiments with a single noteworthy exception. In one particular experiment flow instability occurred, which resulted in a deviation from the general chilldown trend. A plot of the vapor volume fraction data from this experiment is presented in Figure 3-14 for the purpose of comparison.

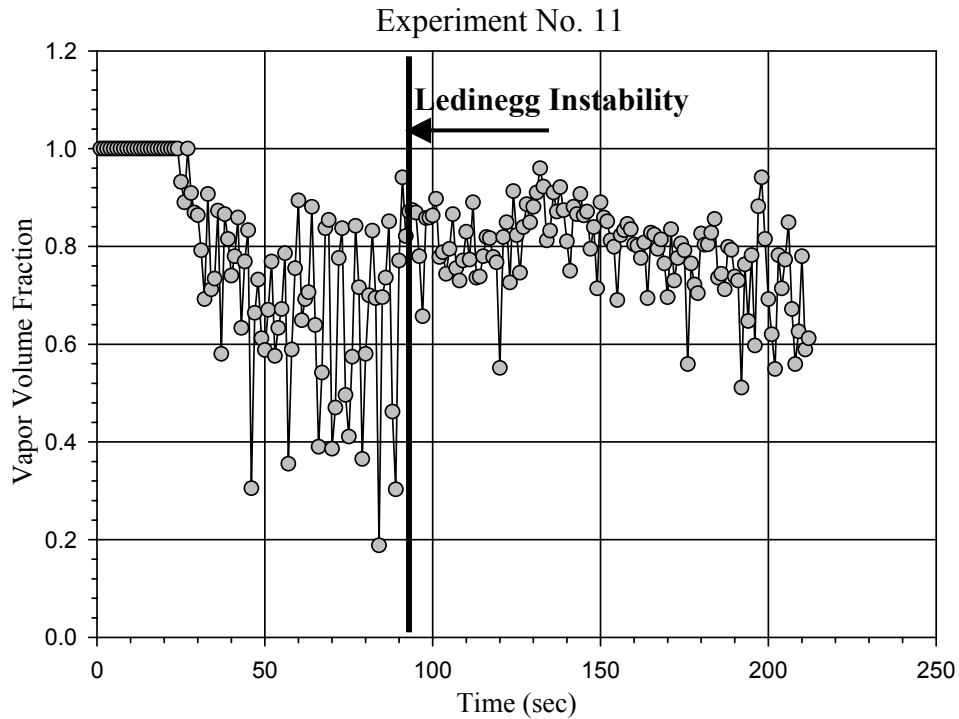


Figure 3-14. Graph of the vapor volume fraction data for experiment # 11.

It is believed that this digression from the typical chilldown sequence is a result of a Ledinegg-instability. When a Ledinegg-instability occurs the flow can exhibit multiple states and is subject to an oscillatory instability referred to as a density wave oscillation. The density wave oscillation is caused by the delay in the system due to the fluid transport time. This experiment was the only record of such an occurrence and future investigations into the frequency and general behavior of such an event have yet to be conducted.

3.5 Sources of Experimental Error

The image analysis procedure is subject to moderate uncertainty due to the highly unstable nature of the flow structure during chilldown, the image capture rate of the camera system, and qualitative and subjective human bias. During the chilldown experiments the liquid height in the visual test section fluctuates considerably. This constant variation in the liquid height throughout the visual test section limits the accuracy of the liquid height measurements. In addition to the variation in the liquid height, the actual flow structure also can inhibit the accuracy of the measurements. Highly unstable flow structures may contain entrained vapor and/or a wavy interface within the image. In these situations an approximate interface line was assumed from which several liquid height measurements were averaged. Two people, one of whom had limited knowledge of the experiment, analyzed the images from several experiments. The results of each analysis were compared in an attempt to quantify this error. It was found that on average the selected liquid heights identified by each examiner were fairly similar with deviations typically around 1.0 millimeter or less. The largest variations in measurements came during the beginning of the experiments where the interface was not very clear. The largest deviation reported during the initial part of chilldown was approximately 1 mm while during the later stages the error was much less than 0.5 mm. As result of the squaring of the height term in the vapor volume fraction computation the larger error in the beginning of the experiment resulted in an uncertainty of approximately 1.5 % while the error in the later stages of chilldown where the interface resolution was greater produced an approximate error of 7 %. This experimental uncertainty is reasonable and compares to the reported uncertainty from the previously

mentioned methods for determining the vapor volume fraction. Additional uncertainty arose from the sequencing of the camera rate and the data acquisition program.

During the chilldown experiment the data acquisition system was initiated first and followed by the camera system. The two independent programs were both selected to record data at one-second intervals however; a varied lag often persisted between the two systems. The lag was on the order of one second and could not effectively be accounted for. In addition to the lag during startup it was found that the camera system often recorded the images at a rate slightly faster than one second. The total variation in time resulting from this deviation was typically less than a second for an entire experiment and thus it was considered negligible. Exhaustive efforts that were made to remedy these variations were met with limited success, and it was concluded that the resultant error was comparatively small and tolerable. In addition to the camera sequencing error it was also observed that the transitioning flow structures did not precisely occur. For example, on occasion it was observed that wavy flow may briefly transition to slug flow and quickly appear to transition back to wavy flow. To account for the wavering transitioning behavior during chilldown as well as any error in precisely identifying a single transitioning event a general transition range was applied in regards to flow structure changes. The transitioning range varied by experiment and typically spanned several seconds in duration. It is also recognized that the identification of flow regimes is subject to the qualitative assessment of the images.

The image analysis procedure was a time consuming process by which an individual must continually make an educated judgment concerning the precise identification of the liquid level height and flow

CHAPTER 4
WALL TEMPERATURE PROFILES AND CHILLDOWN TIME IN CRYOGENIC
HORIZONTAL FLOW

4.1 Introduction and Literature Survey

The ability to accurately predict the chilldown time and temperature profile of cryogenic transfer lines during the initial cooldown phase is of significant design and operational importance to the cryogenic industry. Knowledge of the temperature gradients, temperature history, and chilldown time will allow practitioners to design safer transfer systems optimized for efficiency. A number of previous studies have been conducted regarding the chilldown process, which have produced several general chilldown models. These efforts have been collectively addressed in the introductory chapter as well as Section 3.1, and thus only a brief overview of their contributions pertaining to the thermal aspects of chilldown is discussed.

An early approach suggested by Burke et al. [1] applied an energy and mass balance to a defined control volume that included the outer wall of the transfer line. The model assumed an infinite heat transfer coefficient between the transfer line wall and the fluid and consequentially underestimated the chilldown time of the system.

Subsequent work conducted by Bronson et al. [2] was done to investigate general chilldown concerns relating to the development of nuclear powered rocket engines. The research focus included studies of circumferential temperature gradients and chilldown times. Bronson assumed a uniform temperature difference between the pipe wall and

fluid temperature of 10°K. Solving a heat balance the pipe temperature was determined through trial and error until convergence was reached with the known exit gas temperature.

Steward et al. [5] proposed another simplified model for chilldown time. Their model identified the resistance to flow of the vaporized liquid as a critical factor in controlling chilldown.

An investigation was also conducted by Chi [9]. In his examination of hydrogen chilldown it was observed that a film boiling front was present when the wall to fluid temperature difference exceeded 18.5°F. From this observation he reasoned that the heat transfer from the pipe to the two-phase fluid must first be transferred through the vapor of the film boiling front and therefore a pseudo single-phase gas heat transfer relation was assumed. Combining a relation for the heat balance of the fluid with a relation for the local heat flux of the gas phase, Chi derived a relationship for the chilldown time. Chi's model was an improvement over the previous models but still lacked consideration of the two-phase nature of the fluid, wall temperature gradients, fluctuations in the flow rate, and heat transfer from the surroundings.

It is recognized that these additional considerations dramatically increase the complexity of the problem and are not amenable to closed-form analytical solutions. It is the intent of the current research to examine these considerations and provide a sufficient experimental database of chilldown information for the development of advanced chilldown numerical models.

4.2 Wall Temperature Profile and History

To measure the wall temperature profile and history a section of the transfer pipe was externally instrumented with a series of eight thermocouples as shown in Figure 4-1. The

thermocouples were arranged circumferentially in two groups of four around the external surface of the transfer line approximately one meter down from the center of the visual test section. The thermocouple groups were spaced approximately 8 cm apart and insulated with Melamine foam insulation. Measurements were recorded by the data acquisition system at a frequency of 50 Hz and averaged into one-second increments. The chilldown times, experimental mass flux ranges, quenching front observation times, quenching front speeds, and the approximate Leidenfrost temperatures are tabulated in Table 4-1 and followed by the individual temperature and mass flux histories for the first 10 experiments, shown in Figures 4-2 through 4-21. Demarcations on the temperature histories have been added to identify flow structure transitions, the approximate Leidenfrost point, and the visually observed transition from film boiling to nucleate boiling. The visually observed transition from film boiling to nucleate boiling is designated with an oval on each of the temperature histories. The Leidenfrost temperature was identified on the temperature plots by the rapid drop in temperature associated with the transitioning from film-boiling to nucleate boiling. The Leidenfrost temperature is denoted with a dotted line and the approximate transition point was selected based on the temperature history of the thermocouples located on the bottom of the transfer line.

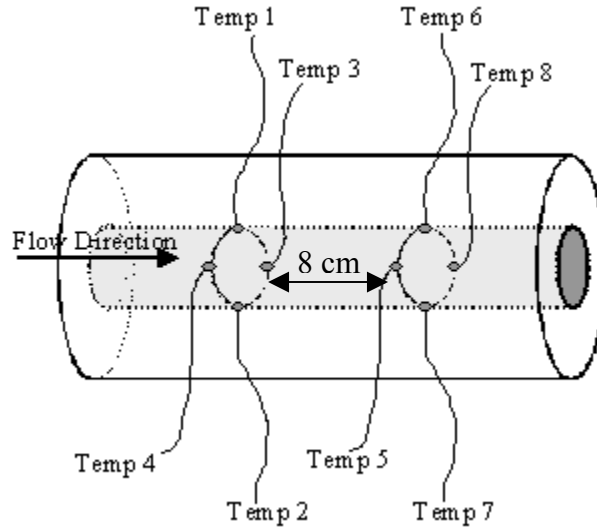


Figure 4-1. Schematic representation of the thermocouple arrangement on the stainless steel transfer line.

Table 4-1. Summary of the chilldown data from the temperature histories.

Experiment Number	Mass Flux Range (kg/m ² -sec)	Approximate Quenching Front Velocity (m/sec)	Approximate Chilldown Time ** (sec)	Quenching Front Observation Time ** (sec)	Approximate Leidenfrost Temperature (°C)
1	125-250	0.052	71	32	-146
2	50-90	0.021	110	43	-144
3	40-120	0.016	145	43	-146
4	200-260	0.062	46	27	-144
5	200-400	0.047	51	24	-148
6	200-350	0.056	54	28	-152
7	125-250	0.047	75	28	-152
8	150-270	0.032	95	32	-148
9	30-60	0.016	197	38	-156
10	20-50	0.019	245	50	-144

** The reported times are referenced to t_i , the time at which chilldown was initiated.

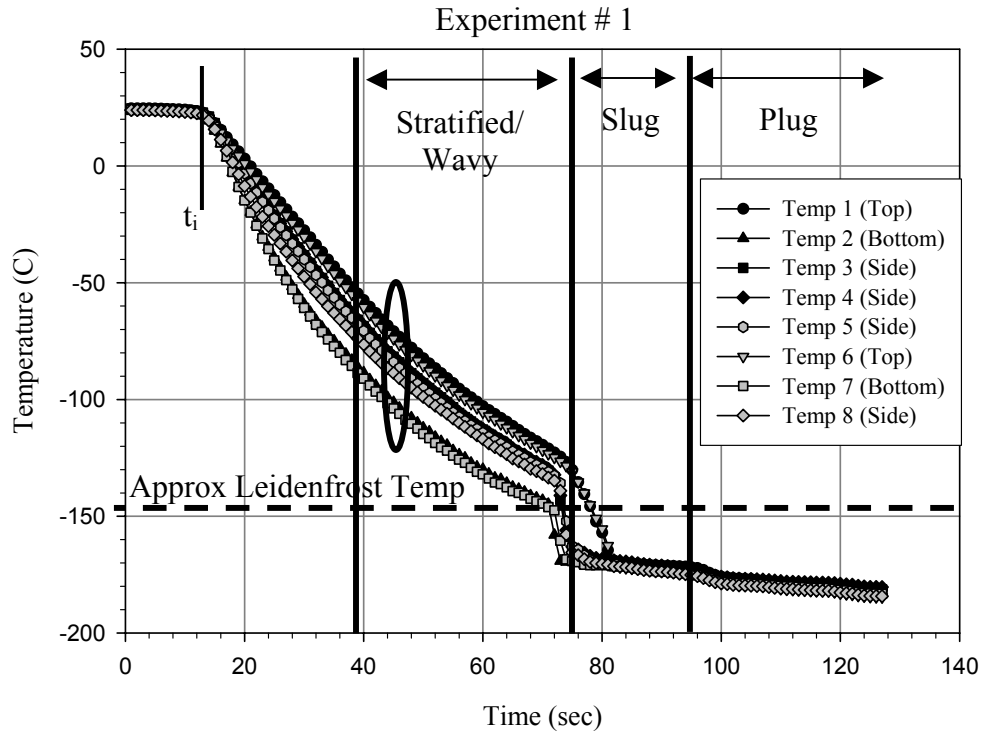


Figure 4-2. Temperature history during chilldown for experiment # 1.

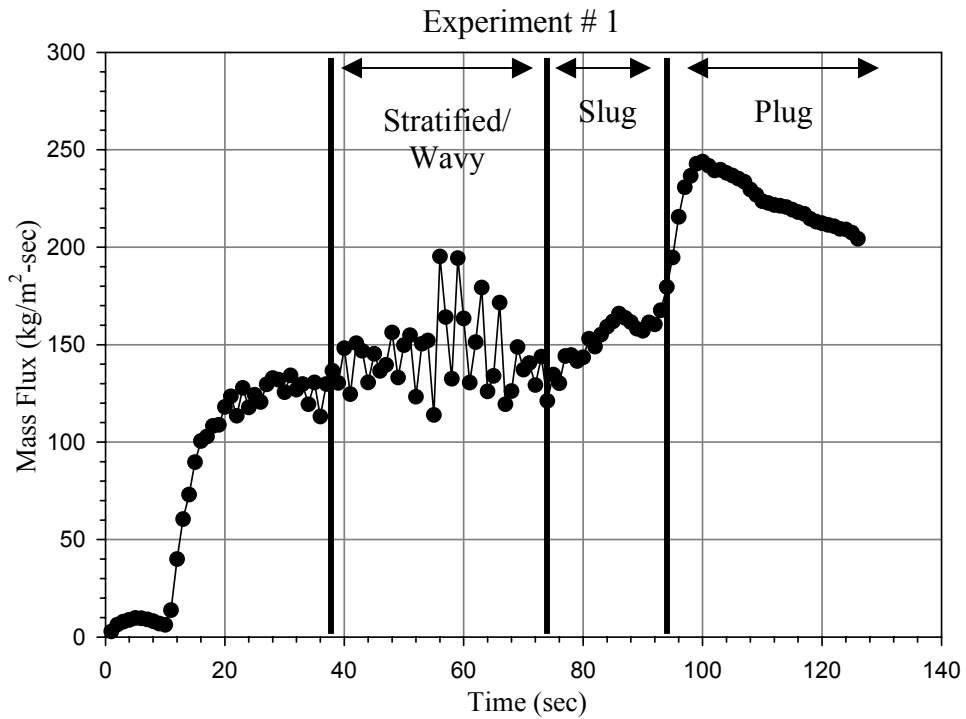


Figure 4-3. Mass flux history for experiment # 1.

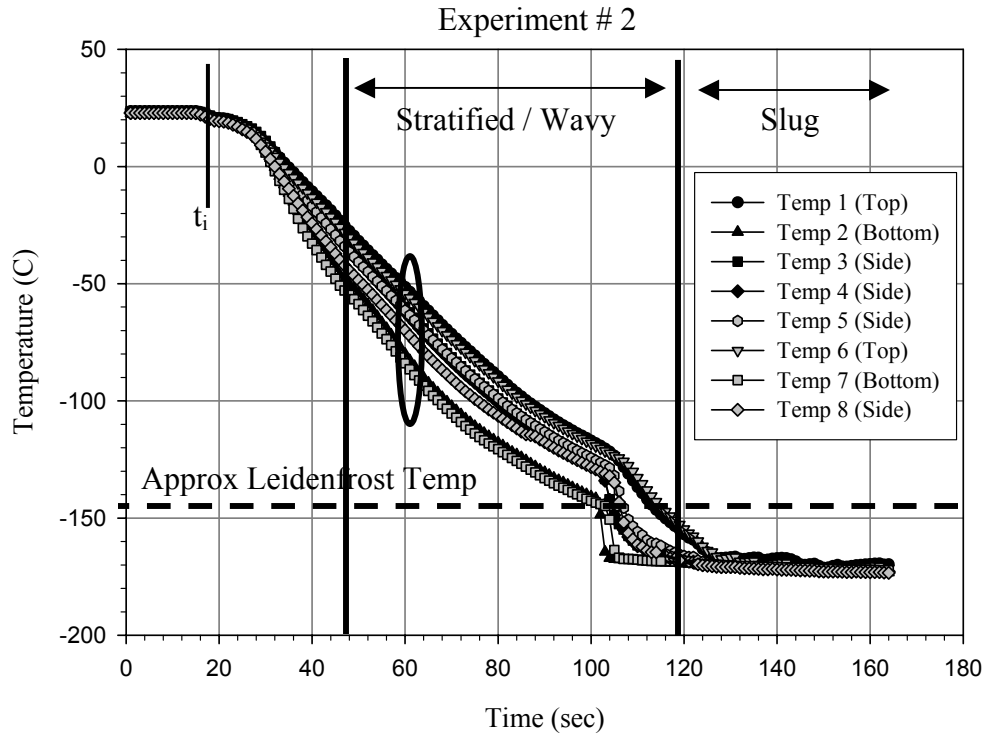


Figure 4-4. Temperature history during chilldown for experiment # 2.

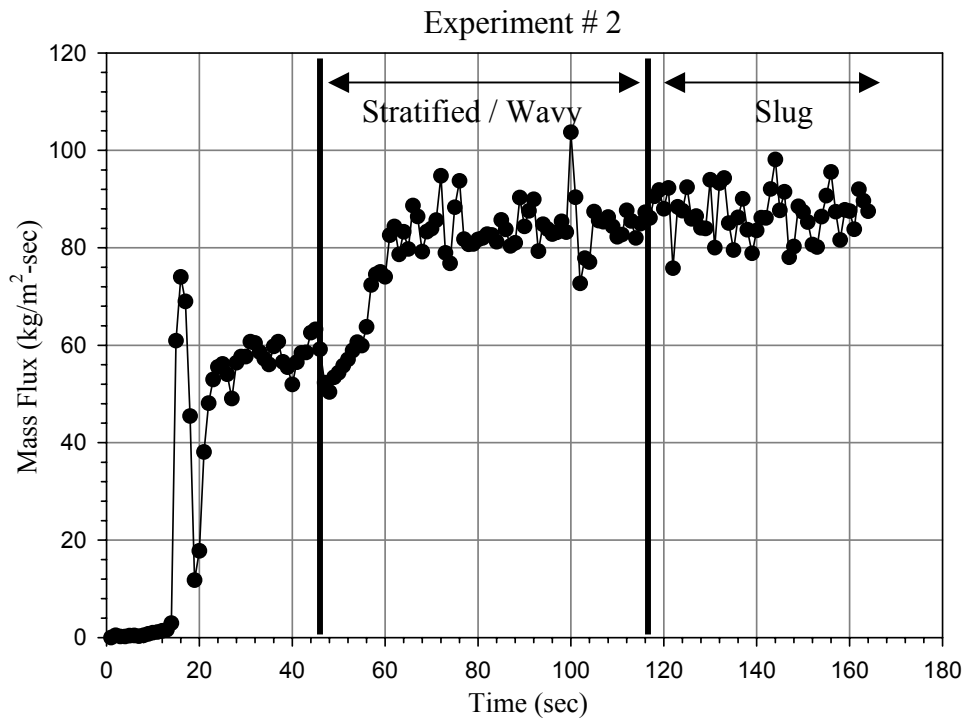


Figure 4-5. Mass flux history for experiment # 2.

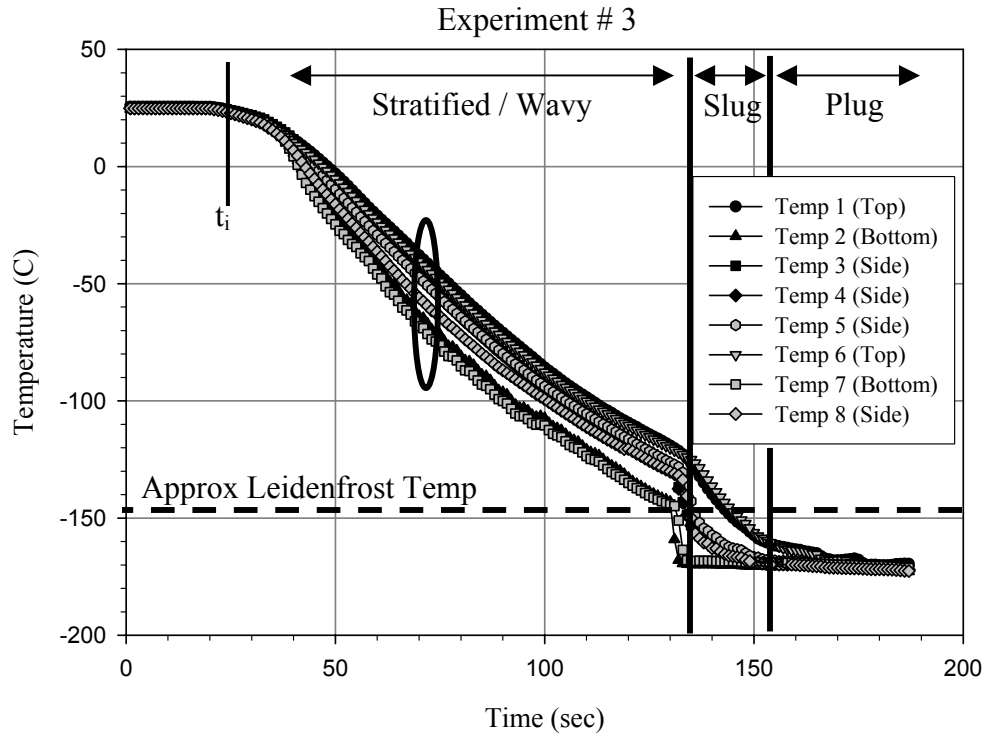


Figure 4-6. Temperature history during chilldown for experiment # 3.

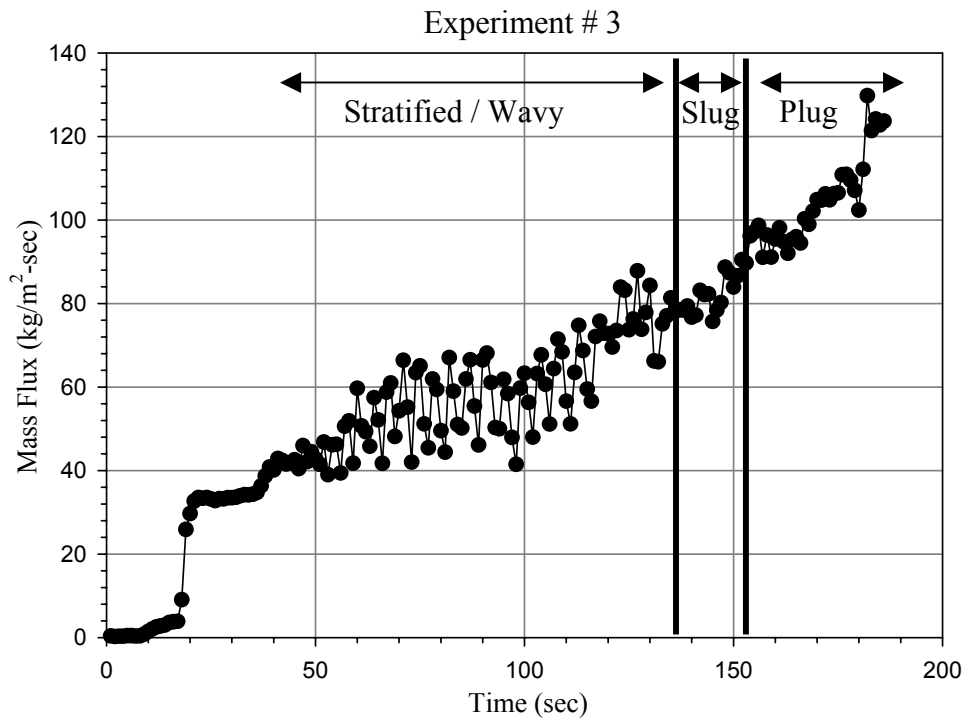


Figure 4-7. Mass flux history for experiment # 3.

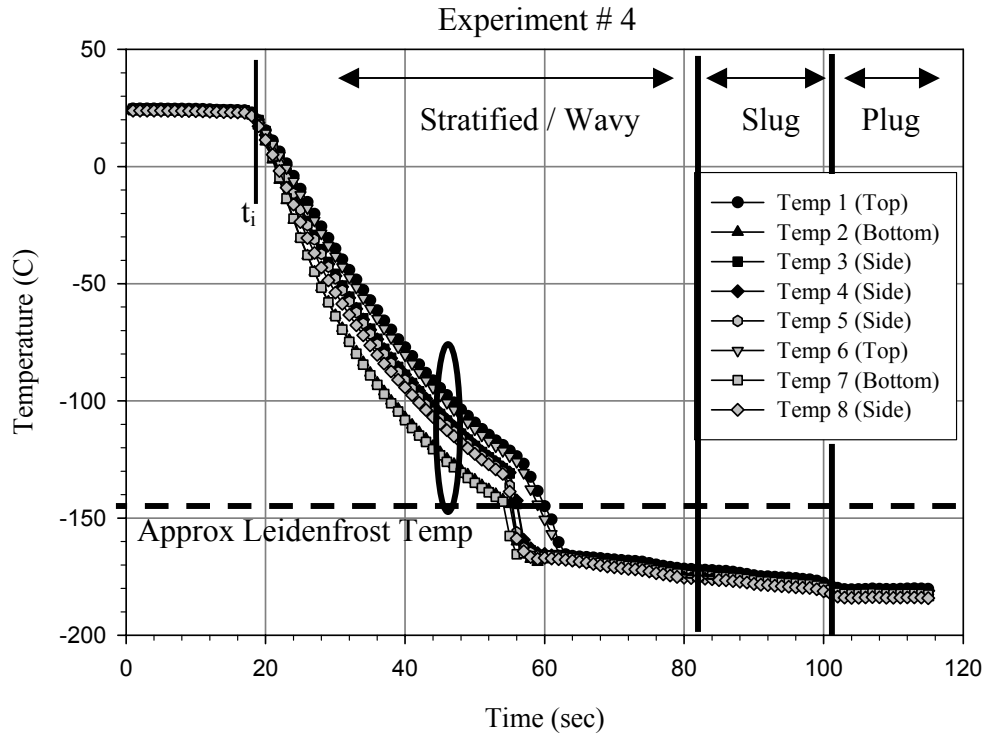


Figure 4-8. Temperature history during chilldown for experiment # 4.

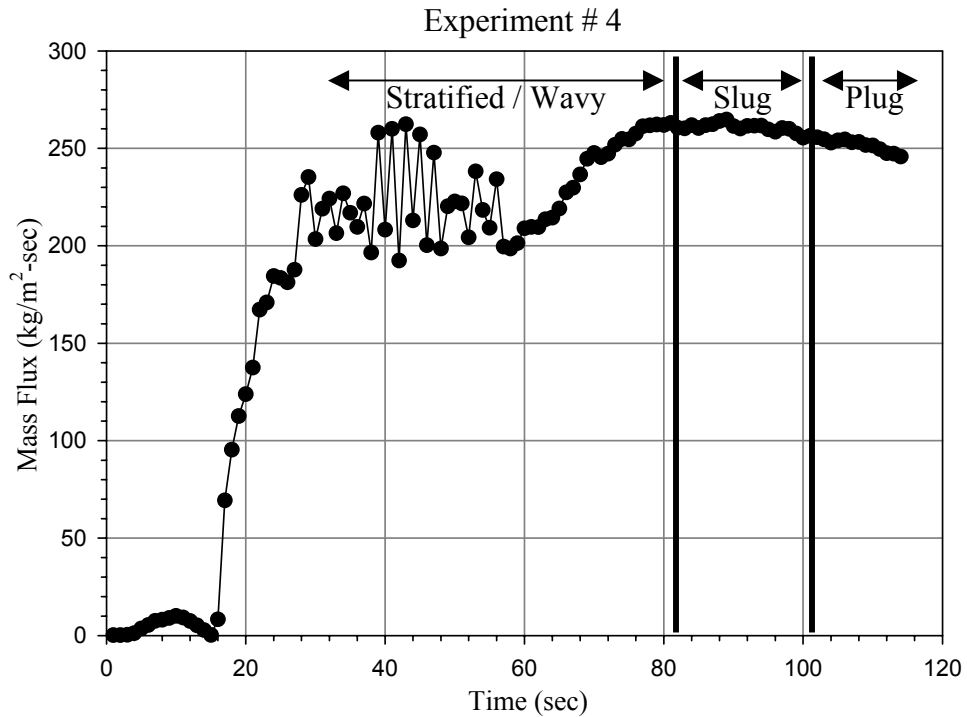


Figure 4-9. Mass flux history for experiment # 4.

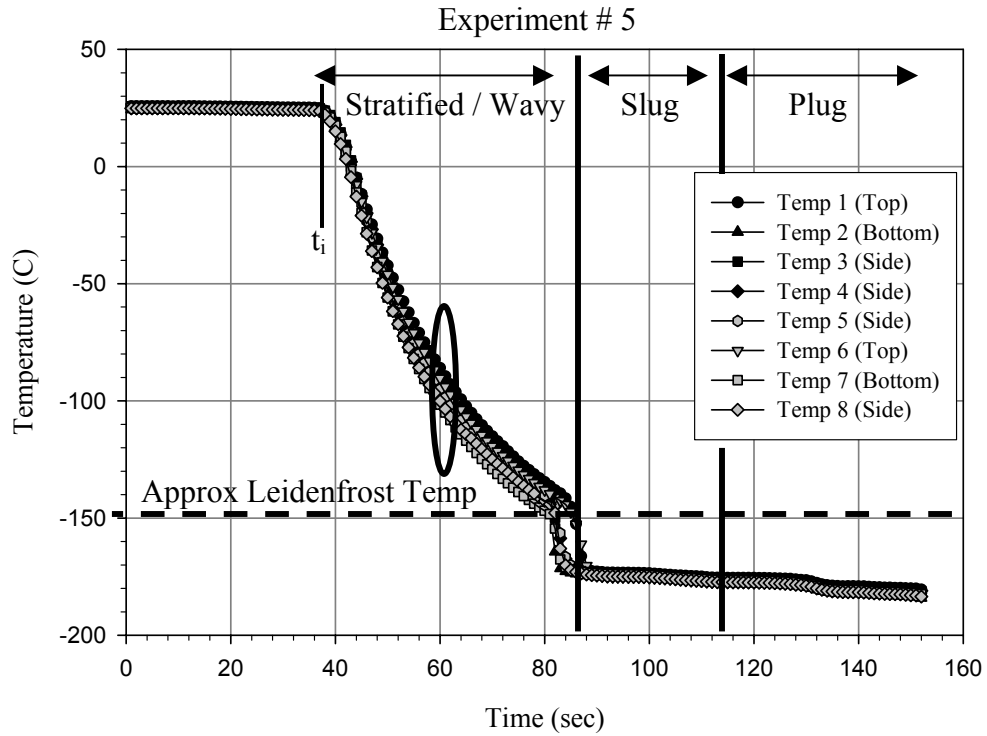


Figure 4-10. Temperature history during chilldown for experiment # 5.

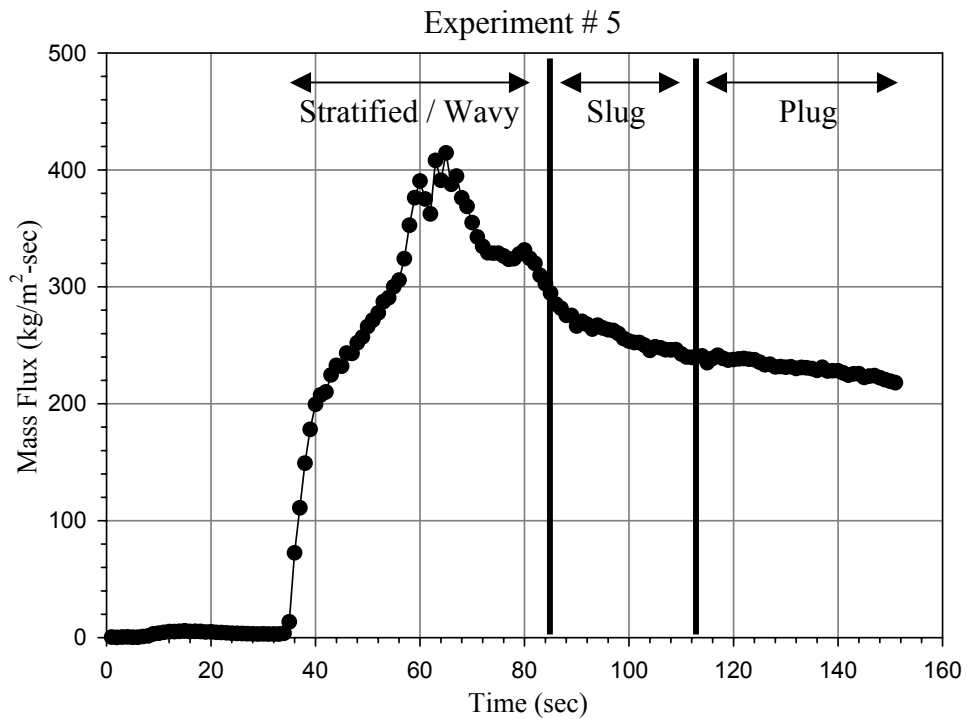


Figure 4-11. Mass flux history for experiment # 5.

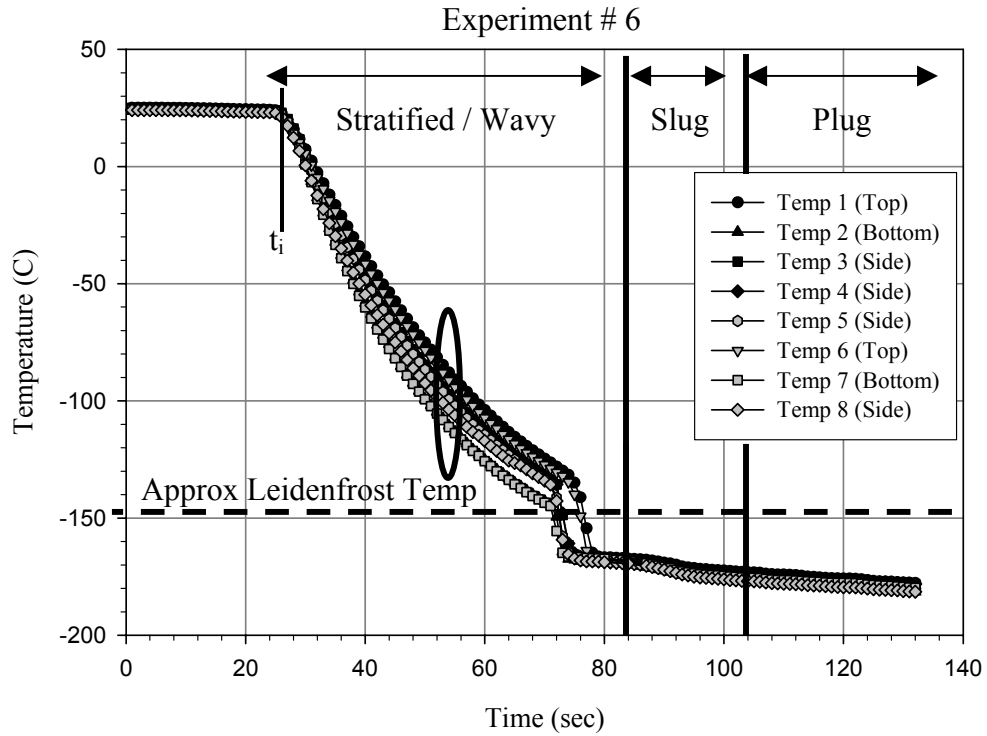


Figure 4-12. Temperature history during chilldown for experiment # 6.

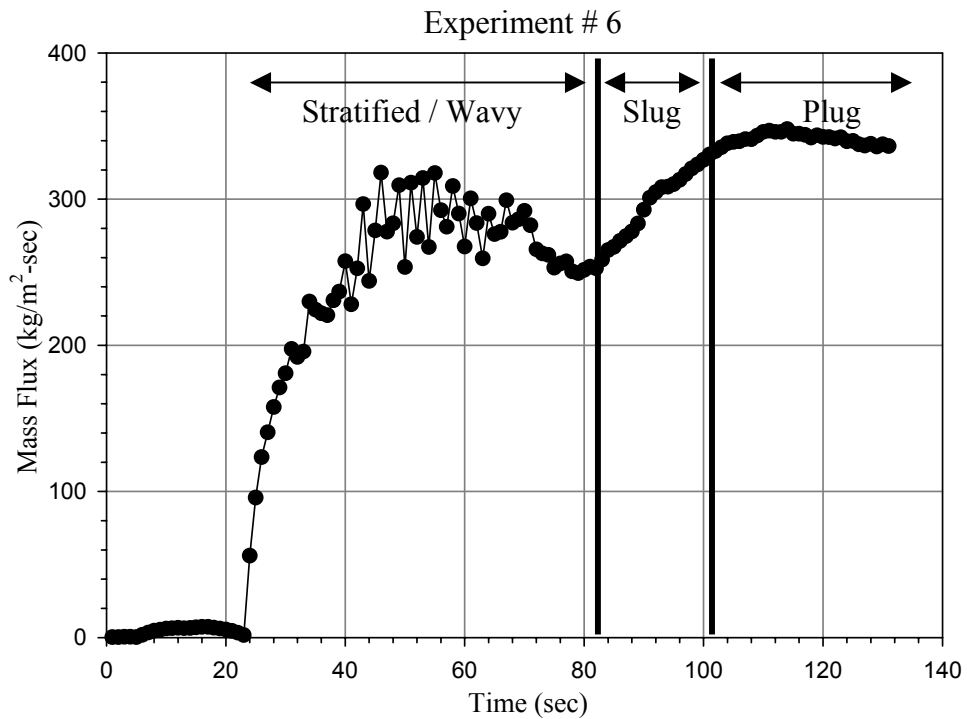


Figure 4-13. Mass flux history for experiment # 6.

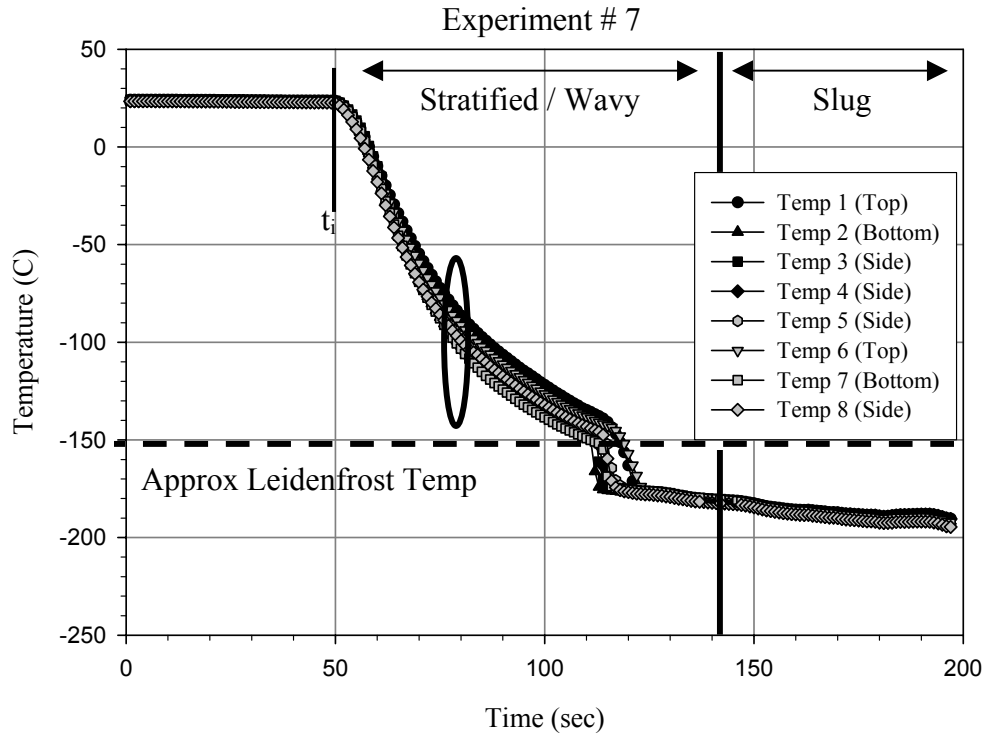


Figure 4-14. Temperature history during chilldown for experiment # 7.

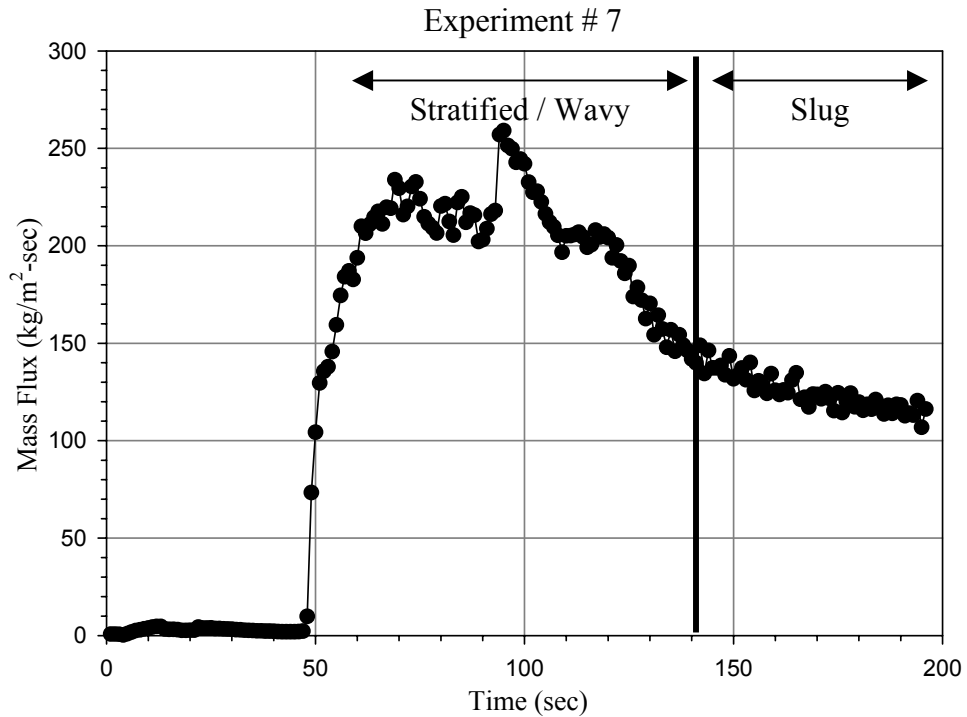


Figure 4-15. Mass flux history for experiment # 7.

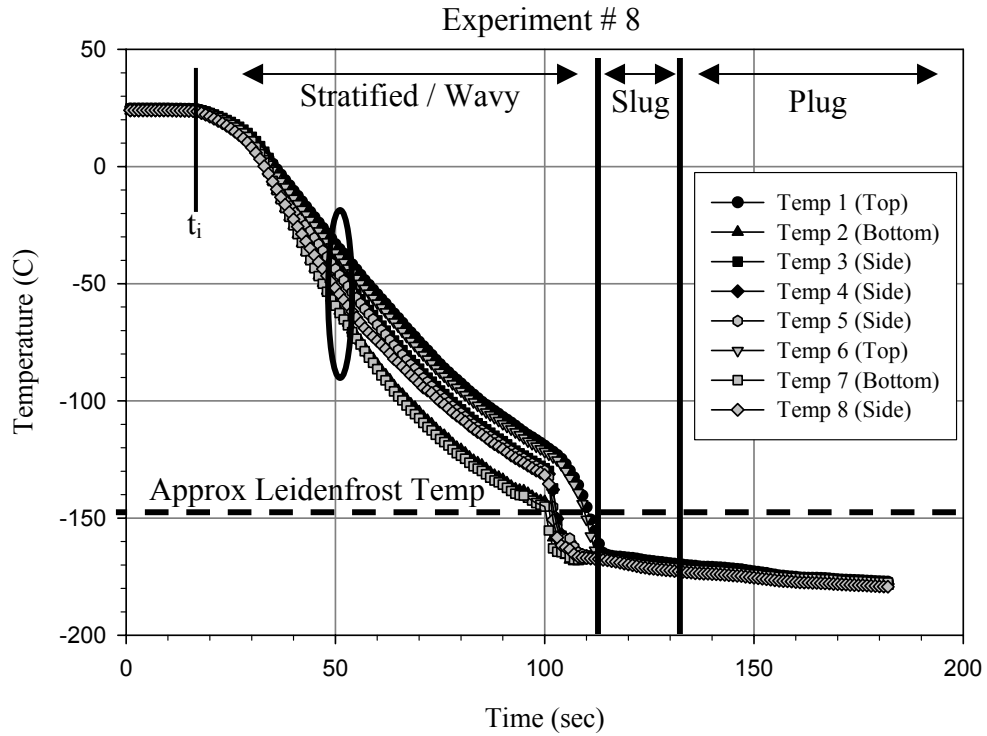


Figure 4-16. Temperature history during chilldown for experiment # 8.

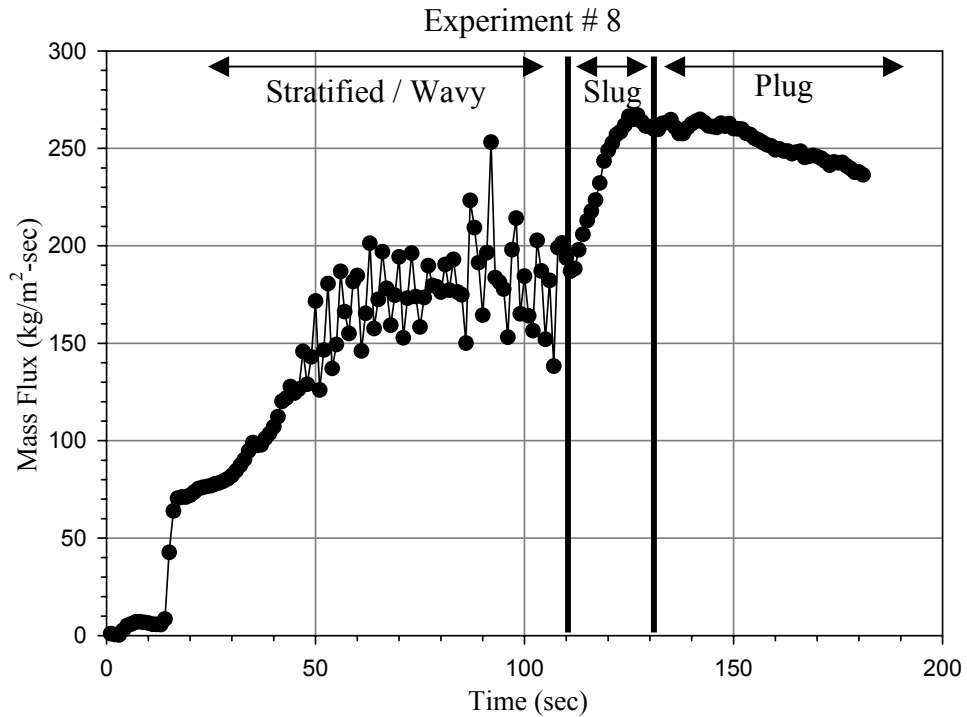


Figure 4-17. Mass flux history for experiment # 8.

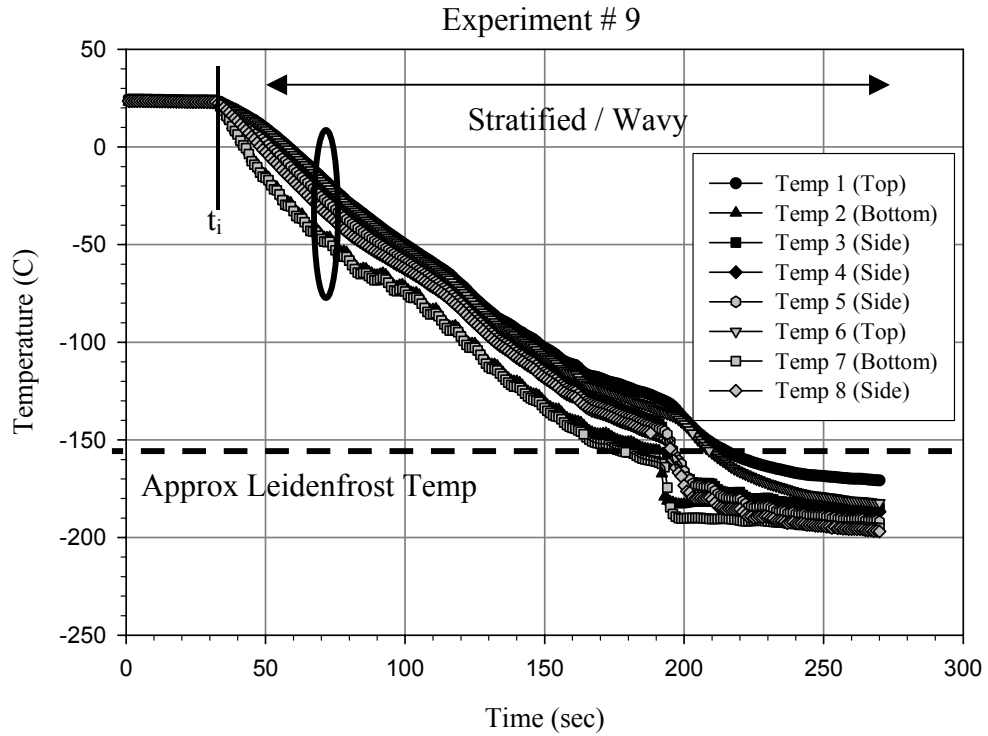


Figure 4-18. Temperature history during chilldown for experiment # 9.

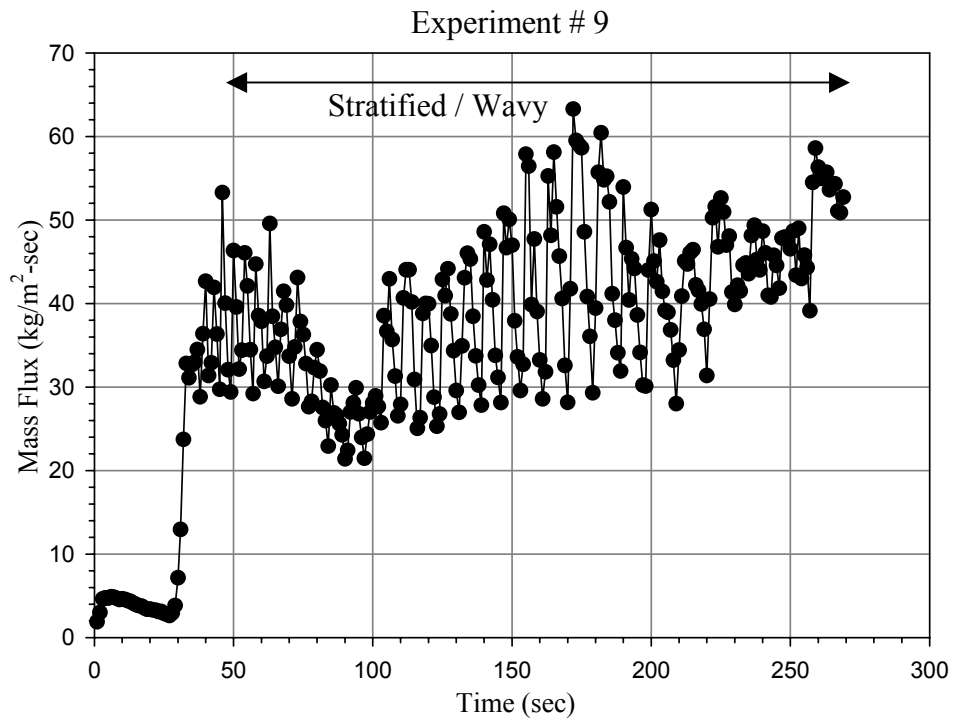


Figure 4-19. Mass flux history for experiment # 9.

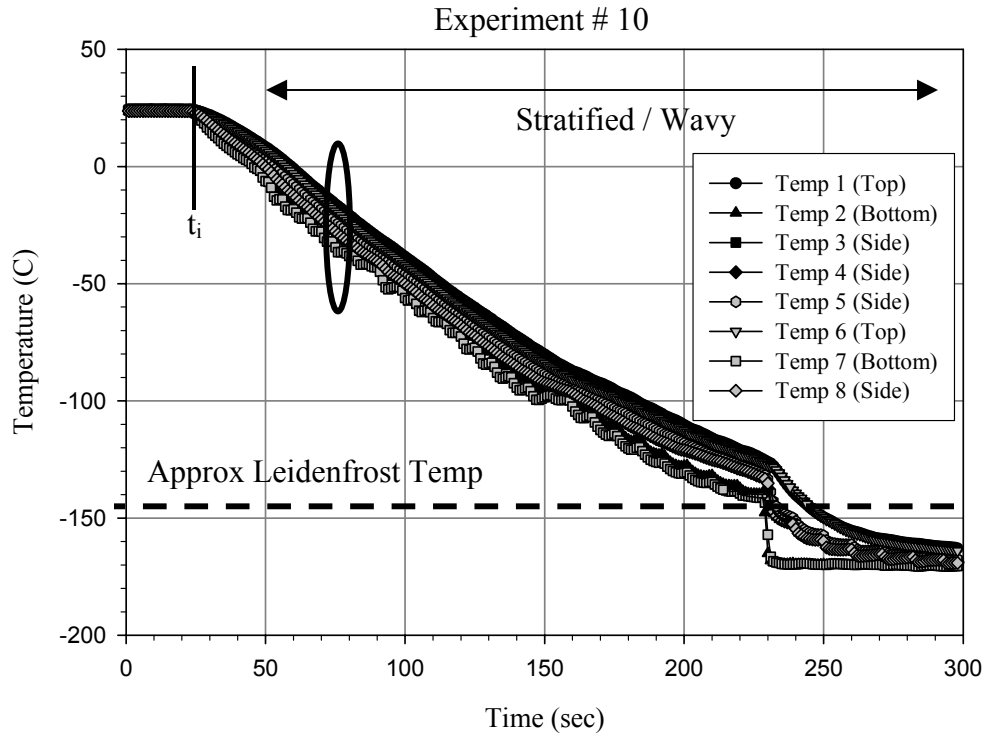


Figure 4-20. Temperature history during chilldown for experiment # 10.

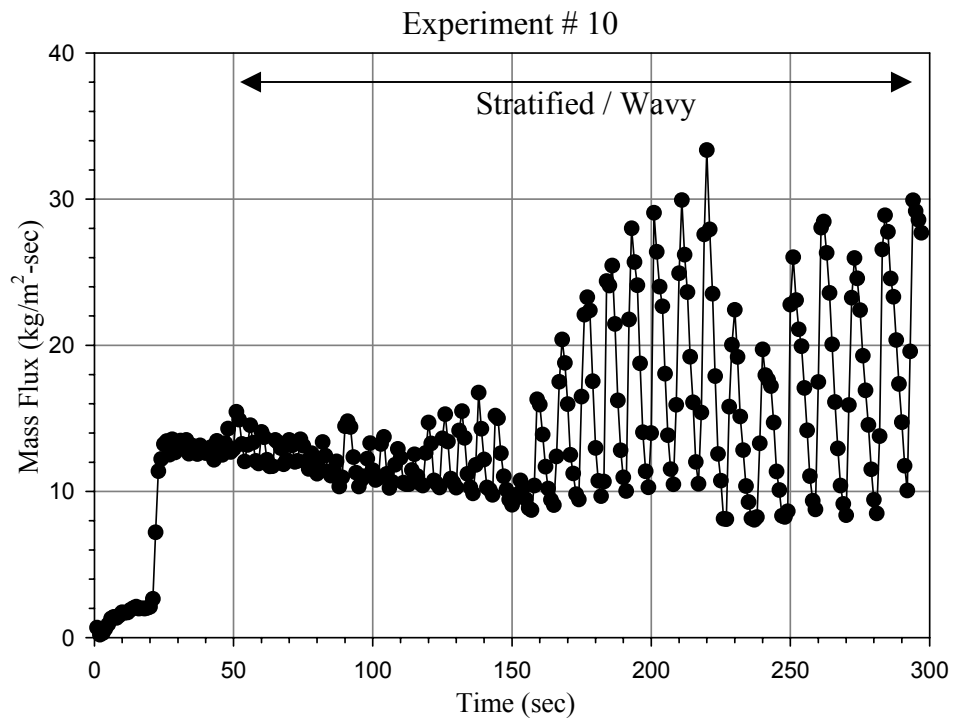


Figure 4-21. Mass flux history for experiment # 10.

4.3 Discussion

The outside wall temperature profiles have provided information pertaining to the chilldown behavior of the facility. The profiles provide specific information regarding the chilldown time, approximate Leidenfrost temperature, heat transfer transitions, and the circumferential temperature gradients in the transfer pipe.

The chilldown time for each of the experiments was determined from the temperature plots. Chilldown was defined to be complete when the wall temperature measurements leveled out at the approximate saturation temperature of the cryogenic nitrogen fluid. The chilldown time for each of the 10 experiments as well as the mass flux range is tabulated in Table 4-1. Results from the experiments support the intuitive relationship between an increased mass flux and lower chilldown time. Experiments 9 and 10, shown in Figures 4-18 through 4-21, clearly illustrate the effects of low mass flux. Figures 4-18 and 4-20 illustrate the more gradual and extended temperature history as well as the lack of flow structure transition beyond the stratified/wavy regime. The chilldown data from these 10 experiments will be used in future research to compute the transient heat transfer coefficient. In addition to the chilldown time, the temperature histories also provided information about the approximate Leidenfrost temperature.

The very high temperature difference, to the fluid from the pipe walls has been observed to cause film boiling of the liquid cryogen during the initial phases of chilldown. During film boiling, heat is transferred to the liquid by conduction through the vapor film and by radiation from the hot pipe wall. The film boiling flow structure prevails until the wall temperature of the transfer lines has chilled to the Leidenfrost temperature. Once the pipe has chilled below this temperature, a moving quenching front is observed briefly and is followed by nucleate flow boiling. This transition is identified

on the temperature profiles by a sharp decrease in temperature. This sharp drop in temperature is used to estimate the approximate Leidenfrost temperature. A diffusion time of approximately one second, corresponding to the thermal diffusion through the pipe wall, was computed for the steel transfer line at standard conditions. This time is relatively small and thus the thermocouple measurements should have good response to the heat transfer transients, and consequently the identification time for the Leidenfrost temperature should be reasonably accurate. The approximate Leidenfrost temperatures for the 10 experiments are tabulated in Table 4-1, and an average of the results indicate an average Leidenfrost temperature of approximately -148°C . It should be noted that a large discrepancy in time exists between the instant the quenching front was visually observed and the sharp decrease in the temperature identified in the plots. This discrepancy is largely attributed to the slow movement of the quenching front and the large separation of the thermocouples from the visual test section. For example, with a quenching front speed of 0.05 m/s , the delay time for the quenching front to pass from the visual section to the heat transfer section is on the order of 20 seconds.

In addition to the approximate Leidenfrost temperature the general shape of the temperature histories reveal three distinct heat transfer modes. In the beginning of the experiments the film-boiling heat transfer regime was evident as previously discussed. Following the film-boiling regime the nucleate flow-boiling regime is observed, and followed by evaporative convective heat transfer. In each of these regimes the dominant heat transfer mechanisms are varied. To develop precise predictive models these heat transfer transitions must be accounted for. It is interesting to note that during the majority of the chilldown, the heat transfer regime is film boiling. This is why the crude

chilldown models have been able to grossly predict the chilldown time. The results show that experiments conducted at high mass fluxes had faster transitions between each of these regimes, indicating that the chilldown process is strongly influenced by the convective fluid velocity. In addition to knowledge regarding the heat transfer regimes during chilldown, the temperature measurements also have provided quantitative knowledge of the temperature gradients in the transfer line during chilldown.

Bronson et al [2] previously reported moderate circumferential temperature gradients. Their work recognized the presence of large gradients within horizontal transfer lines due to the stratification of the cryogenic fluid. The results of the 10 experiments confirm not only the presence of large circumferential temperature gradients but also the existence of small axial temperature gradients during the quenching front phase. The magnitudes of the circumferential temperature gradients are primarily influenced by surface wetting, and thus highly influenced by the flow structure. The largest temperature gradients were observed in experiments that had both a stratified/wavy flow structure and low liquid level height. In these experiments the low liquid height was not sufficient to wet the surface in the vicinity of side-placed thermocouples and thus the heat transfer at these regions was smaller than at bottom of the transfer line. This corresponds to a more distinguished circumferential gradient. Noticeable examples of significant circumferential temperature gradients were evidenced in experiments 1, 2, 3, 4, and 8, shown in Figures 4-2, 4-4, 4-6, 4-8, and 4-16. The general observations regarding the influence of the flow structure as well as the measured results pertaining to the temperature gradients will be incorporated into the future development of numerical heat transfer models for cryogenic transfer systems.

Overall the general shape of the chilldown profiles for each of the tests are in good agreement with the experimental results previously reported by Bronson et al [2], Steward et al [5], and Chi [9]. The temperature profiles have revealed a strong association between higher mass flux and lower chilldown time, identified an approximate Leidenfrost temperature of -148°C , identified three distinct heat transfer regime transitions, and confirmed the existence of large circumferential temperature gradients as well as small axial gradients during the transition from film boiling to nucleate flow boiling. This data will be useful in developing and confirming future numerical chilldown models.

4.4 Sources of Error

As evidenced in all of the transient temperature profiles, the visual observations of the film-boiling fronts did not coincide with the transition to nucleate boiling displayed in the temperature profiles. The disparity in time between the visually observed boiling front passage and the Leidenfrost point suggested by the temperature profiles occurs due to the separation of the thermocouples from the visual test section. This suggests that there is a possibility that the flow structure transitions occurring in the steel transfer line may vary from what is visually observed in the glass viewing section. Future investigation is required to evaluate the significance of the error.

CHAPTER 5 CONCLUSIONS AND RECOMMENDATIONS

In this work, an experimental investigation was conducted to gather detailed information regarding the flow structure, flow properties, and heat transfer mechanisms associated with cryogenic chilldown. An experimental facility was constructed and used to gather visual images of the flow structure and heat transfer mechanisms as well as temperature and pressure data. This chapter lists the significant accomplishments and findings of this experimental investigation and concludes with suggestions for future research.

5.1 Accomplishments and Findings

The research presented in this document has enhanced the fundamental understanding of cryogenic chilldown as follows:

- 1. Visualizations of the entire chilldown process were obtained throughout a range of mass fluxes. The visualization revealed the detailed flow structure and heat transfer transitions that occur during chilldown. Images captured the transition from film boiling to nucleate boiling, revealing the quenching front shape, height, and approximate transverse speed. The detailed knowledge gained of the flow structure and heat transfer transitions will be incorporated in the future development of an advanced fundamental numerical chilldown model.
- 2. Wall temperature profiles and chilldown time data were also obtained. The wall temperature profiles helped verify the existence and magnitude of circumferential and small axial temperature gradients in the transfer line during the various phases of chilldown, as well as determine the approximate Leidenfrost temperature of the nitrogen. This information will be useful in analyzing current and developing future numerical chilldown models capable of predicting the chilldown time and temperature gradients of transfer systems.

5.2 Recommendations for Future Research

The current research was conducted to gather a detailed understanding of the mechanisms of cryogenic chilldown with the ultimate goal of developing an advanced mechanistic based chilldown model. Several important issues remain unresolved and are suggested for future research:

- 1. During the experiments annular flow was observed at sufficiently high mass flux rates (typically greater than $600 \text{ kg/m}^2\text{-sec}$); however due to current limitations of the camera system and visual test section, a distinguishable liquid/vapor interface at the upper portion of the test section could not be easily identified. Capturing the liquid-vapor interface in annular flow was particularly difficult because of the rapid flow rate and the distributed flow around the inner wall of the tube. The distributed flow added additional distortion and concealed the internal liquid-vapor interface. To capture these images the camera system needs to be enhanced by changing the lighting setup, lens configuration, and shutter time. Consideration of annular flow is critical to developing a comprehensive understanding of chilldown and this issue should be initially pursued in future research.
- 2. Due to an oversight in the data acquisition setup, the measured pressure drop across the test section was not accurate. The oversight has been corrected, however future experiments must now be run to compile a database for a range of flow conditions. The data should then be compared to existing pressure drop models and if necessary a new model should be derived.
- 3. The flow structure has a large impact on the thermal behavior of the system during chilldown and is of considerable importance. To consider the flow structure in a numerical model for chilldown, a method for predicting flow structure transition is required. Future research should address the development of a flow regime map and a method for predicting flow regime transitions. The current data should be initially compared with the flow regime maps of Steiner [25], Kattan-Thome-Favrat [26,27,28], Baker [3], and Taitel and Dukler [29].
- 4. Additional research also needs to be conducted to identify the heat transfer coefficient for the transfer line and develop a method of computing the inside wall temperature. An inverse heat transfer approach should be useful for this purpose.

APPENDIX A
PROPERTIES OF NITROGEN

The relations presented in this appendix were used to calculate the relevant physical and thermodynamic properties of both liquid and gaseous nitrogen. All of the properties except vapor density were generated from the NIST fluid thermophysical properties database [30]. The saturation properties are valid for $-210 < T < -147$ °C. All temperature and pressure values are reported in °C and kPa respectively.

A.1 Property Relations

1. Saturation Temperature, $T_{sat}(P)$:

$$T_{sat}(\text{°C}) = 1 * 10^{-05} * P^3 + 0.0082 * P^2 + 1.7091 * P + 119.51 \quad (\text{A.1})$$

2. Saturation Pressure, $P_{sat}(T)$:

$$P_{sat}(\text{kPa}) = 1 * 10^{-05} * T^3 + 0.0075 * T^2 + 1.5793 * T + 111.44 \quad (\text{A.2})$$

3. Density, liquid, ρ_l :

$$\rho_l(\text{kg/m}^3) = -0.0787 * T^2 - 33.907 * T - 2820.6 \quad (\text{A.3})$$

4. Density, vapor, ρ_g :

$$\rho_g(\text{kg/m}^3) = (P_{\text{exit}} + 101) / (.2968 * (T_{\text{exit}} + 273)) \quad (\text{A.4})$$

5. Liquid Dynamic Viscosity, μ_l :

$$\mu_l(\text{Pa*s}) = (-4 * 10^{-09}) * T^3 - (2 * 10^{-06}) * T^2 - 0.0004 * T - 0.0233 \quad (\text{A.5})$$

6. Vapor Dynamic Viscosity, μ_g :

$$\mu_g(\text{Pa*s}) = (5 * 10^{-08}) * T + 2 * 10^{-05} \quad (\text{A.6})$$

APPENDIX B
EXPERIMENTAL CRYOGENIC CHILLDOWN VISUALIZATIONS

A digital copy of all of the images and experimental data may be attained by request

from:

Dr. James F. Klausner

237 Mechanical and Aerospace Engineering Building B

PO Box 116300

Gainesville, Fl 32611-6300

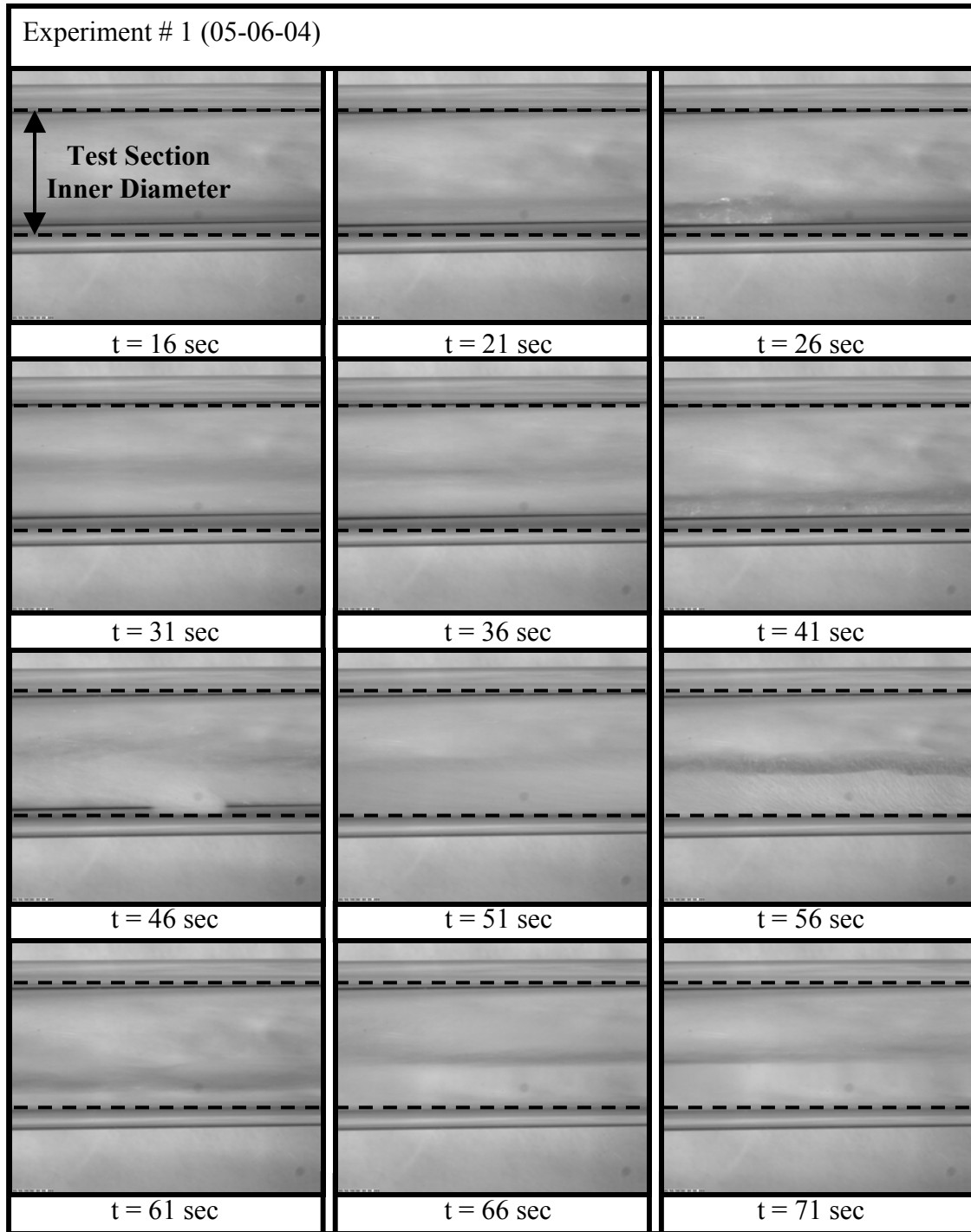


Figure B-1. Chardown images from experiment # 1.

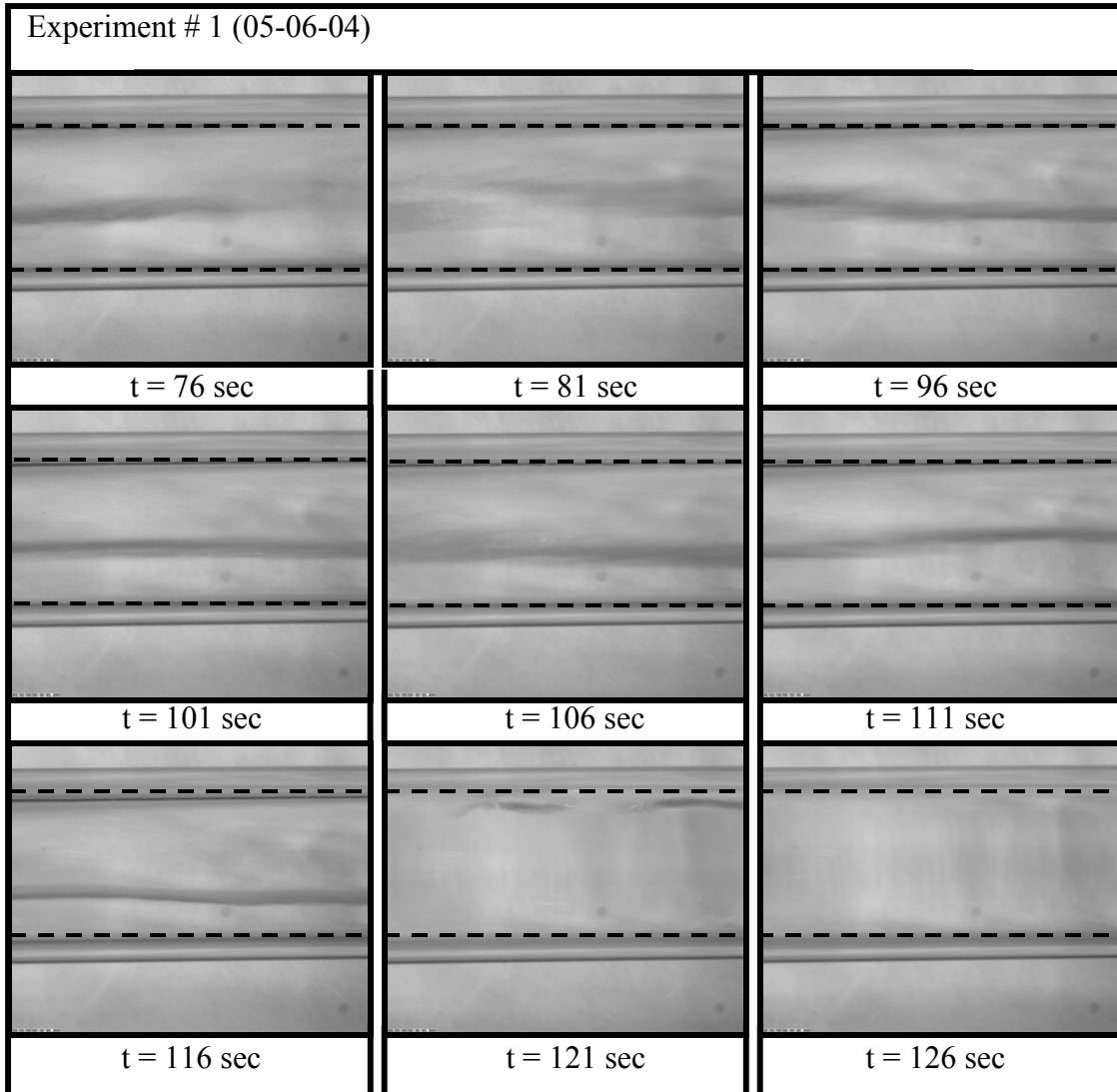


Figure B-1. Continued.



Figure B-2. Chardown images from experiment # 2.

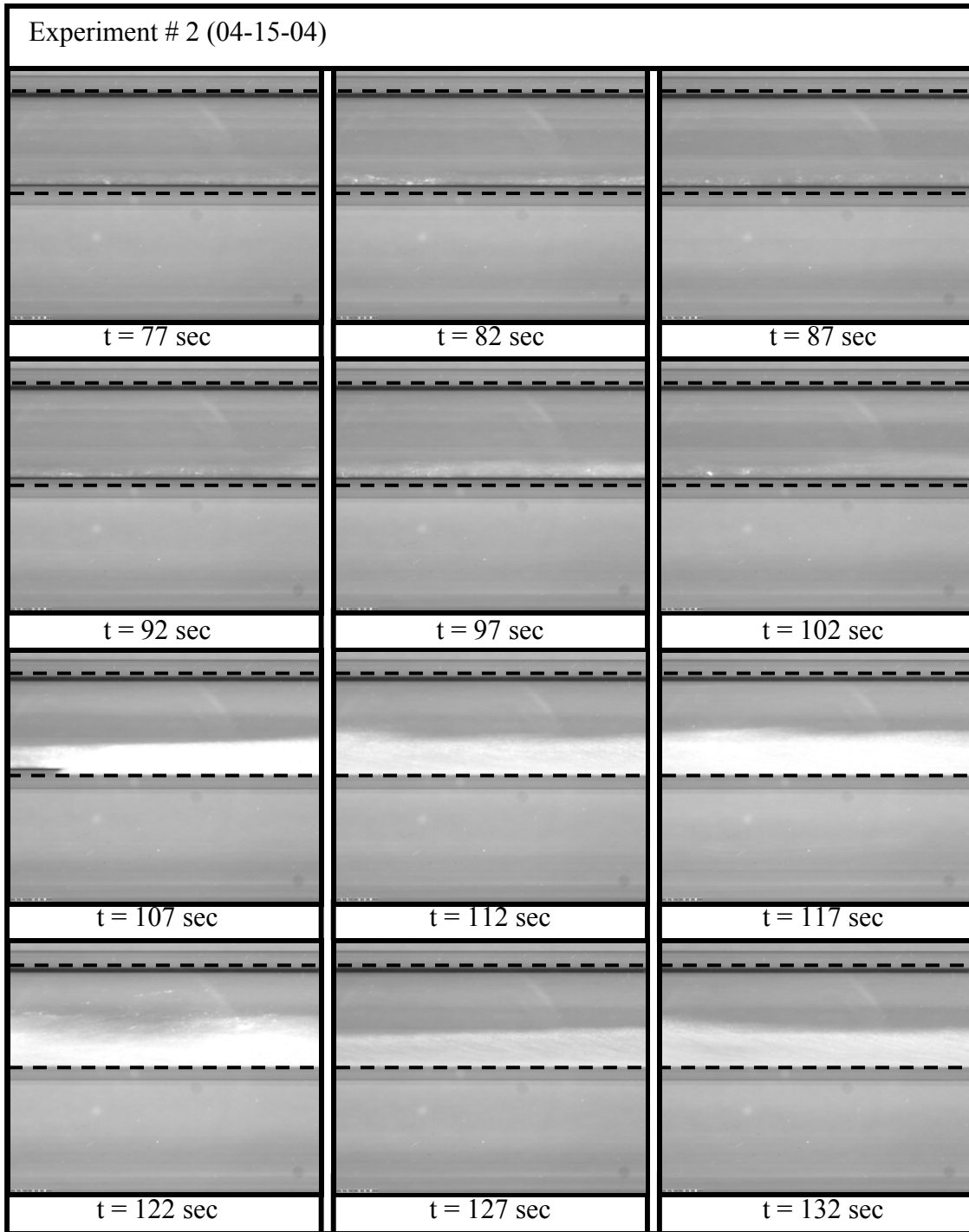


Figure B-2. Continued.

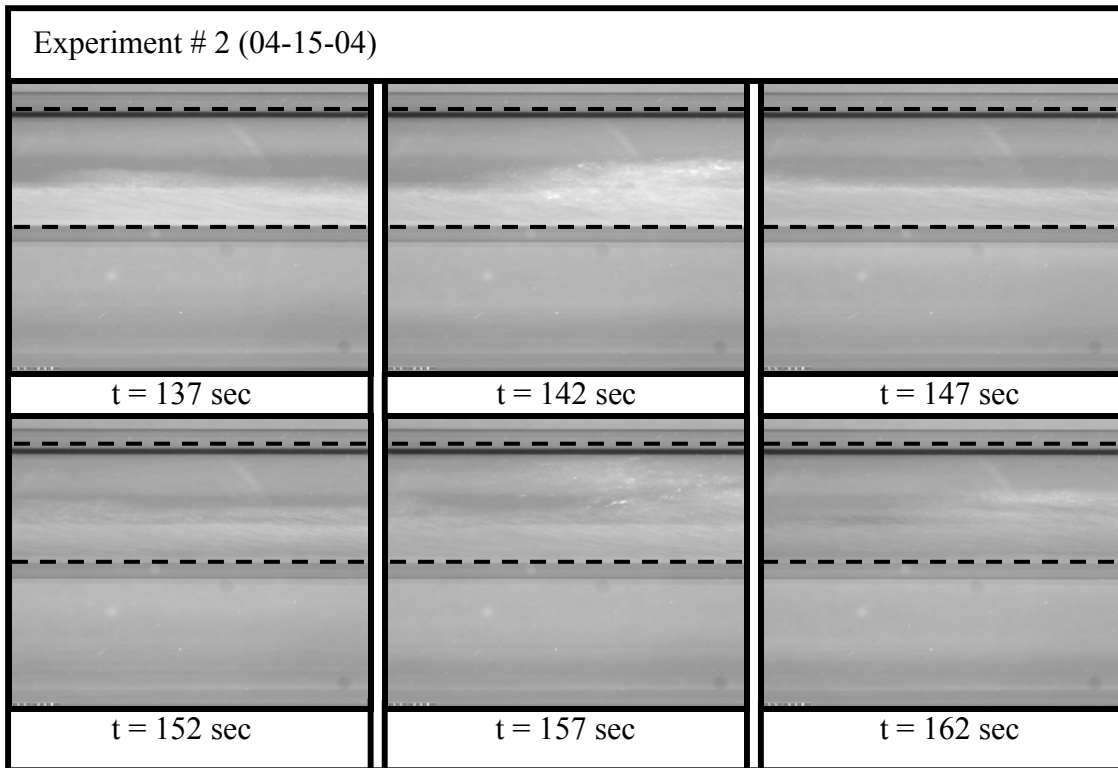


Figure B-2. Continued.

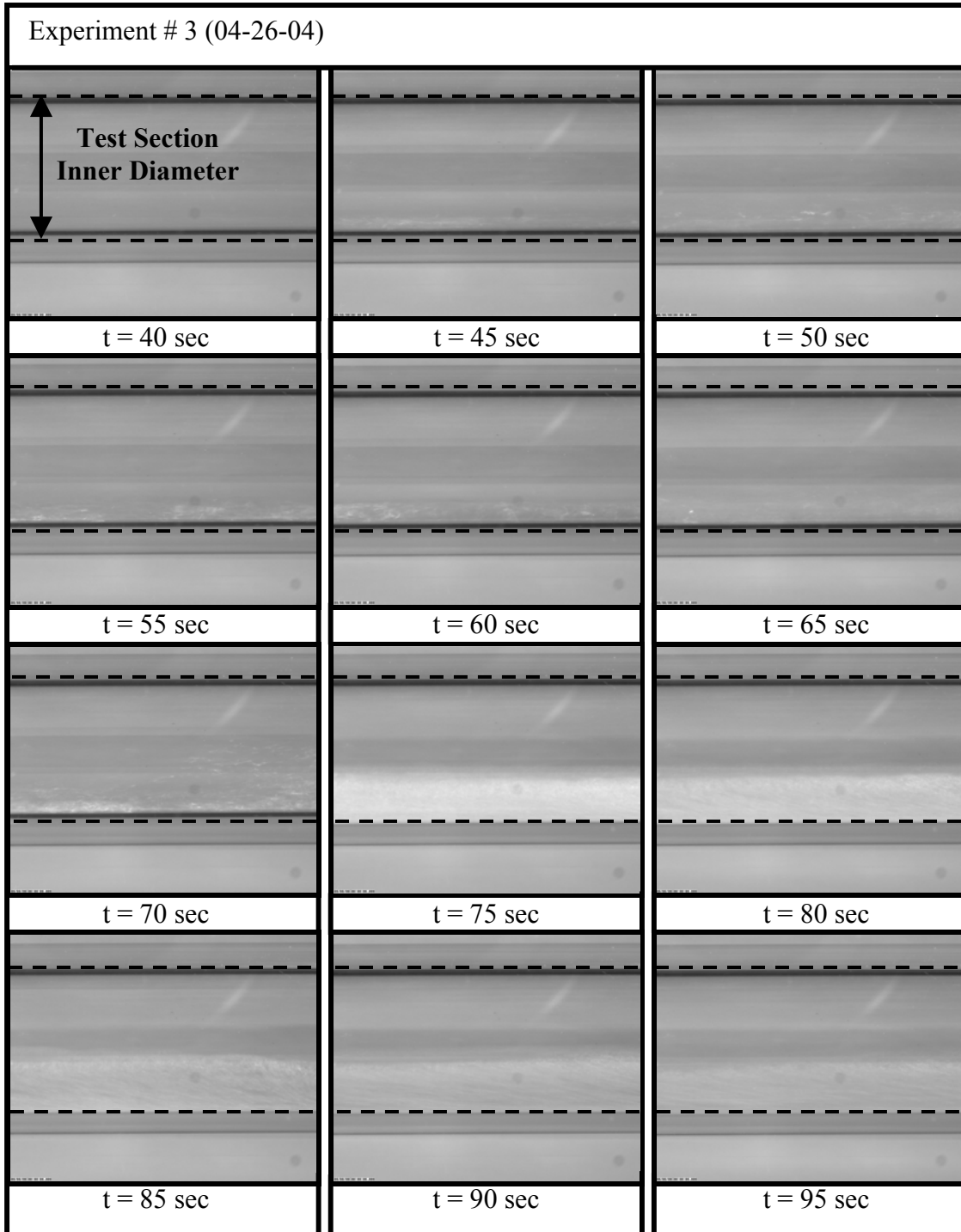


Figure B-3. Chardown images from experiment # 3.

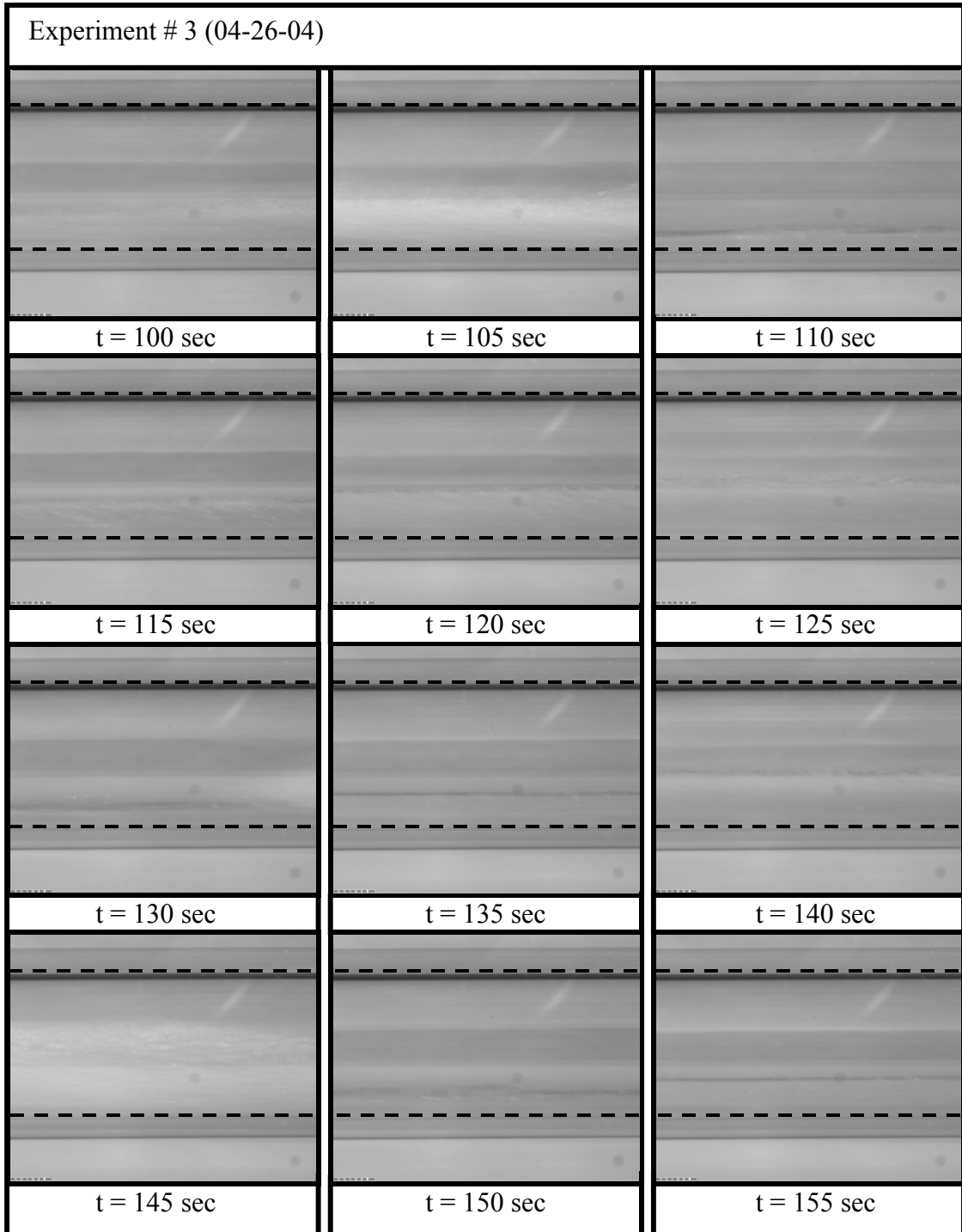


Figure B-3. Continued.

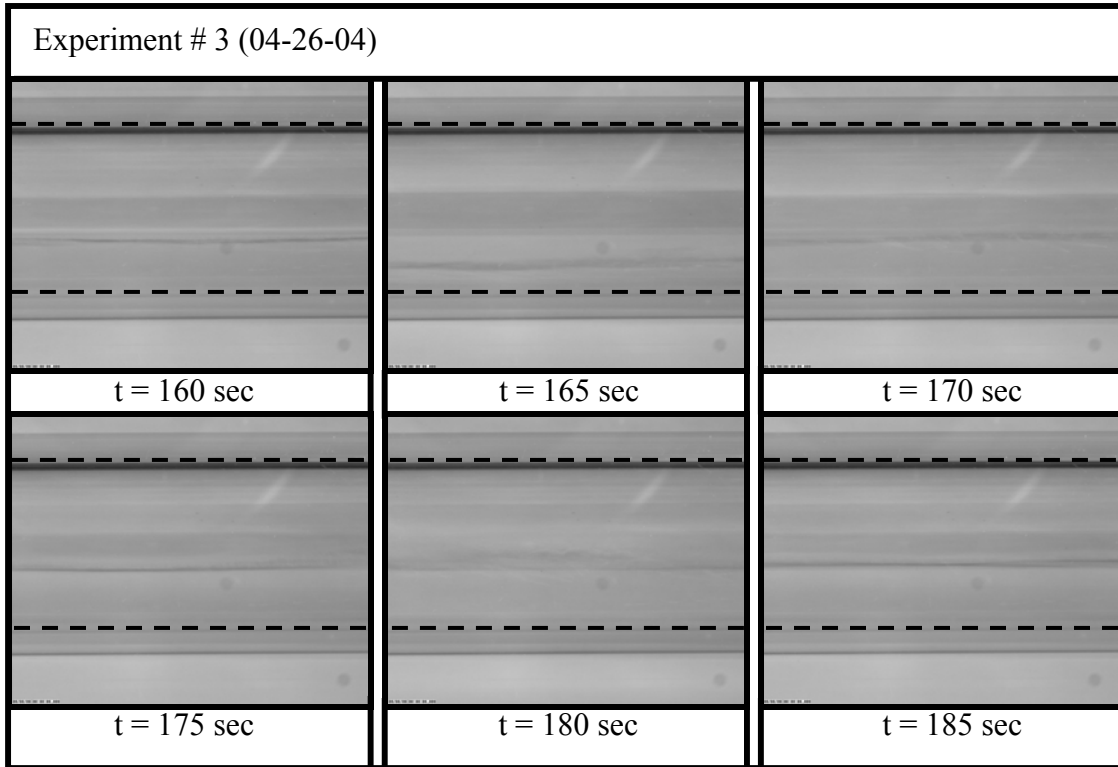


Figure B-3. Continued.

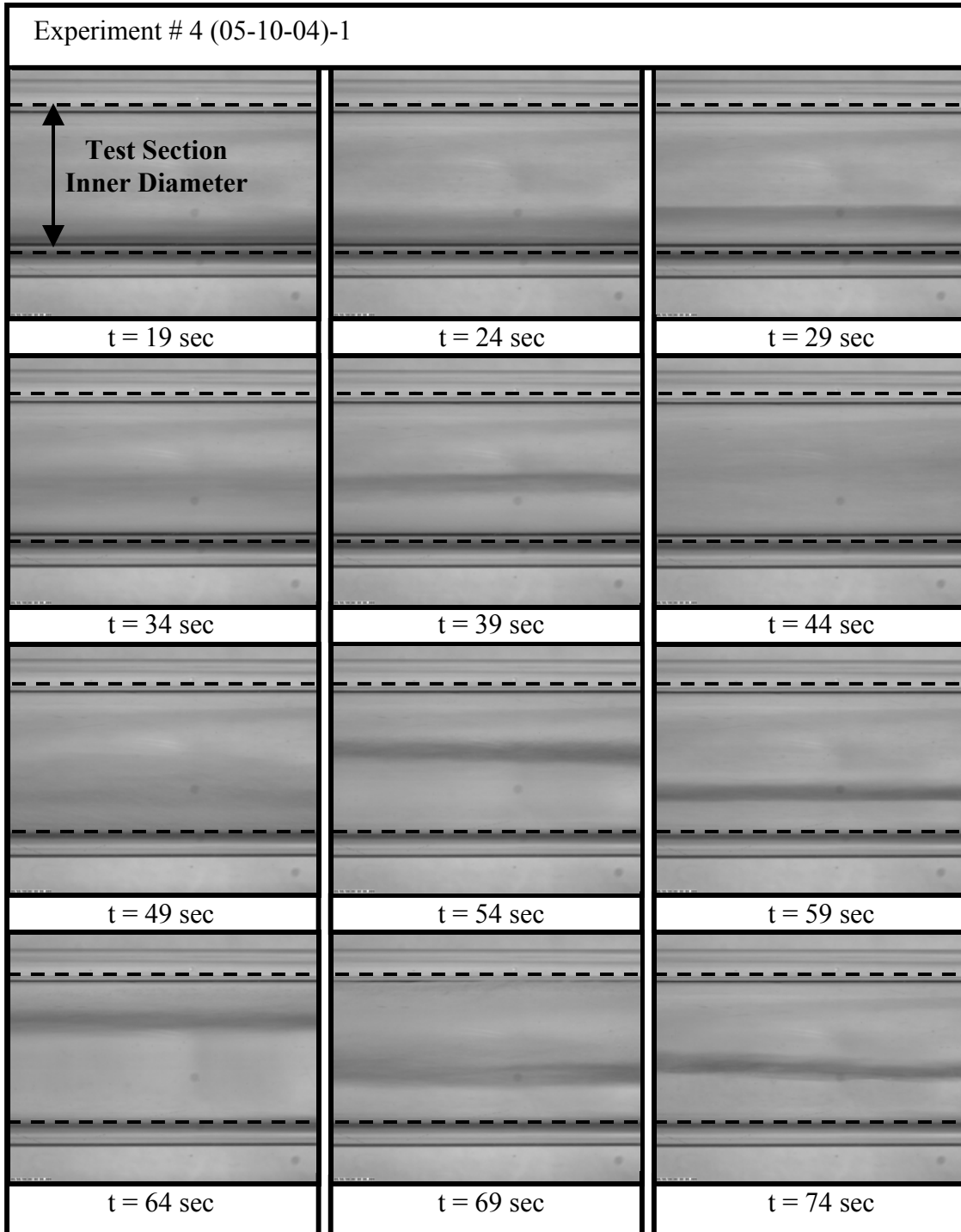


Figure B-4. Chardown images from experiment # 4.

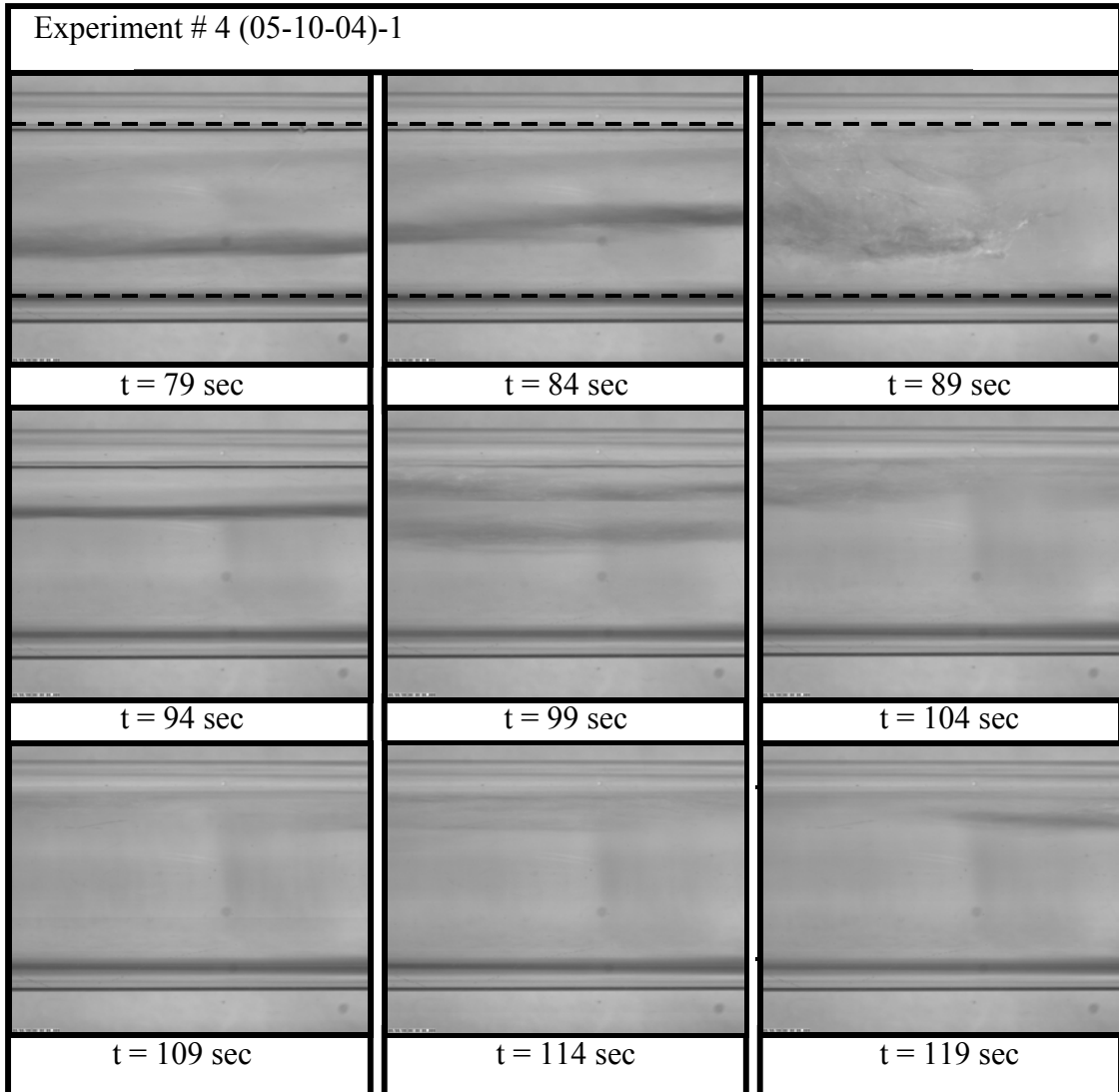


Figure B-4. Continued.

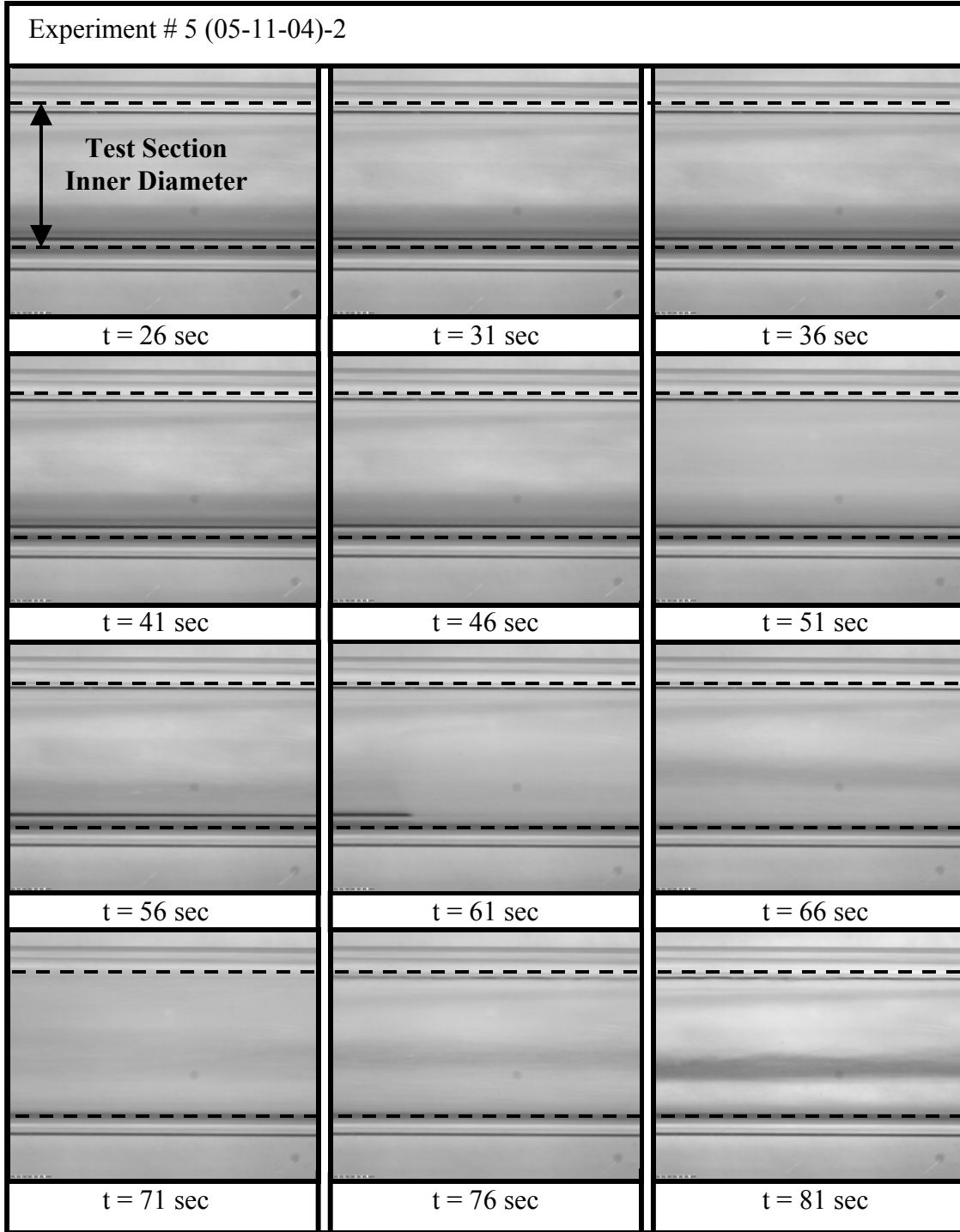


Figure B-5. Chardown images from experiment # 5.

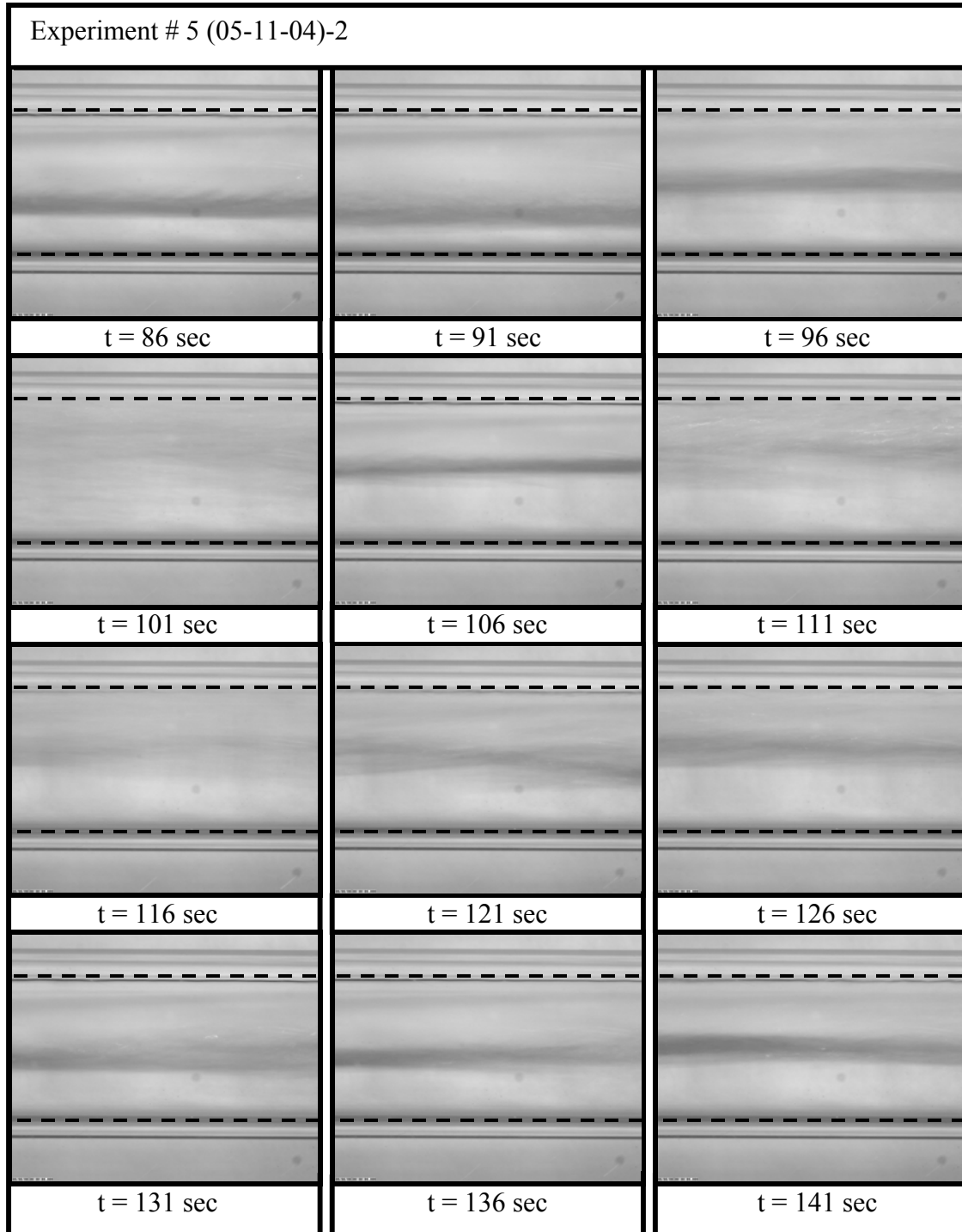


Figure B-5. Continued.

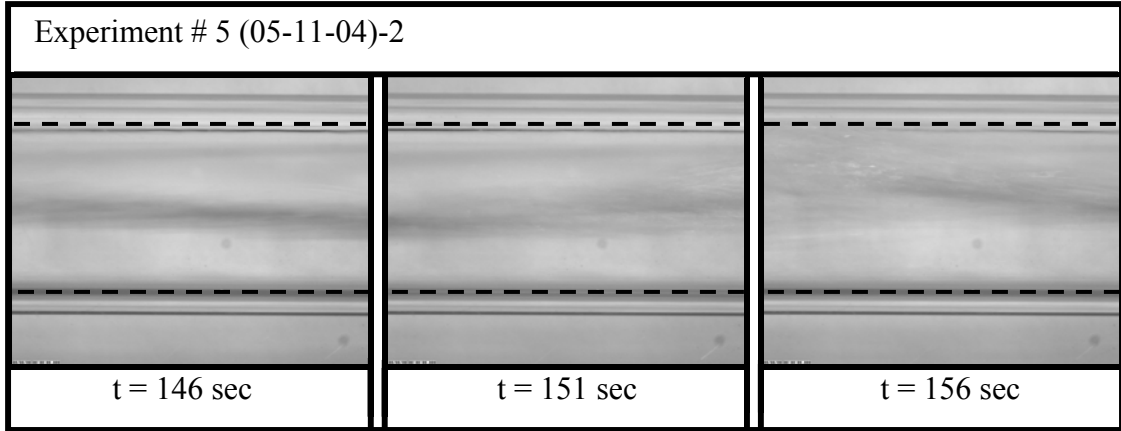


Figure B-5. Continued.

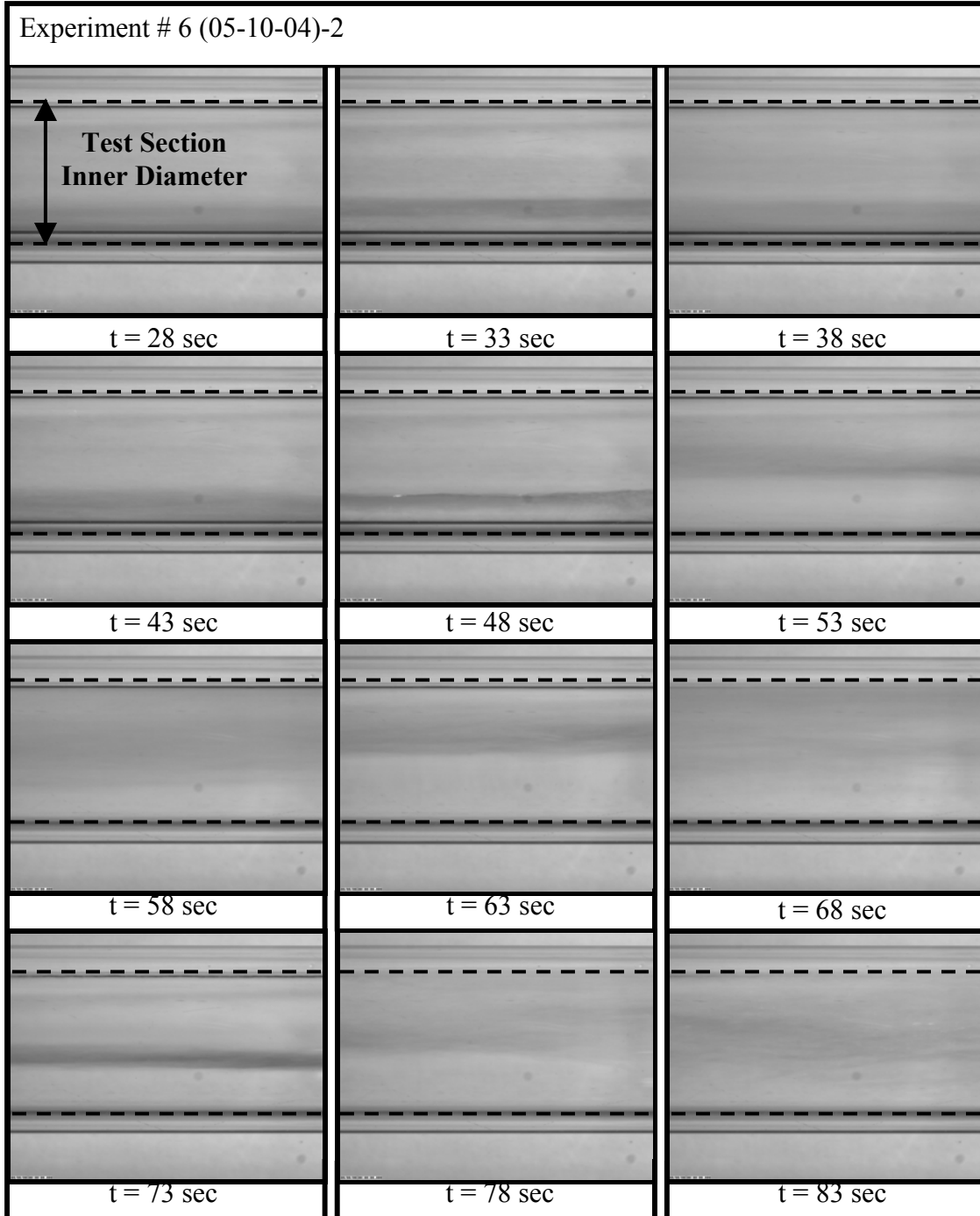


Figure B-6. Chilldown images from experiment # 6.

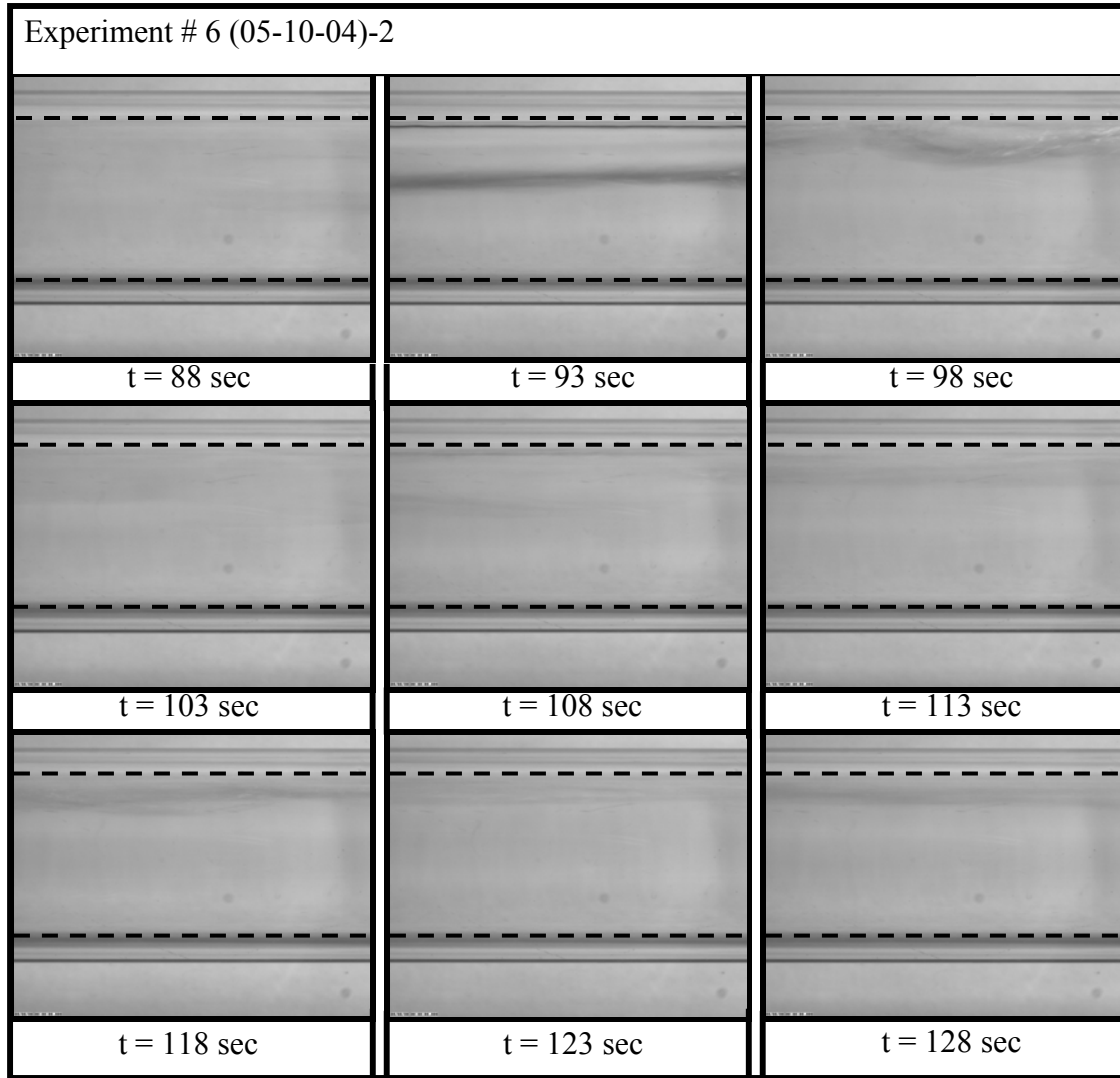


Figure B-6. Continued.



Figure B-7. Chilldown images from experiment # 7.

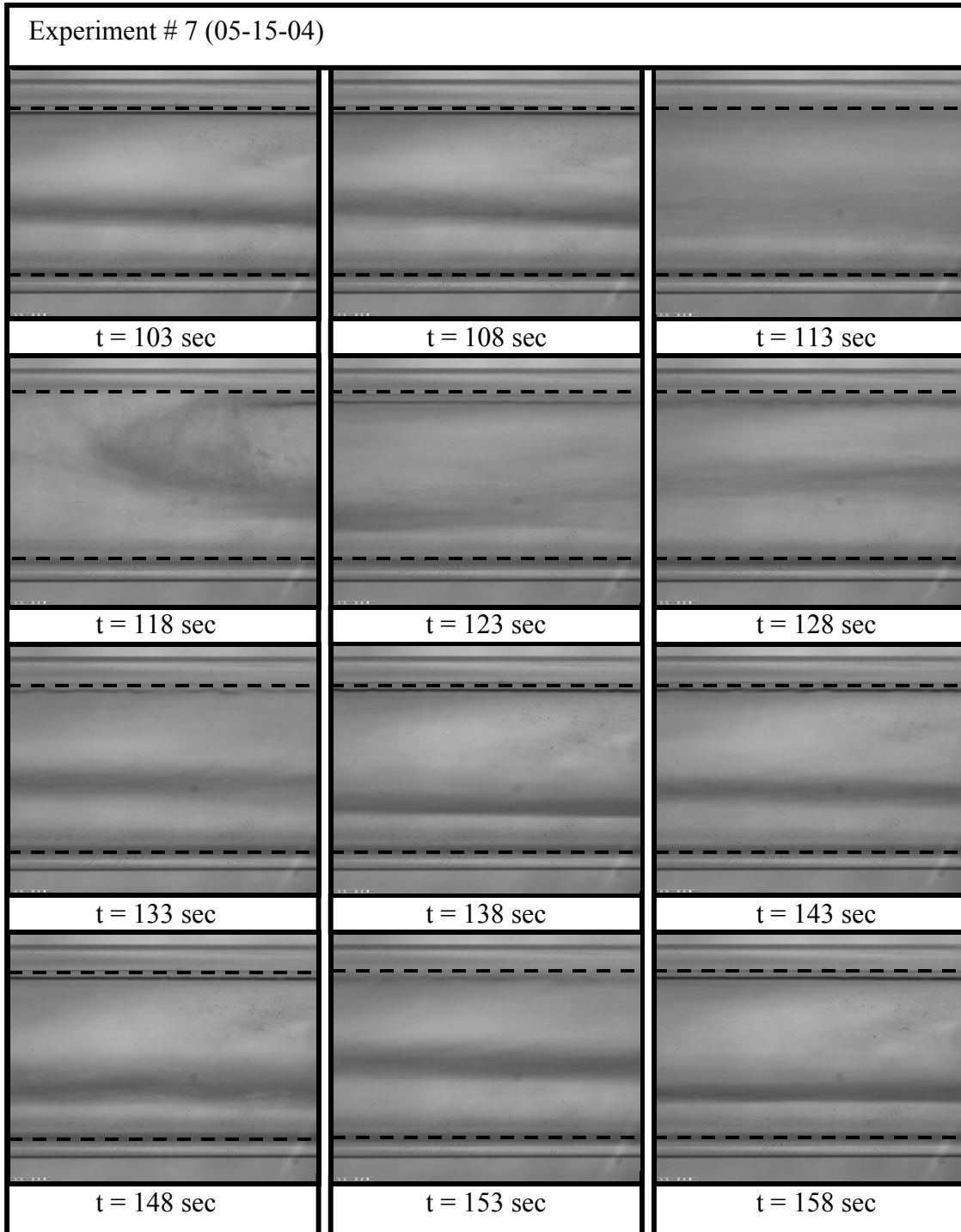


Figure B-7. Continued.

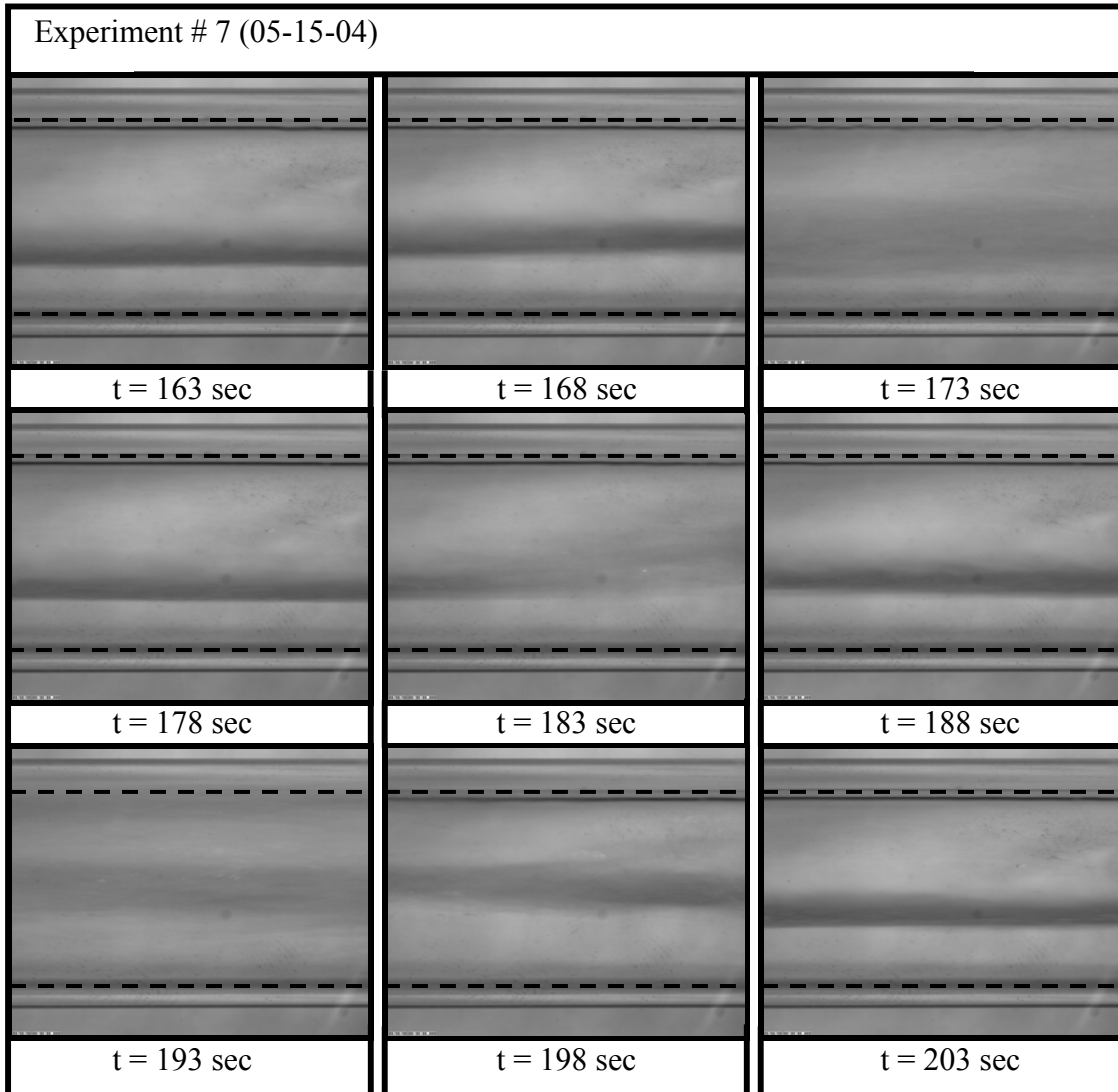


Figure B-7. Continued.

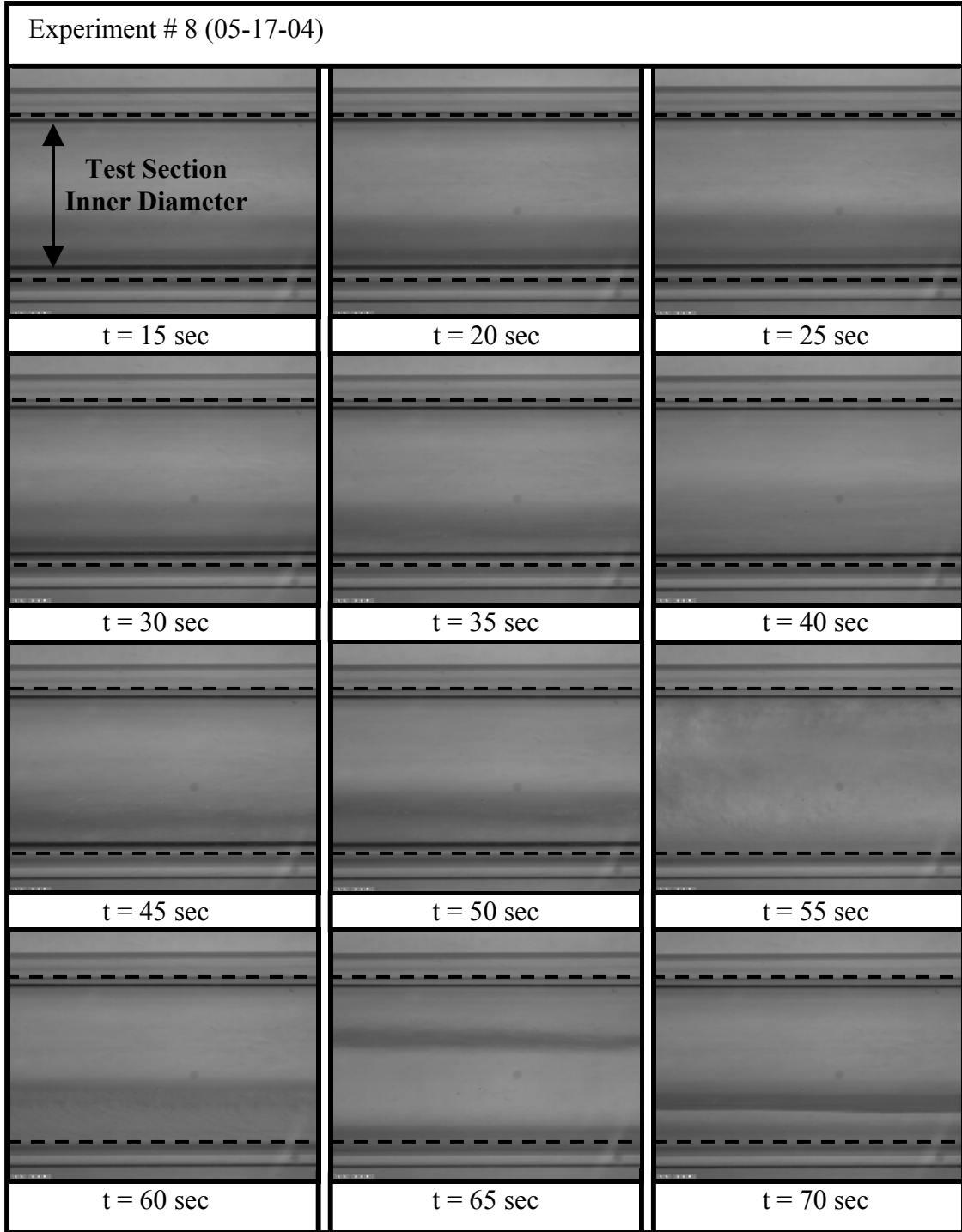


Figure B-8. Chardown images from experiment # 8.

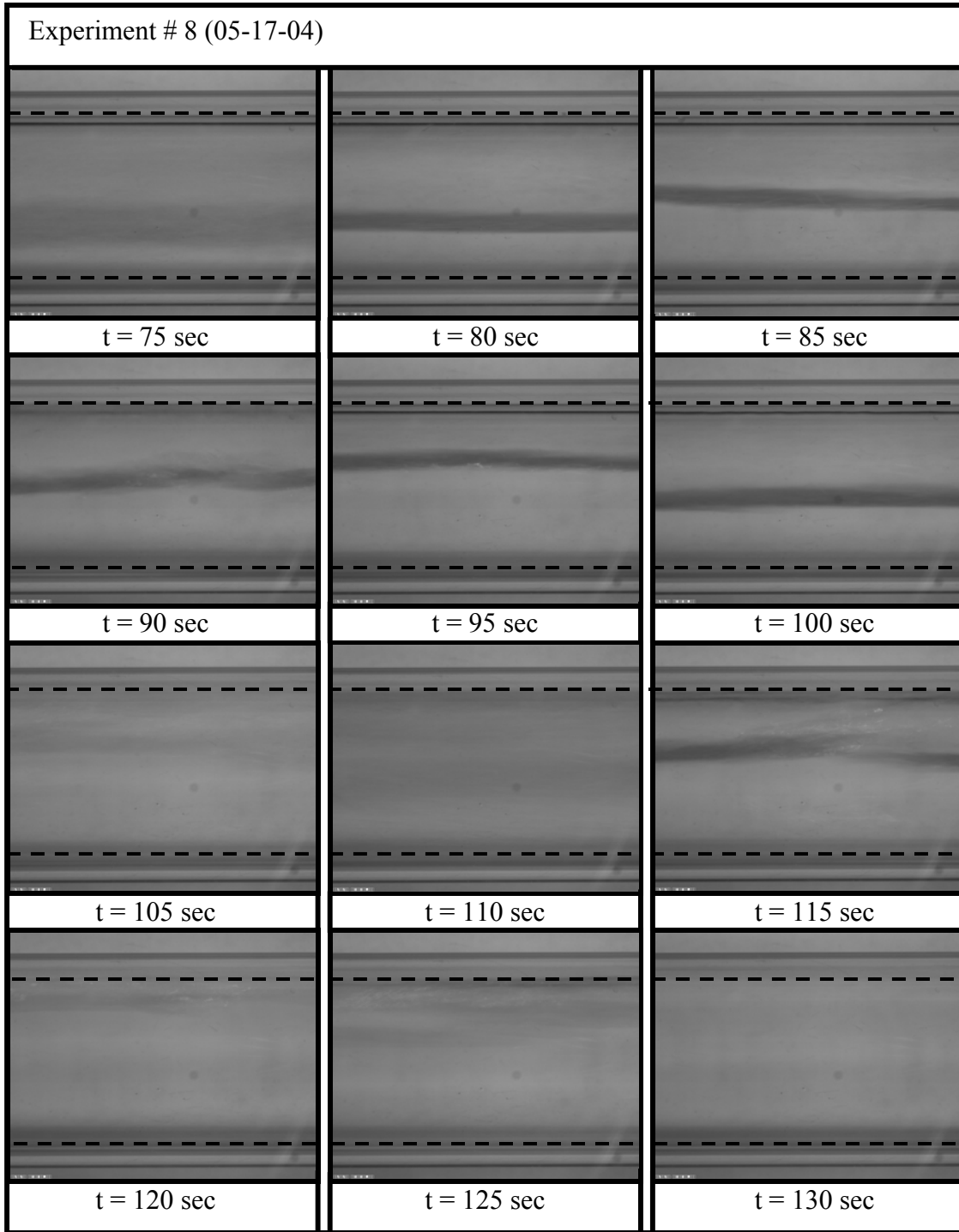


Figure B-8. Continued.

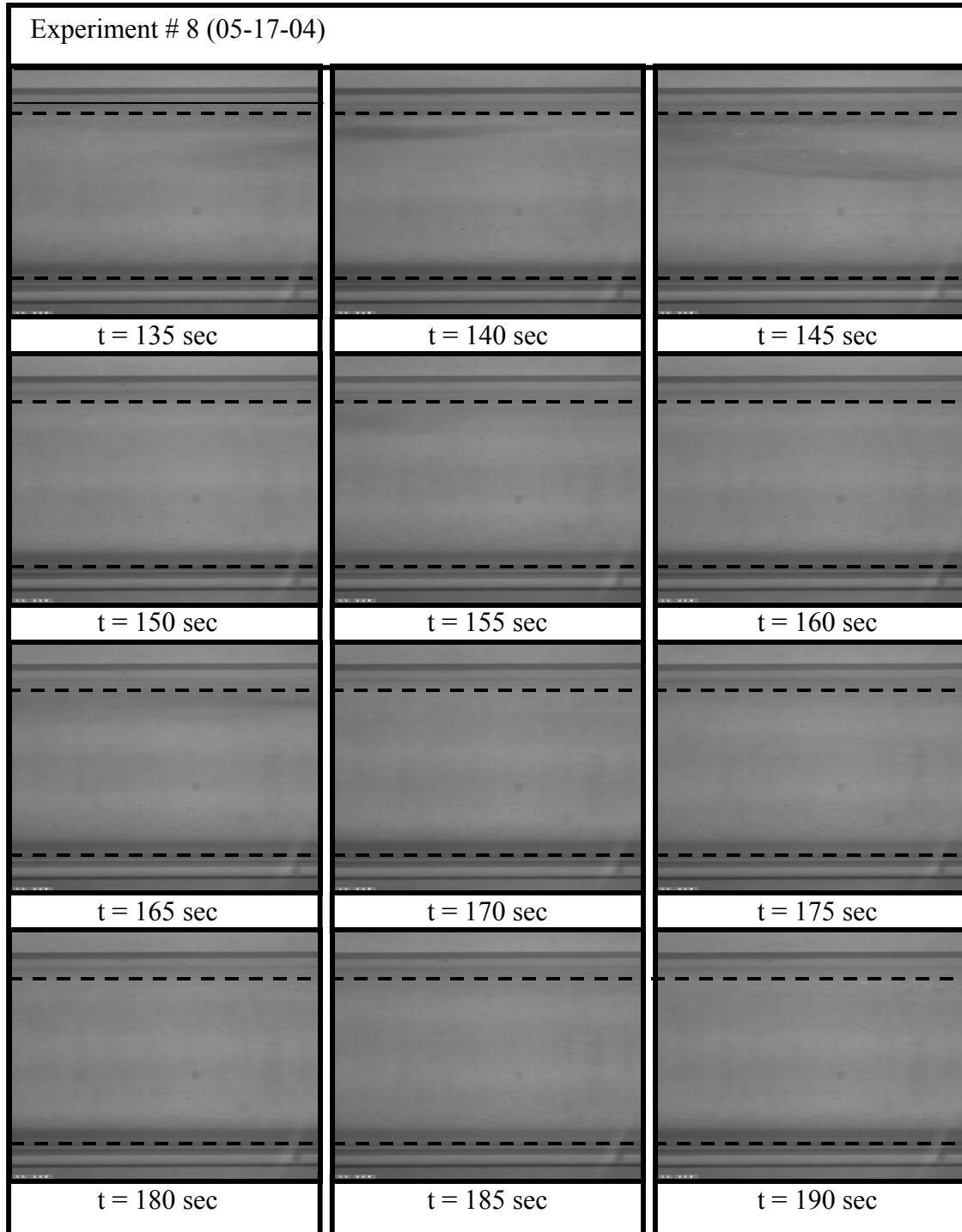


Figure B-8. Continued.

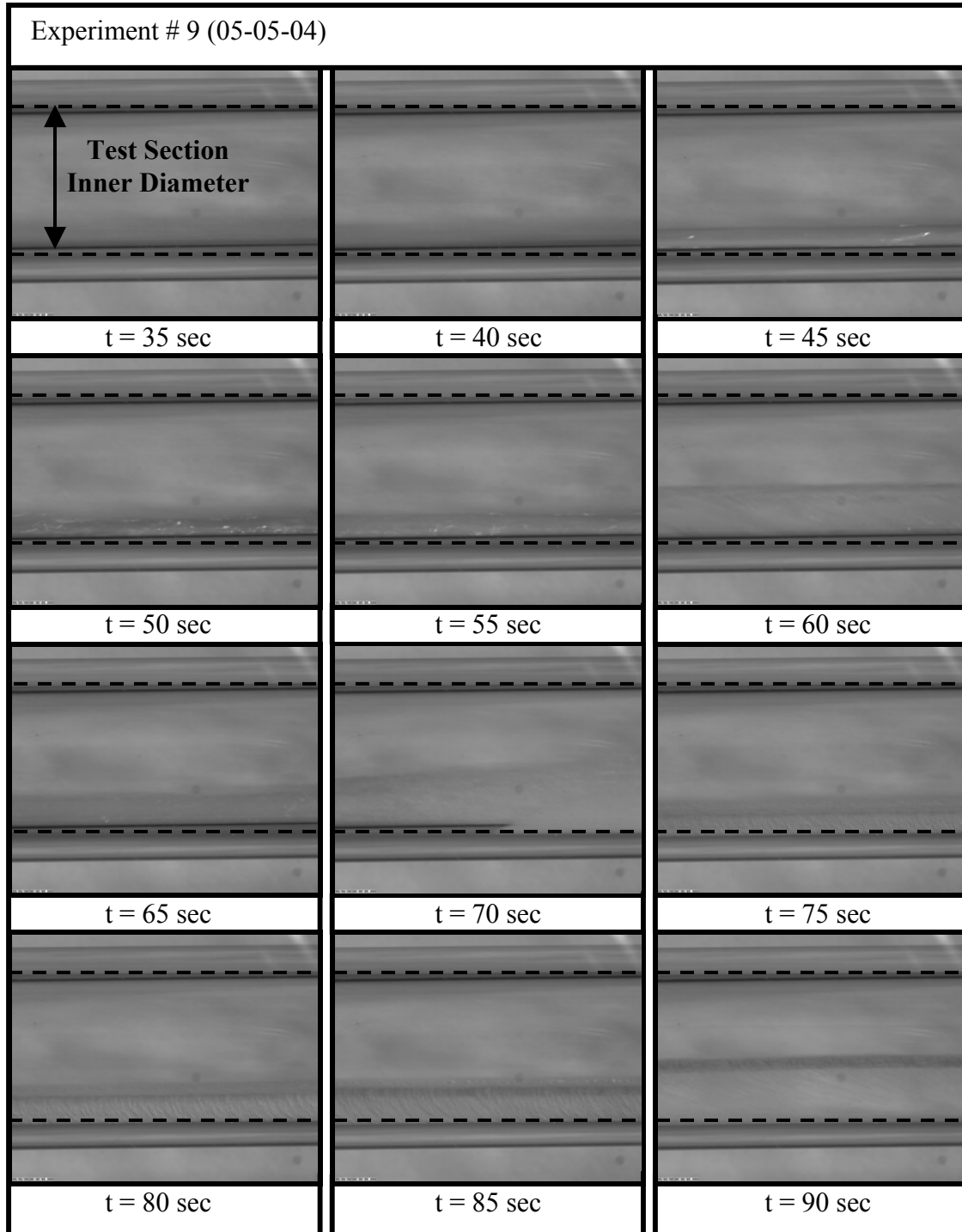


Figure B-9. Chardown images from experiment # 9.

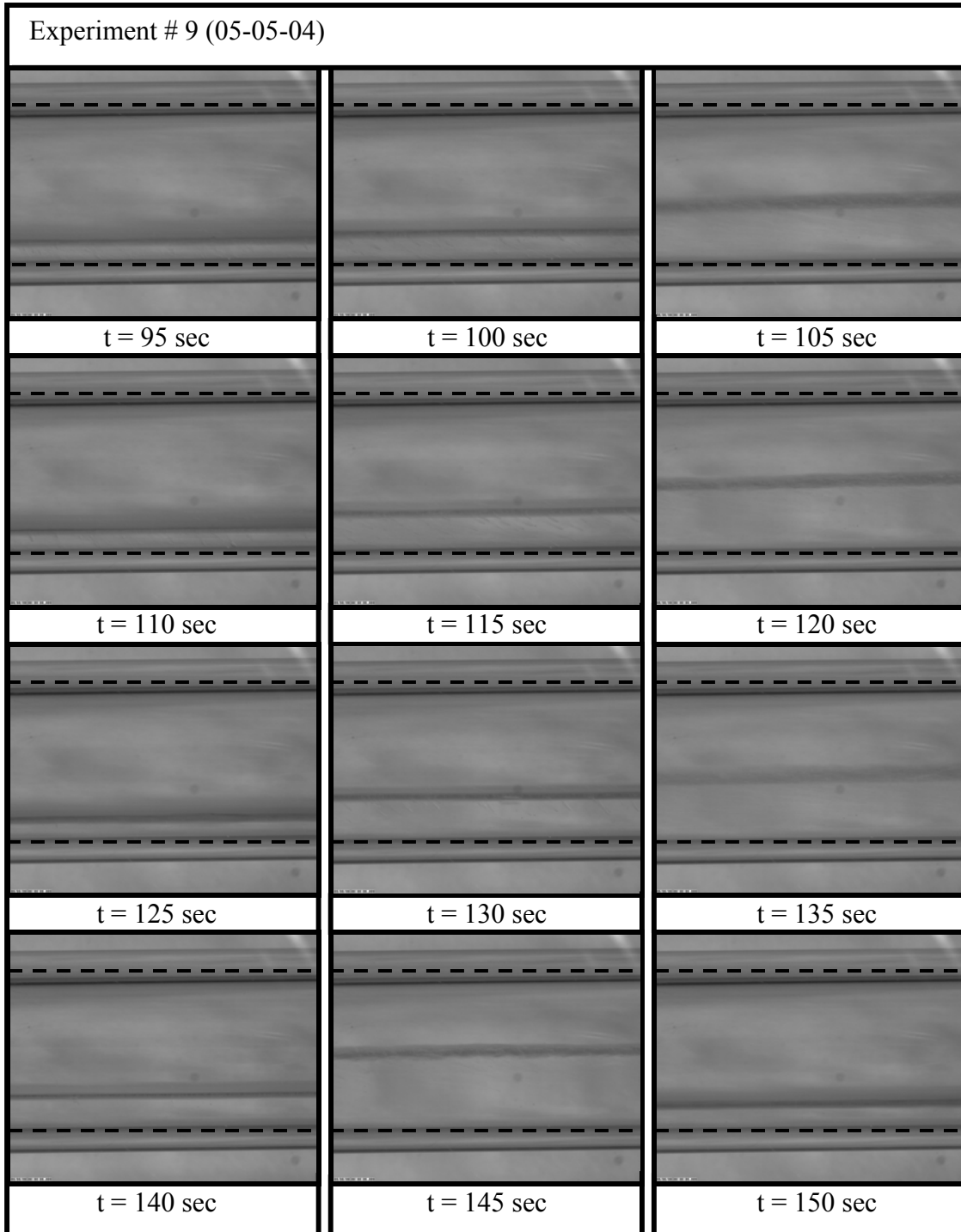


Figure B-9. Continued.

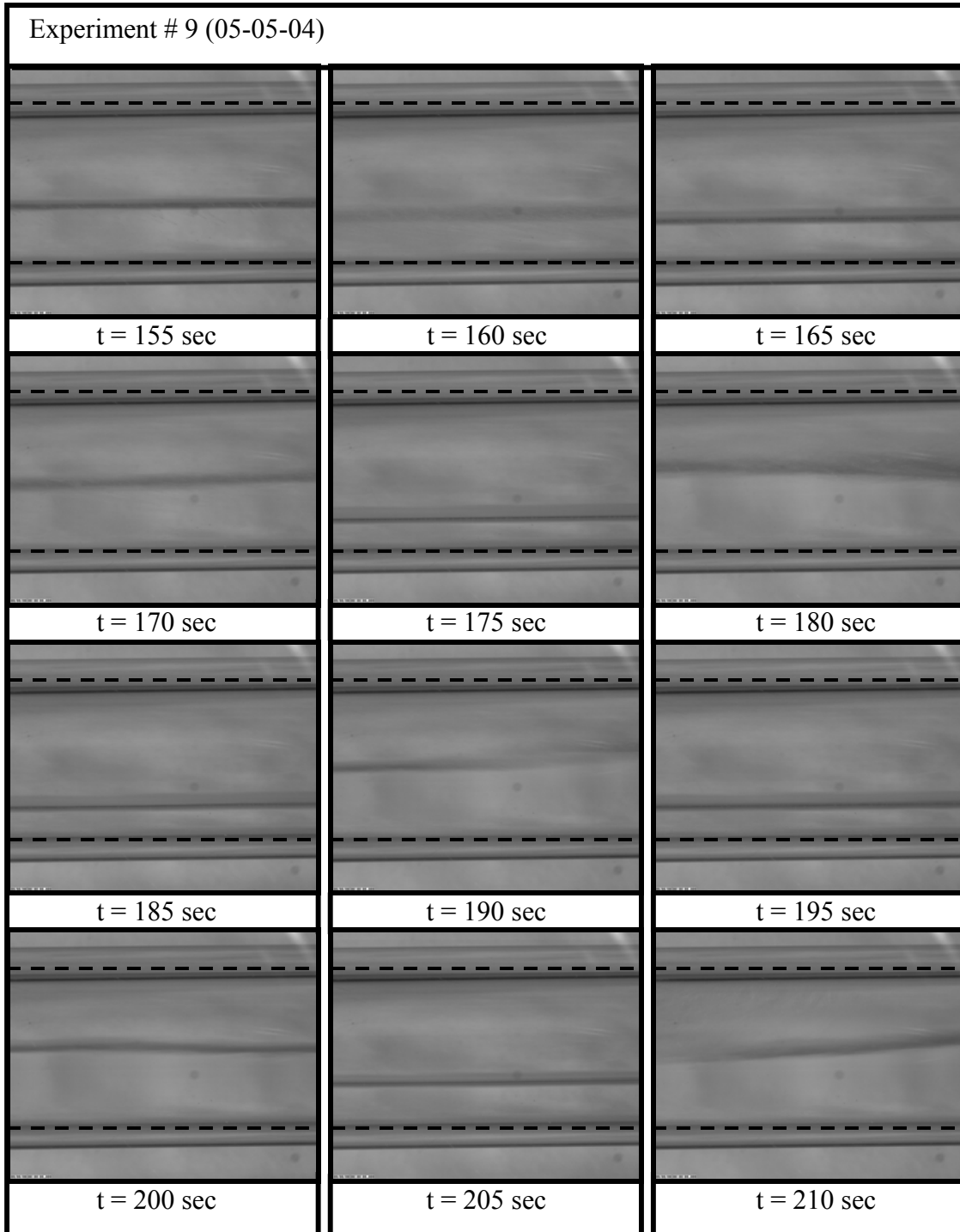


Figure B-9. Continued.

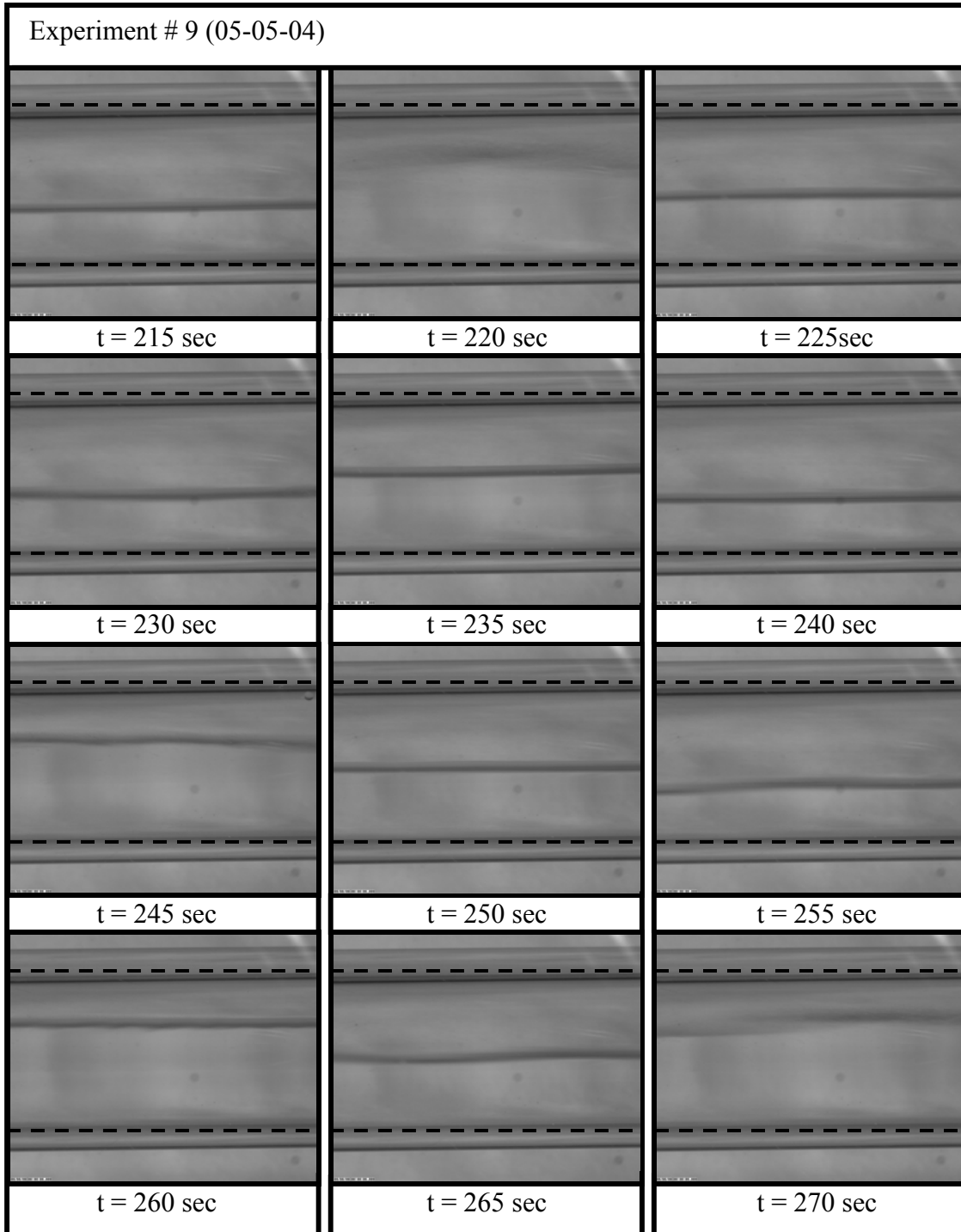


Figure B-9. Continued.

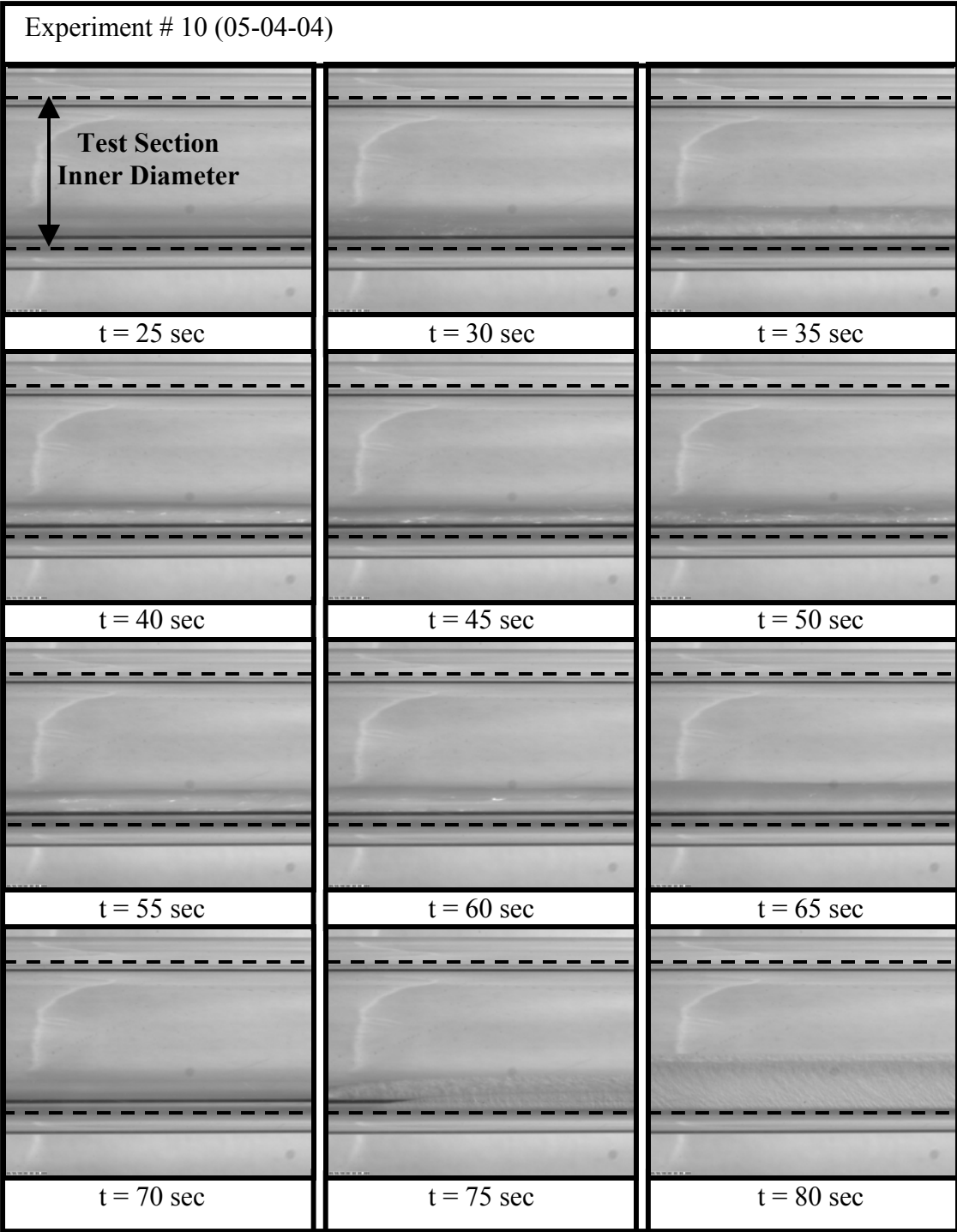


Figure B-10. Chardown images from experiment # 10.

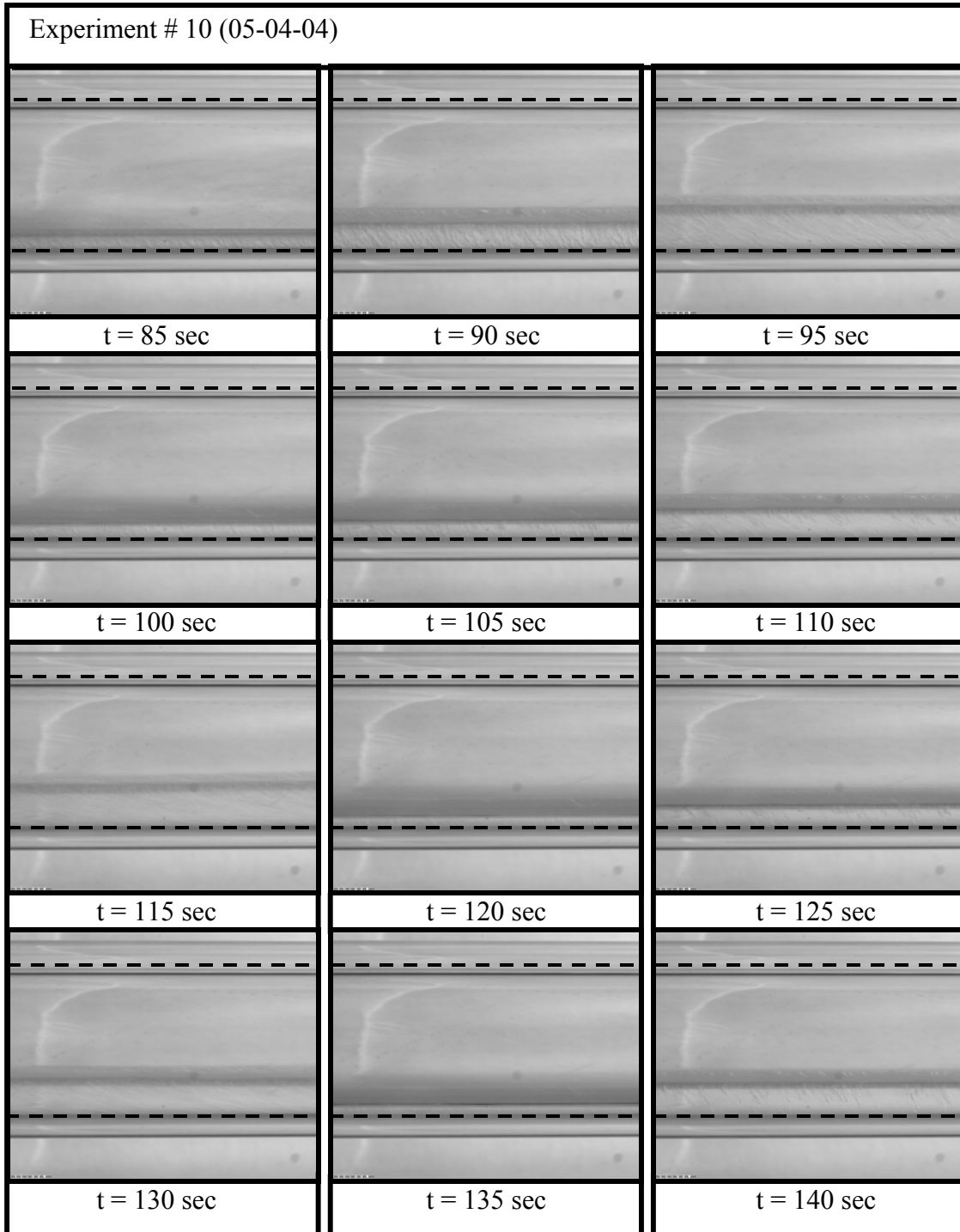


Figure B-10. Continued.

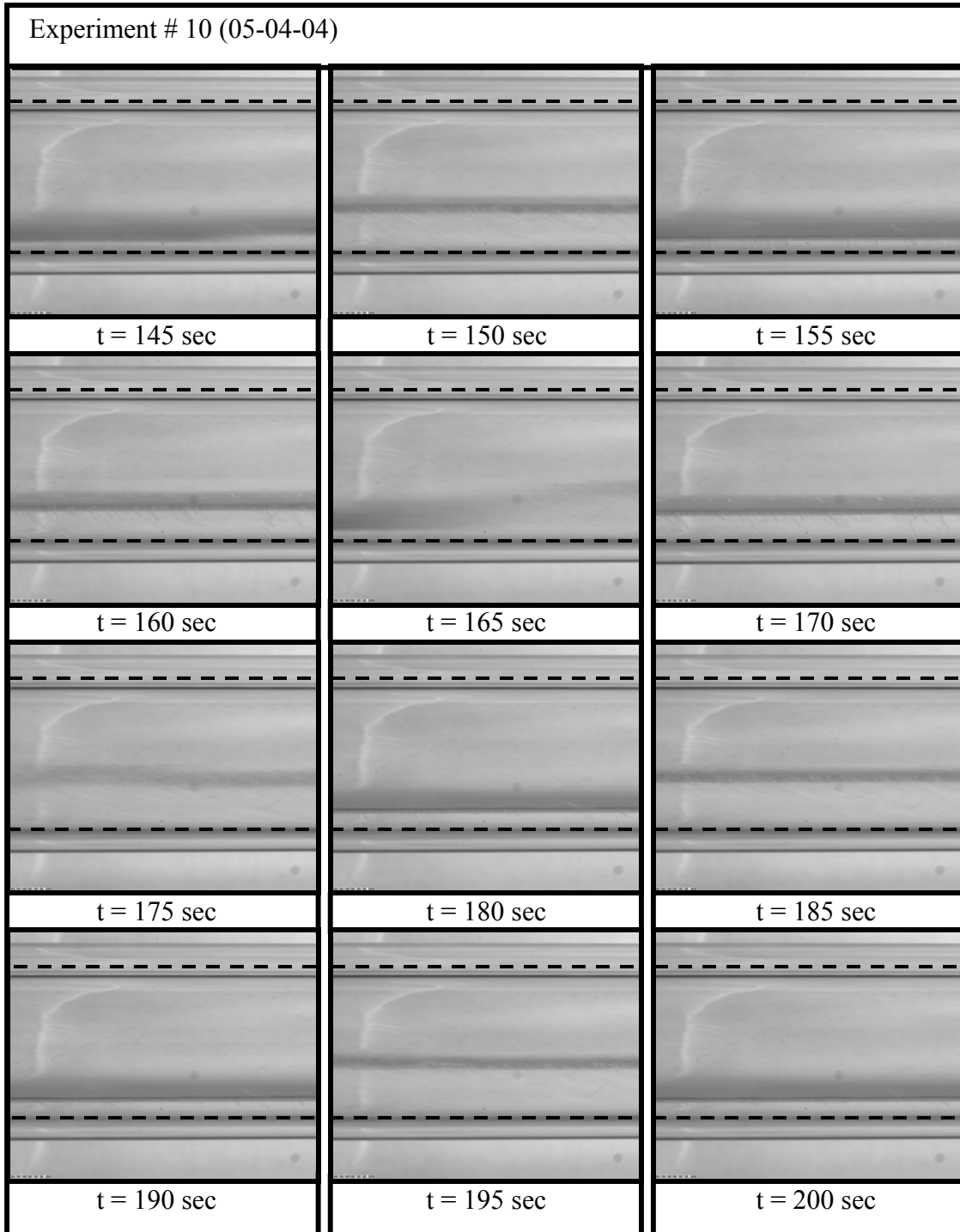


Figure B-10. Continued.

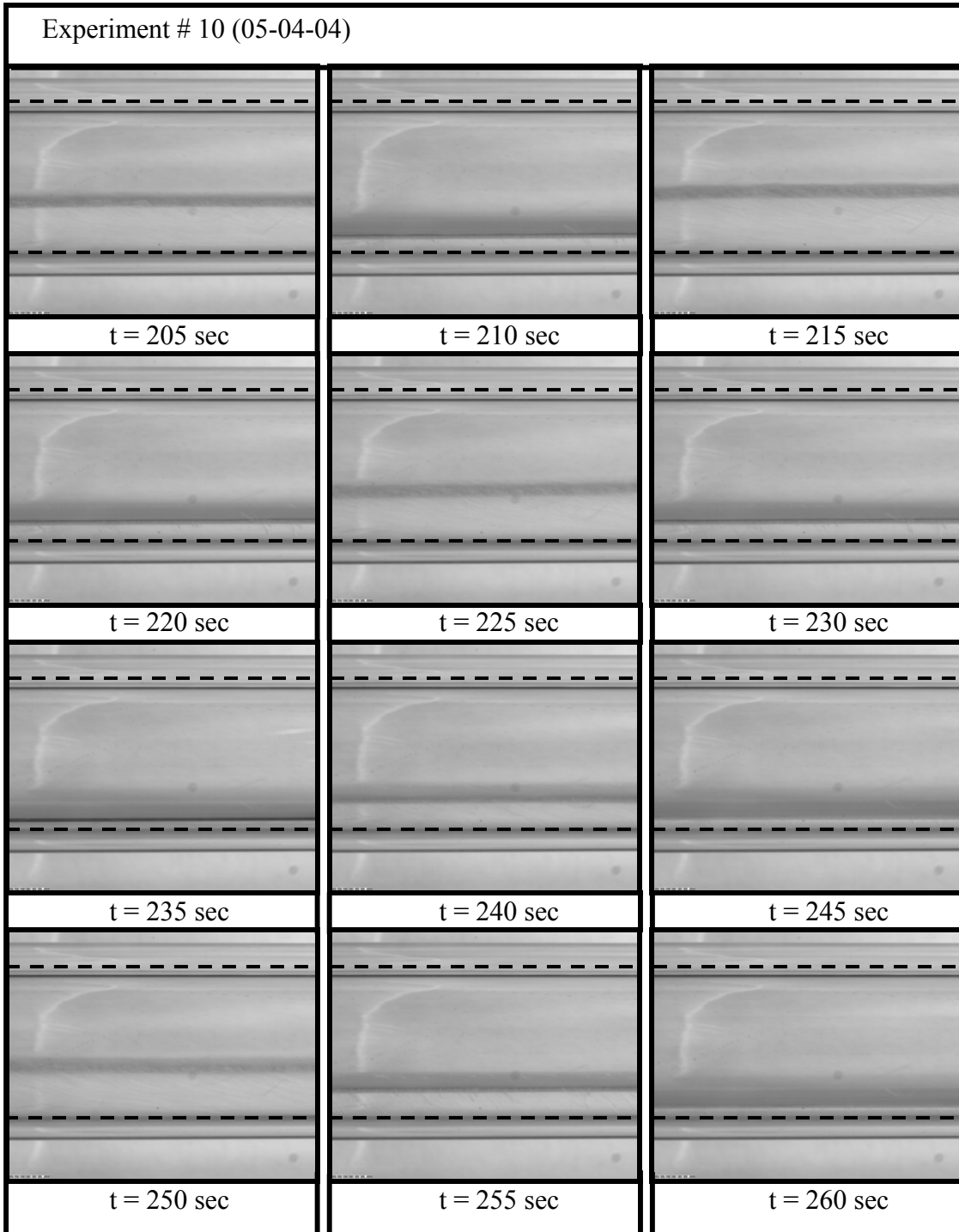


Figure B-10. Continued.

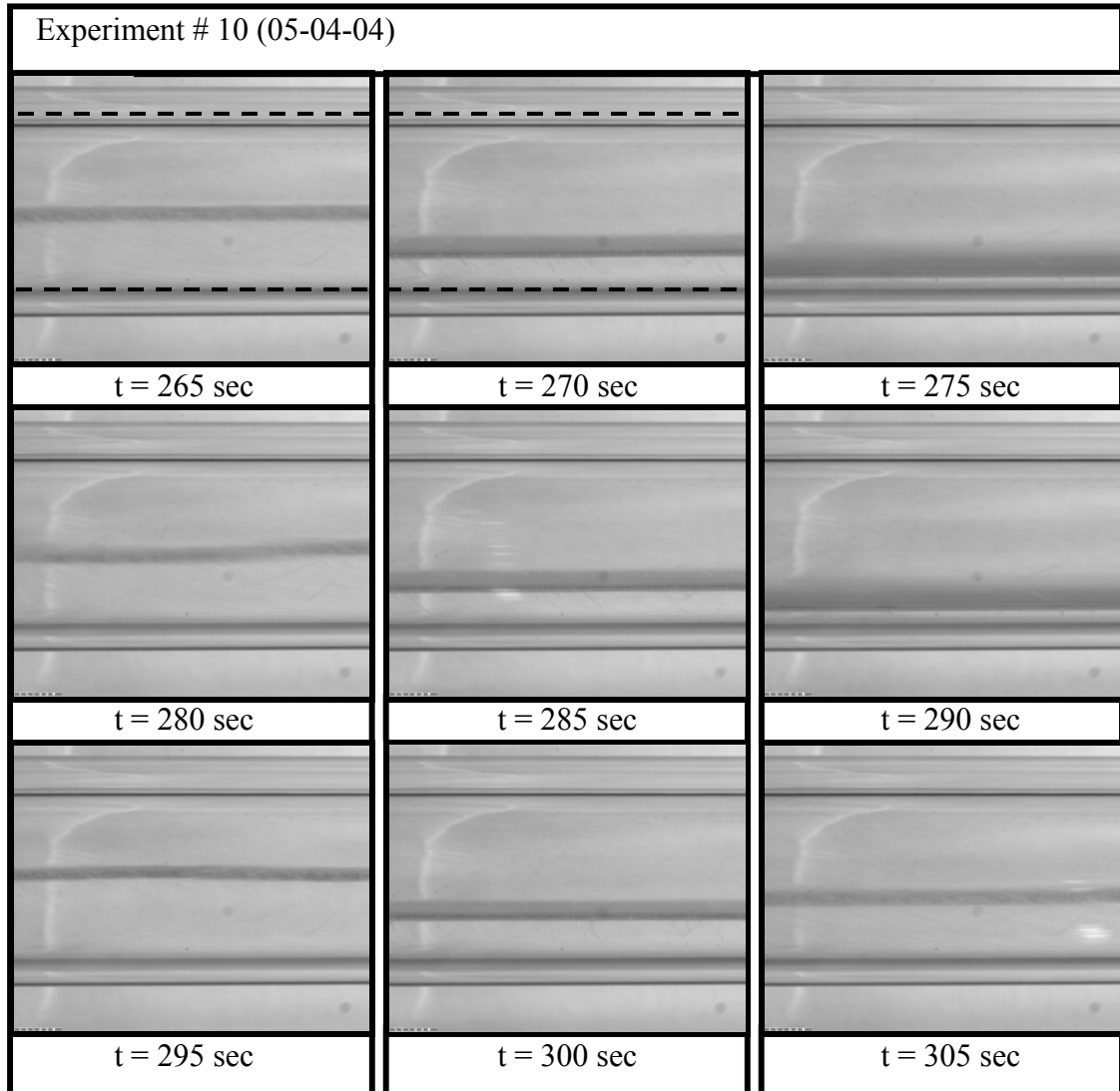


Figure B-10. Continued.

LIST OF REFERENCES

1. Burke, J.C., Byrnes, W.R., Post, A.H., Ruccia, F.E., 1960, "Pressurized Cooldown of Cryogenic Transfer Lines," *Advances in Cryogenic Engineering*, Vol. 4, pp. 378-394.
2. Bronson, J.C., Edeskuty, F.J., Fretwell, J.H., Hammel, E.F., Keller, W.E., Meier, K.L., Schuch, A.F., Willis, W.L., 1962, "Problems in Cool-Down of Cryogenic Systems," *Advances in Cryogenic Engineering*, Vol. 7, pp. 198-205.
3. Baker, O., 1954, "Design of pipe lines for simultaneous flow of oil and gas," *Oil and Gas Journal*, 53, pp. 185.
4. Hedayatpour, A., Antar, B.N., Kawaji, M., 1993, "Cool-Down of a Vertical Line with Liquid Nitrogen," *Journal of Thermophysics and Heat Transfer*, Vol. 7, No. 3, pp. 426-434.
5. Steward, W.G., Smith, R.V., Brennan, J.A., 1970, "Cooldown Transients in Cryogenic Transfer Lines," *Advances in Cryogenic Engineering*, Vol. 15, pp. 354-363.
6. Carey, V., 1992, *Liquid-Vapor Phase-Change Phenomena*, Taylor and Francis Press, New York.
7. Warren, B.A. and Klausner, J.F., "Developing Lengths in Horizontal Two-Phase Bubbly Flow," *Journal of Fluids Engineering*, Vol. 117, pp. 512-518, 1995.
8. Barnea, D., and Taitel, Y., 1994, "Interfacial and Structural Stability of Separated Flow," *International Journal of Multiphase Flow*, Vol. 20, pp. 387-414.
9. Chi, J.W.H, 1965, "Cooldown Temperatures and Cooldown Time During Mist Flow," *Advances in Cryogenic Engineering*, Vol. 10, pp. 330-340.
10. Solomon, 2003, "Information Specific to Liquid Nitrogen," <http://www-safety.deas.harvard.edu/services/nitrogen.html> , July 31st, 2003, Harvard College.
11. "Pyrex Borosilicate Glass", 2002, <http://www.bibbysterilin.co.uk/internet/bibbsite.nsf/AllDocumentsByDocIndex2/EWYN5EWB5WTALN5HMJ6G> , June 15th, 2002, Bibby Sterlin Co.
12. White, F.M., 1986, *Fluid Mechanics*, McGraw-Hill, New York.

13. Zuber, N., and Findlay, J.A., "Average Volumetric Concentration in Two-Phase Flow Systems," *Journal of Heat Transfer*, Vol. 87C, pp. 453-468, 1965.
14. Klausner, J.K., 1989, "The influence of Gravity on Pressure Drop and Heat Transfer in Flow Boiling," Ph.D. Thesis, University of Illinois at Urbana-Champaign.
15. Graham, R.W., Hendricks, R.C., Hsu, Y.Y., Friedman, R., 1961, "Experimental Heat Transfer and Pressure Drop of Film Boiling Liquid Hydrogen Flowing Through A Heated Tube," *Advances in Cryogenic Engineering*, Vol. 6, pp. 517-524.
16. Chi, J.W.H, and Vetere, A.M., 1963, "Two-Phase Flow During Transient Boiling of Hydrogen and Determination of Nonequilibrium Vapor Fractions," *Advances in Cryogenic Engineering*, Vol. 9, pp. 243-253.
17. Kutateladze, S.S., 1952, "Heat Transfer in Condensation and Boiling," State Science and Technology Publication of Literature on Machinery, Moscow, Atomic Energy Commission Translation 3770.
18. Kawaji, M., and Banerjee, S., 1987, "Application of a Multifield Model to Reflooding of a Hot Vertical Tube: Part I-- Model Structure and Interfacial Phenomena," *Journal of Heat Transfer*, Vol. 109, pp. 204-211.
19. Kawaji, M., and Banerjee, S., 1988, "Application of a Multifield Model to Reflooding of a Hot Vertical Tube: Part II—Analysis of Experimental Results," *Journal of Heat Transfer*, Vol. 110, pp. 710-720.
20. Cross, M.F., Majumdar, A.K, Bennett Jr., J.C, Malla, R.B, 2002, "Modeling of Chill Down in Cryogenic Transfer Lines," *Journal of Spacecraft and Rockets*, Vol. 39, No. 2, pp. 284-289.
21. Willis, W.L., and Smith, J.R., 1965, "Detection of Density Variations in Flowing Two-Phase Hydrogen," *Advances in Cryogenic Engineering*, Vol. 10, pp. 323-329.
22. Killian, W.R., and Simpson, J.O, 1960, "Measuring Vapor-Liquid Ratios During Flow by a Capacitance Method," *Advances in Cryogenic Engineering*, Vol. 5, pp. 505-508.
23. Khalil, A., McIntosh, G., Boom, R.W., 1981, "Experimental Measurement of Void Fraction in Cryogenic Two Phase Upward Flow," *Cryogenics*, Vol. 11, pp. 411-414.
24. Filippov, Yu. P., 2001, "How to Measure Void Fraction of Two-Phase Cryogenic Flows," *Cryogenics*, Vol. 41, pp. 327-334.
25. Steiner, I.D., 1993, "Heat Transfer to Boiling Saturated Liquids," *VDI – Heat Atlas*, pp. 1-30, Taylor and Francis Press, New York.

26. Kattan, N., Thome, J.R., Favrat, D., 1998, "Flow Boiling in Horizontal Tubes: Part 1 – Development of a Diabatic Two-Phase Flow Pattern Map," *Journal of Heat Transfer*, Vol. 120, pp. 140-147.
27. Kattan, N., Thome, J.R., Favrat, D., 1998, "Flow Boiling in Horizontal Tubes: Part 2 – New Heat Transfer Data for Five Refrigerants," *Journal of Heat Transfer*, Vol. 120, pp. 148-155.
28. Kattan, N., Thome, J.R., Favrat, D., 1998, "Flow Boiling in Horizontal Tubes: Part 3 – Development of a New Heat Transfer Model Based in Flow Pattern," *Journal of Heat Transfer*, Vol. 120, pp. 156-165.
29. Taitel, Y., and Dukler, A.E., 1979, "A Model for Predicting Flow Regime Transitions in Horizontal and Near Horizontal Gas-Liquid Flow," *AIChE Journal*, Vol. 22, No.1, pp. 47-55.
30. "Thermophysical Properties of Fluid Systems," 2003, <http://webbook.nist.gov/chemistry/fluid/>, June 28th, 2004, National Institute of Standards and Technology.

BIOGRAPHICAL SKETCH

Christopher was born in 1979 in Flint, Michigan, and is the second son of parents Ronald and Marianne Velat. Chris has resided in Sarasota, Florida, since 1986 and enrolled at the University of Florida in 1999. Following the completion of his Bachelor of Science degree in materials science and engineering in May of 2002, Chris enrolled in the mechanical and aerospace engineering graduate program in pursuit of a Master of Science degree and was selected as a Florida Space Grant Fellow. In 2003 Chris was selected as a pilot candidate with 142nd fighter wing of the Oregon Air National Guard and will attend officer school and undergraduate pilot training in the fall of 2004.